AD NUMBER

AD836763

LIMITATION CHANGES

TO:

Approved for public release; distribution is unlimited.

FROM:

Distribution authorized to U.S. Gov't. agencies and their contractors; Critical Technology; DEC 1967. Other requests shall be referred to Office of Naval Research, Washington, DC 20360. This document contains export-controlled technical data.

AUTHORITY

onr ltr, 28 jul 1977

SU-SEL-68-029

The Interpretation of HF Sweep-Frequency Backscatter Soundings to Deduce the Structure of Localized Ionospheric Anomalies

by

Thomas A. Croft

December 1967

Technical Report No. 116

Prepared under
Office of Naval Research Contract
Nonr-225(64), NR 088 019, and
Advanced Research Projects Agency ARPA Order 196

RADIOSCIENCE LABORATORY

STANFORD ELECTRONICS LABORATORIES

STANFORD UNIVERSITY · STANFORD, CALIFORNIA

MISSING PAGE
NUMBERS ARE BLANK
AND WERE NOT
FILMED

SEL-68-029

THE INTERPRETATION OF HF SWEEP-FREQUENCY BACKSCATTER SOUNDINGS TO DEDUCE THE STRUCTURE OF LOCALIZED IONOSPHERIC ANOMALIES

by

Thomas A. Croft

December 1967

Technical Report No. 116

Prepared under

Office of Naval Research Contract
Nonr-225(64), NR 088-019, and
Advanced Research Projects Agency
ARPA Order No. 196

Radioscience Laboratory
Stanford Electronics Laboratories
Stanford University Stanford, California

ABSTRACT

By use of computer simulation, it is possible to predict the effect of traveling ionospheric irregularities upon the data obtained by HF sweep-frequency ground-backscatter sounders. The simulation process makes use of an ionospheric model in which radio rays are traced to determine the time distribution of energy along the distant ground after skywave travel. Subsequent computation yields a synthetic record of the echo amplitude as a function of radio frequency and time delay, much like the experimental data. The degree of realism achieved is limited primarily by the need for economy; the process used here is a simplified version of one previously described (Ref. 1).

It is shown that a localized ionospheric irregularity causes a discontinuity in backscatter echo amplitude with a limited extent in frequency and with a delay that is comparatively independent of frequency. This discontinuity has the appearance of a short streak on the synthetic records; such a feature is common in experimental data. When an ionospheric irregularity exists from the ground to an unlimited altitude and is formed with its long axis tilted about 45° away from the observer, a backscatter streak appears which is spread over the entire frequency range of the background echo. Furthermore, this streak is tilted on the record, i.e., its time delay increases with an increase in frequency. When a similar anomaly is programmed so that it tilts inward toward the observer, then the resulting streak has a delay that decreases with an increase in frequency. A relation between the tilt of the anomaly and the tilt of the backscatter streak is thus demonstrated. The relation is in accord with a limited observation that tilted streaks in experimental backscatter move only in the predicted direction of anomaly motion as deduced from the measured direction of anomaly tilt.

Anomalies with constant altitude are shown to produce new, short-range leading edges on the backscatter. Experimental data having this form can thus be interpreted as an indication of the presence of small "layerlets" within the ionosphere, but it is noted that there are at least three other possible causes for this particular form of backscatter echo.

CONTENTS

ILLUSTRATIONS

ILLUSTRATIONS (Cont)

TABLE

ACKNOWLEDGMENT

When this paper was given at the IAGA-URSI Symposium at St. Gallen, Switzerland, on October 4, 1967, I was privileged to show some remarkable lapse-time motion pictures of waves in noctilucent clouds, which were made available by Dr. B. F. Fogle (who is now at the National Center for Atmospheric Research). I thank him for this and also I thank Mr. L. H. Tveten of ESSA who similarly made available a movie of his sweep-azimuth backscatter which shows waves so clearly. A short sequence from each film is included in a 15-minute motion picture describing this research; copies can be obtained from Mrs. J. Virginia Lincoln, Chief of the ITSA Data Services, ESSA, Boulder, Colorado.

The work reported here was supported by the Advanced Research Projects Agency through the Office of Naval Research, Contract Nonr-225(64).

I INTRODUCTION

Many forms of experimental data indicate that there are extensive traveling irregularities in the earth's upper atmosphere. Study of the mechanics of wave propagation in this regime indicates that a considerable portion of the traveling irregularities are "atmospheric gravity waves," that is, waves whose propagation depends upon the force of gravity. In noctilucent clouds, which are near the lower edge of the ionospheric E region, one often sees a number of long, straight, parallel ripples. Figure 1 is an unusual set of pictures of these clouds. Here we see the intersection of two different wave trains that are crossing one another. Lapse-time motion pictures of such clouds (Ref.2) show that the ripples move relative to the apparent motion of the material (the wind) and that there may be different ripples moving in different directions simultaneously. The existence of such structures is also indicated in the variable-azimuth backscatter data of Tveten (Ref. 3), which often show the apparent progress of a sequence of long, straight waves as they travel through the ionosphere. Similar irregularities have been mapped in a vertical plane by measuring incoherent electron scatter (Ref. 4), but this experimental method works only above the observer and therefore is limited by the immobility of the required equipment. Other experimental techniques can show evidence of the passage of irregularities, but they produce data from which it is comparatively difficult to deduce the morphology of the electron density distribution.

It will be shown here that one can extract clues about the vertical profile of a distant traveling wave from sweep-frequency HF sounder measurements of ground backscatter which propagates each way via the ionosphere. This is not a new form of data; it is similar to the data of Hunsucker and Tveten except that here the antenna azimuth is fixed and the frequency slowly varies across the HF spectrum. Figure 2 shows 30 records of such backscatter obtained with a sounder at Stanford. Notice that a number of near-horizontal streaks are present; these can be interpreted to shed light on the vertical distribution of electrons within traveling ionospheric irregularities. Since skywave energy travels at

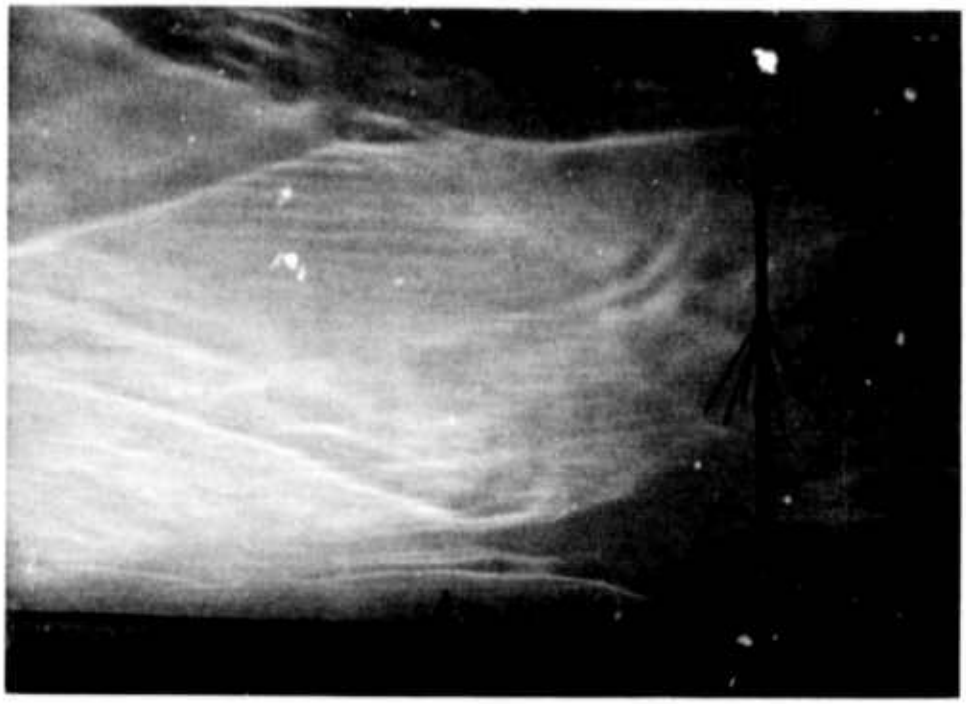

a. Photograph taken by K. A. Devine at 0115 AST

b. Photograph taken by K. A. Devine at 0133 AST

Fig. 1. NOCTILUCENT CLOUDS PHOTOGRAPHED FROM FORT CHIMO ON JULY 6, 1964.

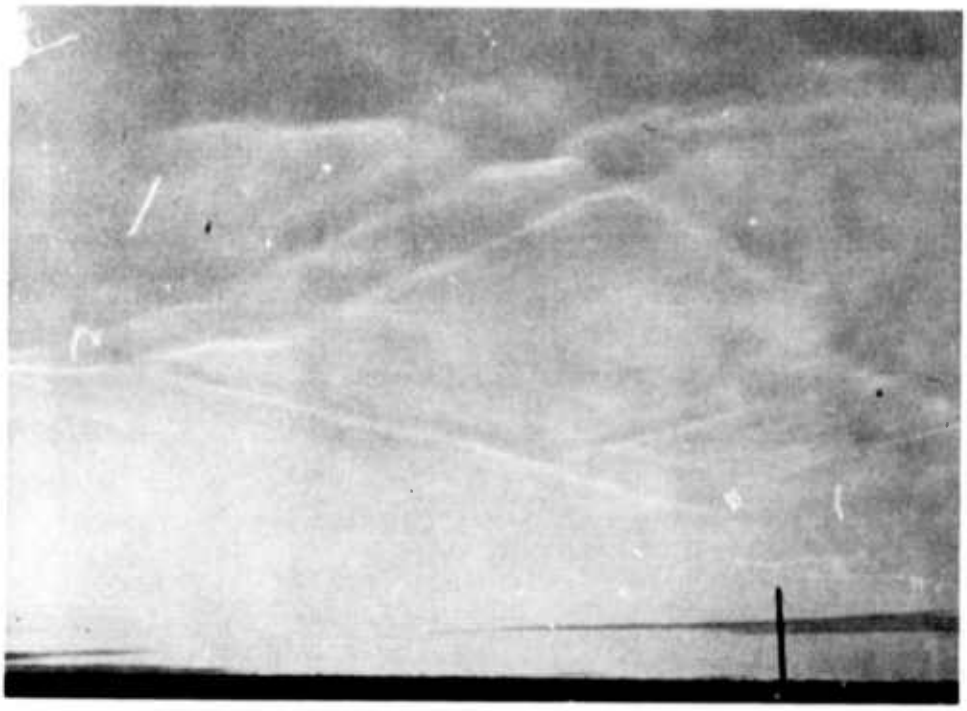

c. Photograph taken by J. L. Veilleux at 0130 AST

Fig. 1. CONTINUED.

nearly the speed of light, the ground from which this scatter is obtained is approximately 1500 km distant for each 10 msec of group delay. It will be shown here that an ionospheric irregularity tends to focus energy at the ground range of those rays that have their apogee located in or near the irregularity. Consequently, for one-hop backscatter, the range of a detected irregularity is approximately half the range of the scattering ground, or 750 km per 10 msec of backscatter group delay. By this approximate rule, it may be seen that the irregularities shown on the one-hop backscatter of Fig. 2 are located in the ionosphere at a distance of 600 to 1800 km from the sounder. (Similar streaks in multihop backscatter will not be discussed here, although they are plentiful on the data.)

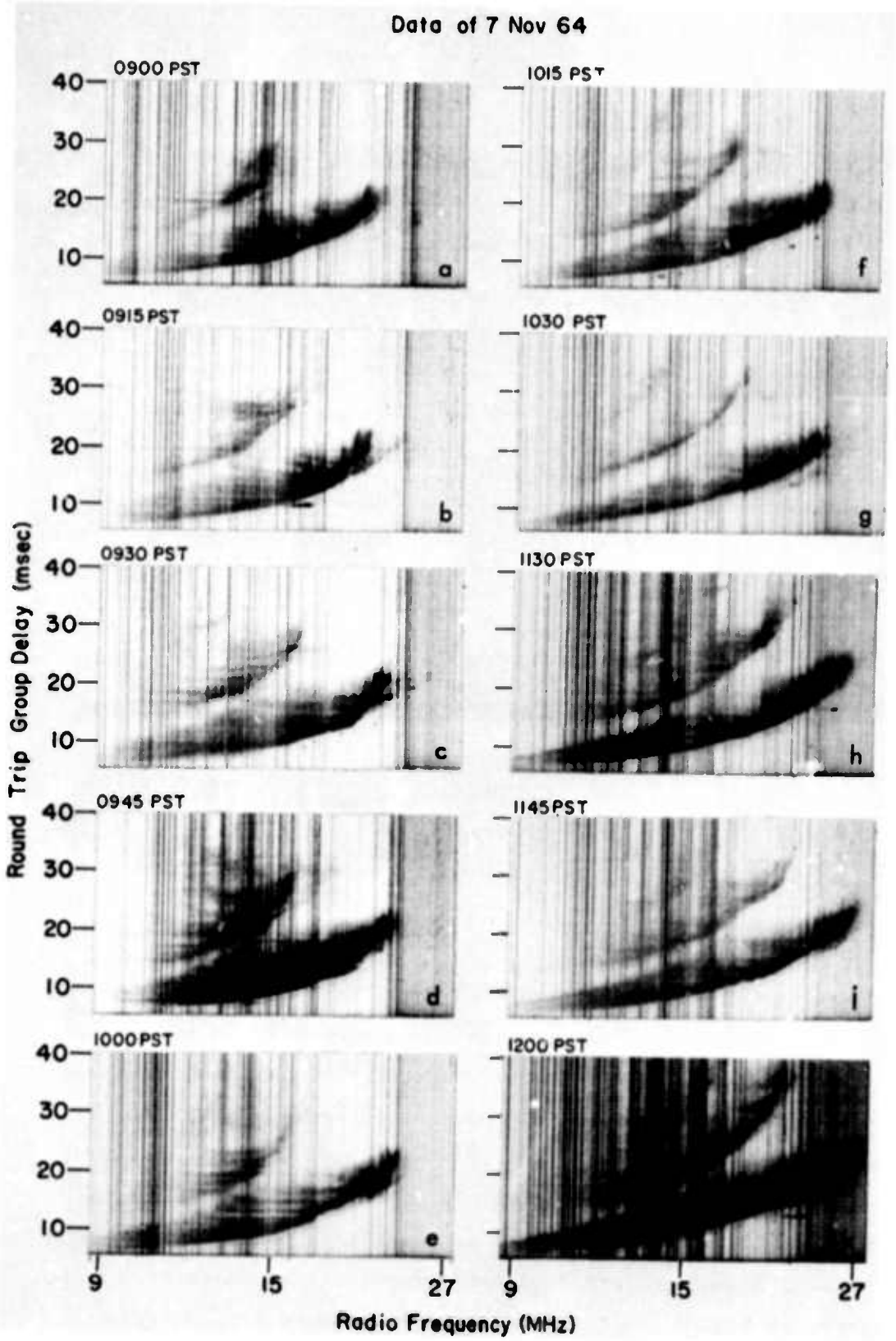

Fig. 2. THIRTY EXPERIMENTAL SWEEP-FREQUENCY BACKSCATTER SOUNDINGS OBTAINED WITH A 5 kW SOUNDER NEAR STANFORD. (Ref. 5)

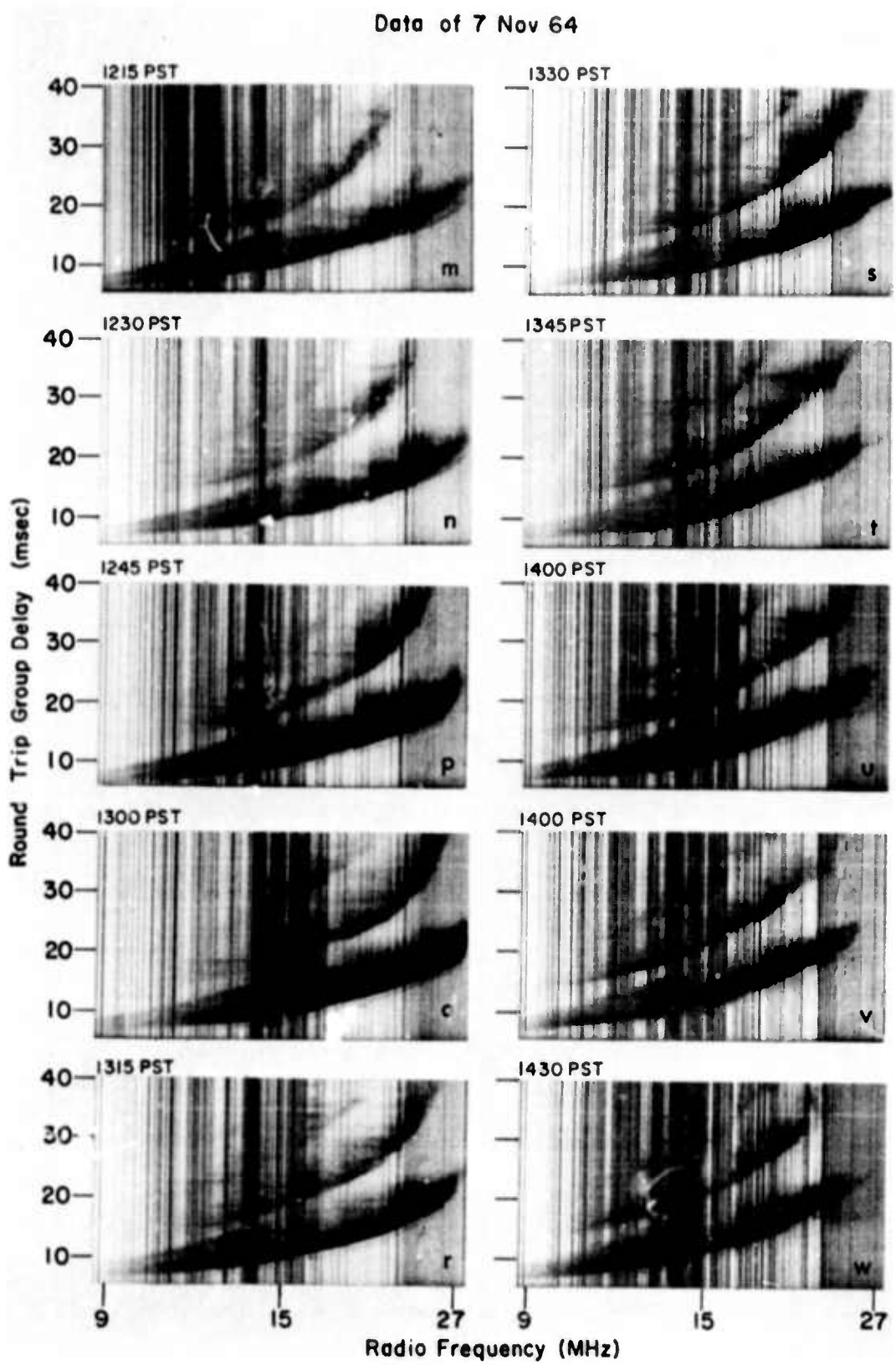

Fig. 2. CONTINUED.

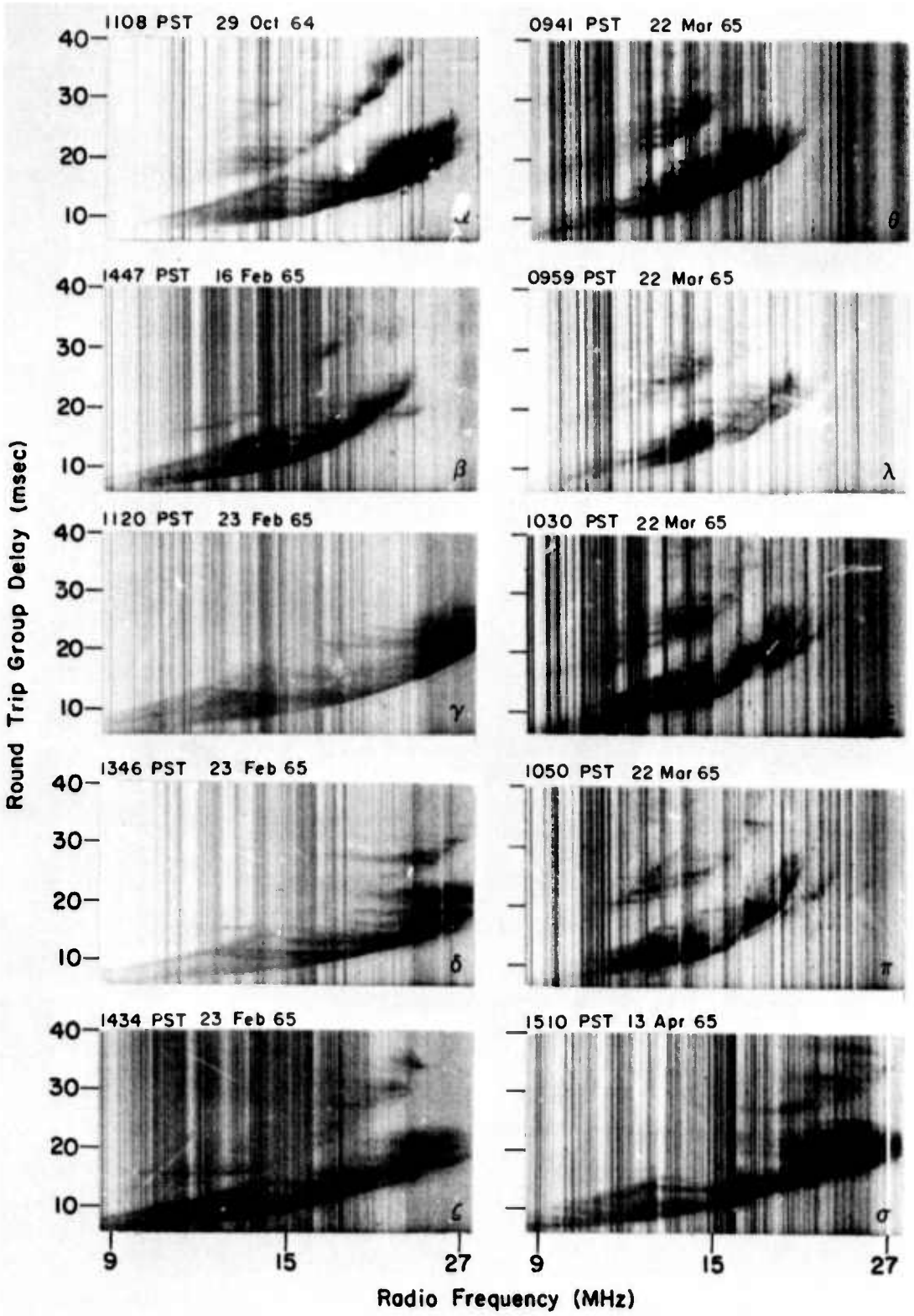

Fig. 2. CONTINUED.

On September 19, 1967 my colleague, Mr. Taylor Washburn, ran a test to check for the existence of moving streaks on sweep-frequency backscatter. He obtained 58 frames of backscatter in a time so short that it is possible to observe the motion of individual streaks. For ease of reference, these frames are considered to constitute Fig. 3, and they are presented as an appendix at the end of this report. It is intended that the reader should be able to flip through the appendix with his gaze fixed on each frame to see the motion of the backscatter irregularities.

On the right side of each frame is given the Pacific daylight time. This is Greenwich mean time minus 7 hours. There was nominally one frame every 2 min obtained with a sweep rate of 250 kHz per second downward from 27 to 9 MHz. The chirp sweep technique was used with a transmitted power of 30 kW into an antenna recently built by ITT at the Lost Hills field site of Stanford University. This antenna is a broadside array of folded tilted monopoles directed along a bearing of 86°. The antenna has 18 elements on nominal 40-ft spacings for a total aperture of 680 ft when it is in the transmission mode. The backscatter was received at Site 514 on the Stanford campus by means of a rhombic antenna. These particular data were obtained during an early test of some new equipment and therefore many of the settings of equipment variables were not optimized. As a consequence, it appears that the data have a very limited dynamic range, which is particularly unfortunate in the present context since interest here is centered on very slight discontinuities in the echo amplitude. Many of the tilted streaks on the backscatter are only barely visible for a single frame; it is therefore not possible to follow the motion of very many of the interesting features. Doubtlessly, we will obtain much better data of this type in the near future, but at the time of this writing (December, 1967) these data were the best available of this type.

II THE METHOD OF SIMULATING BACKSCATTER

Analysis of the phenomena that play a part in the production of ground backscatter shows that each mechanism is comparatively simple but that there is an interplay of such a variety of mechanisms that the entire process is rather complex. Fortunately, since computers share this characteristic, backscatter can be simulated in a straightforward manner: It is only necessary to simulate each mechanism and to program an appropriate interaction of the parts, copying the natural process. Because of economic considerations, it is convenient to break the calculations into two parts, designated "raytracing" and "backscatter synthesis," which are related to one another, as shown in Fig. 4.

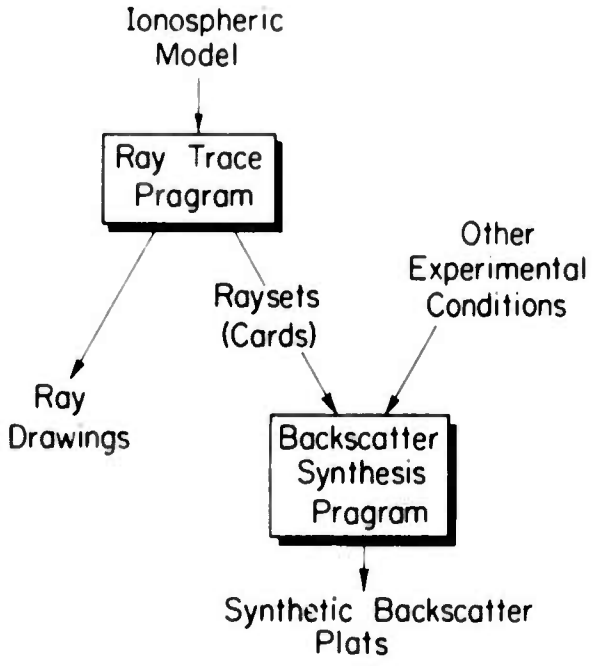

Fig. 4. THE SIMULATION PROCEDURE.

A. Raytracing and the Rayset Method

To begin the process, one must select and encode an ionospheric model, which is a two-dimensional electron distribution. Radio rays are then traced in the model by any one of a variety of methods. These will not be discussed here because they constitute an extensive subject in

themselves and because the specific choice of a method is unimportant in the present context.* The program used here is a repeated application of Snell's law in a refractive index distribution which is scalar because the geomagnetic field is neglected. The computed output consists of ray drawings and also of ray information coded into punched cards, which are called raysets. These contain enough information to describe the time and space distribution of an ionospherically propagated (skywave) pulse along the ground. Thus the raysets provide the backscatter synthesis program with all necessary information relating to the effect of the ionospheric model.

As a consequence of this approach, it is possible to compute the effect on backscatter of any ionospheric irregularity through which one can trace rays. This is the key to the power of the technique. With the present state of the art, our ability to trace rays is limited primarily by the necessity for economy; the methods for simulation are well developed.

B. Backscatter Synthesis

The synthesis can be carried out with striking realism; it can be compared to complicated bookkeeping in the sense that each simulated mechanism is simple but many of them interact so that the entire process is complex. The most realistic simulation (Refs. 1 and 6) required roughly 1 min on a large computer. For this study it was desired to compute backscatter for 10 to 30 frequencies per "sweep-frequency" record, but the price of 10 to 30 min of computer time was prohibitive. The original simulation program made use of a number of approximations: For example, the geomagnetic field was neglected during ray calculation and the ionospheric model was only two-dimensional. (Backscatter has not yet been simulated in this manner without these two assumptions.) To reduce costs further, a number of additional simplifying assumptions have been made here, as follows:

---

*The interested reader can refer, for example, to the January 1968 issue of Radio Science, which is devoted exclusively to raytracing. Also, the author is preparing Technical Report No. 112, which will describe the Stanford University activities in high frequency radio raytracing.

(1) It is assumed that rays that travel out to the scatterer via a particular path can return only by the same path.

(2) Only one ionospheric hop is allowed along the path.

(3) The ground scatter coefficient varies with incidence angle and radio frequency, but it no longer is a function of range.

(4) For the purpose of calculating absorption, a single value of solar zenith angle is used, independent of range.

(5) The effect of pulse duration and shape is not calculated.

(6) Constant factors are ignored since only relative echo amplitude is calculated.

With these six additional assumptions, the simulation program became simplified to such an extent that program execution was reduced to roughly 2 sec per frequency sample in the synthetic backscatter. This makes the newer method practical as a research tool for preliminary studies and as a means for seeking gross behavior patterns. The original method can still be used for the study of effects that would be absent from this faster program due to the loss of realism. In both programs, the sounder antenna has gain which is a function of both elevation and azimuth and which furthermore is different at each radio frequency. It was believed that the gain pattern has such a strong influence on the backscatter that its form could not be neglected.

The new approximations, applied to Eq. (8) from Ref. 1, lead to the following expression for the backscatter power conveyed to and from the scattering ground between a neighboring pair of closely spaced, precomputed rays:

$$\text{Power} = \frac{G^2(\bar{\beta})\ \sigma_o(\bar{\psi})}{\bar{R}} \left(\frac{\cos\bar{\beta}}{\sin\bar{\psi}}\right)^2 \frac{(\Delta\beta)^2}{\Delta T\ \Delta R} \qquad (1)$$

where

G = antenna gain, a function of takeoff angle

β = ray takeoff angle measured relative to the horizon

ψ = ray landing angle at the scatterer end of the path

T = group delay along the ray

R = ground range traversed by a ray

$\Delta\beta$, ΔT, ΔR = differences of the parameters for two adjacent rays

$\bar{\beta}$, $\bar{\psi}$, $\bar{R}$ = averages of the parameters for the two rays

σ_o = ground scatter coefficient, set equal to $\sin^b \bar{\psi}$ with optional constant b

The power is reduced by absorption, which is calculated from the formula:

$$\frac{1700(\cos 0.881\ \bar{\chi})^{1.3}}{(F + 1.2\ \text{MHz})^2 \sqrt{1 - 0.97 \cos^2 \bar{\beta}}}\ \text{dB round trip} \qquad (2)$$

This formula has been derived from Laitinen and Haydon (Ref. 7) with provisions that the sunspot number is 100 and the electron gyrofrequency is 1.2 MHz. Here $\bar{\chi}$ is the average solar zenith angle along the path, a single constant set in the program by the user.

The backscatter simulation process is now very simple. At each frequency, each neighboring pair of rays is used to calculate the power that would be received according to Eqs. (1) and (2). The power is assumed to be received uniformly during the time interval from the minimum round trip time to the maximum round trip time (the minimum and maximum of 2T from the two rays). At any moment in time, one may receive the sum of several different power increments from different radio propagation modes. The computer adds all possible power increments as a function of time at each frequency and generates a plot of power vs time at that frequency.

C. The Data Display

By trial, it has been found most convenient to plot the logarithm of power, normalized so that a specified total number of decibels of variation is plotted. This specification is called "dynamic range" because it controls the appearance of the data much as the dynamic range of a receiver controls the appearance of actual backscatter. The data presented here have all been calculated at 30 dB to provide uniformity, although the decibel specification is arbitrary.

The display of the synthetic data is designed to simulate the experimental display such as that used on Fig. 2. A difficulty arises

because the data are three-dimensional. The experimental records show amplitude by varying the oscilloscope light intensity to be photographed, but no computer plotting device available at Stanford could produce a variable intensity plot. To overcome this limitation, the abscissa of the synthetic display is used for two different parameters according to the logic illustrated on Fig. 5. At the top is shown a model with three dimensions: time, frequency, and power. The synthesis is essentially a fixed-frequency process that is applied repeatedly at multiple frequencies. (The same is true of the experimental process when a pulsed sounder is used.) If the fixed-frequency records of Fig. 5a were hinged about their baseline so that they could be folded down onto the frequency-time plane, the record would look like that of Fig. 5b. It is necessary to adjust the power variation scale so that no single-frequency record overlaps the baseline of the next higher frequency. With this precaution, the abscissa can be used to represent both frequency and power in an unambiguous manner.

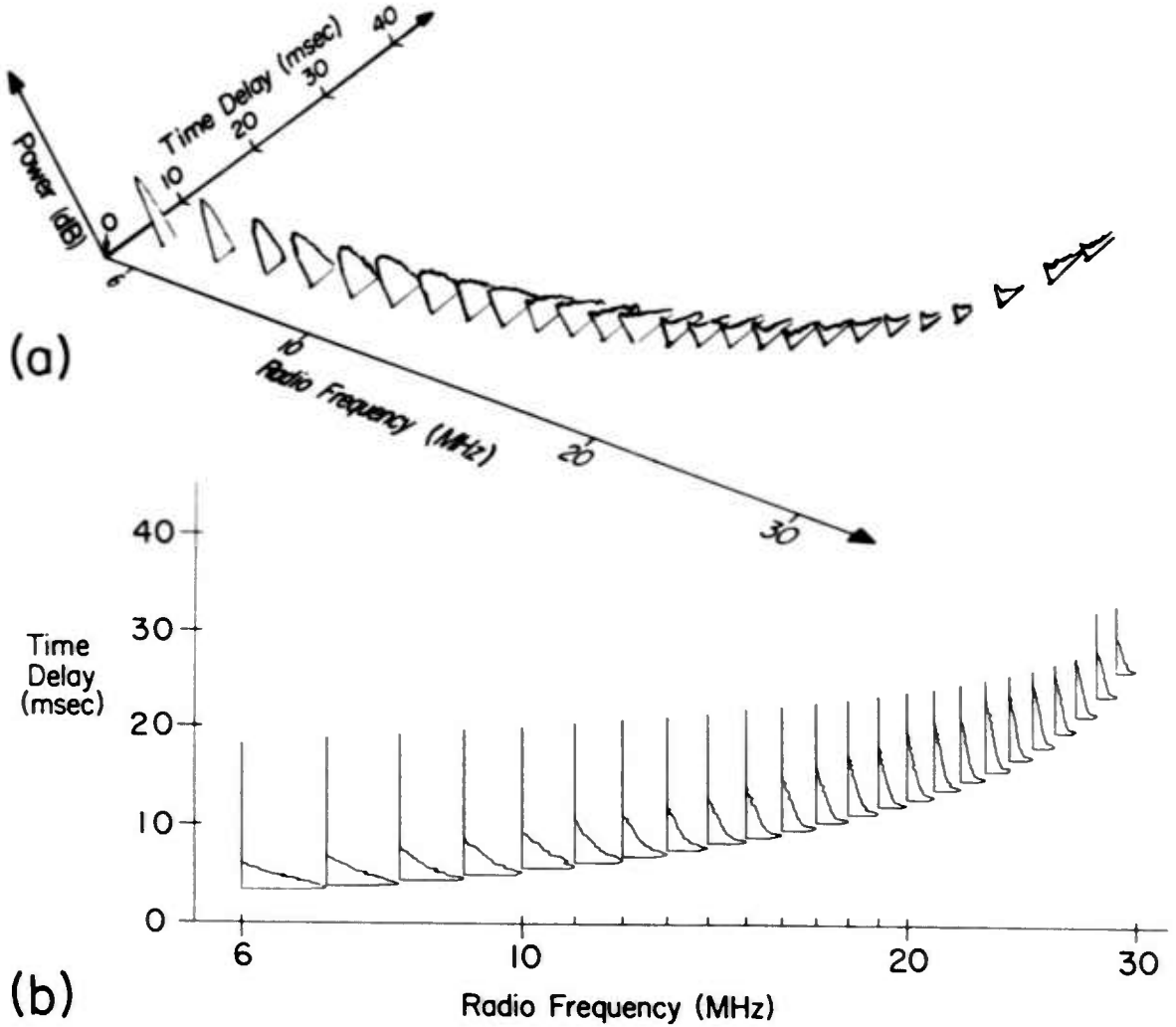

Fig. 5. THREE-DIMENSIONAL DATA. (a) Presented in a two-dimensional display; (b) where the abscissa represents both frequency and power.

III FIVE MODELS OF THE IONOSPHERE

Here, five ionospheric models will be used to produce synthetic sweep-frequency backscatter records. One model is the undisturbed ambient, a single Chapman layer with a maximum density of 10^6 electrons/cm^3 at an altitude of 300 km and a scale height of 100 km. The remaining models are identical except that each has an anomaly of some type.

Three models contain a localized irregularity approximately 1200 km from the hypothetical radar, with shapes as illustrated on Fig. 6. The top model (a) will be called the "local" model since it is concentrated in a circular area. The second model (b) will be called an "outward tilt" because the structure tilts away from the sounder. The third model (c) will be called an "inward tilt" since it is tilted inward. In each of these three models, the electron density profile across the local disturbance has a depletion region in which the number density vs distance is parabolic and in which the central density is 30 percent less than the ambient density outside the irregularity at that height.

The decrease of electron density by 30 percent of ambient in a traveling disturbance is not unreasonable. Reference 8 shows records of a disturbance in which the overhead electron density decreased by more than 70 percent within a few minutes during the passage of an irregularity. Also, one of the two profiles given by Ref. 4 shows a large region in which electron density is decreased by 30 percent.

The fifth model contains a small concentric "layerlet," that is, a region of limited depth within which the electron density is perturbed in a manner that is a function only of altitude. For this layer, the entire electron density model can be described by the single curve of electron density vs height shown in Fig. 7. The model was derived by multiplying the ambient Chapman function by a single cycle sinusoid of density vs altitude. The maximum density change was 10 percent and the cycle wavelength was 20 km in depth, as shown in Fig. 6d. In effect, we have moved roughly 6 percent of the electrons from the 250- to 260-km interval up to the 260- to 270-km interval. (This latter view is an approximation since the total number of electrons actually increased slightly due to multiplication by the sinusoid.)

It is somewhat debatable that this model should be included here in a discussion of traveling irregularities. The multiplying function might represent a traveling wave that is moving up or down while remaining concentric with the earth, but it might also represent a stationary shelf of ionization somewhat like a miniature ionospheric layer. The experimental data available indicate the existence of these structures but do not provide clues about possible motion.

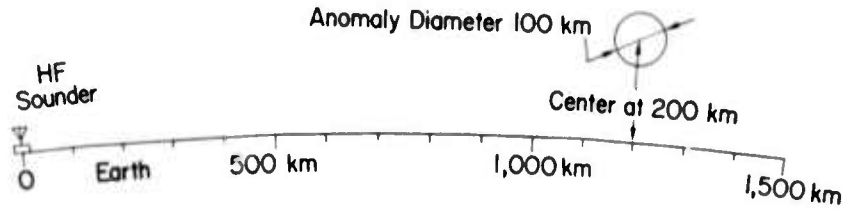

a. The local anomaly

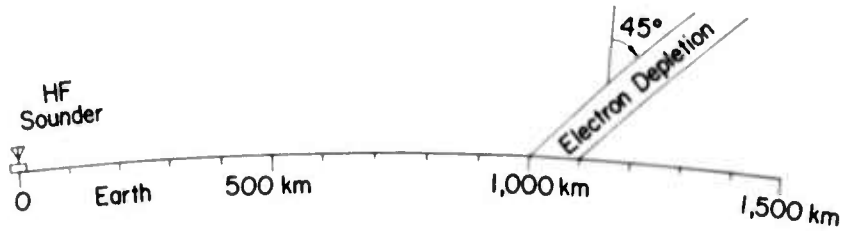

b. The outward tilt

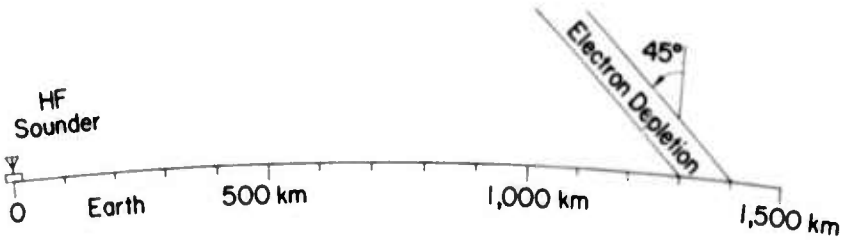

c. The inward tilt

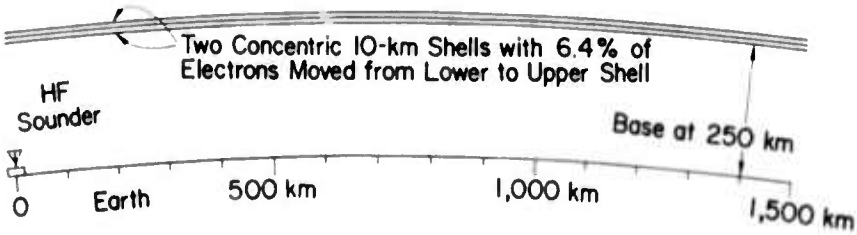

d. The concentric anomaly

Fig. 6. VERTICAL PROFILES OF THE FOUR IONOSPHERIC ANOMALY MODELS. These are used as perturbations in a single Chapman layer model.

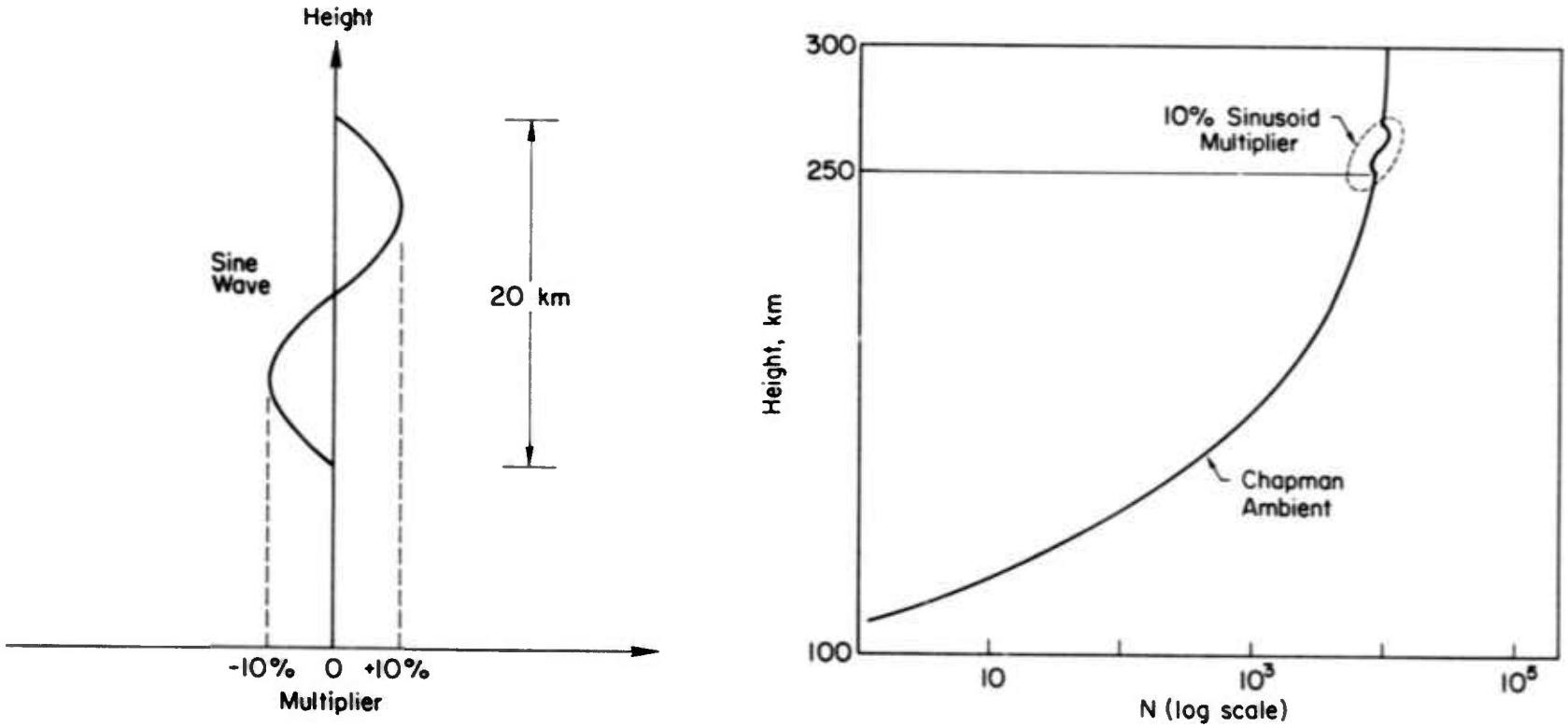

a. The density multiplier

b. The concentric anomaly model

Fig. 7. THE CONCENTRIC ANOMALY USED FOR SIMULATION. (Same as Fig. 6d)

IV SYNTHETIC BACKSCATTER FOR THE FIVE MODELS

A. Backscatter with the Ambient Ionosphere

The ambient ionospheric model was used to produce the synthetic backscatter shown on Fig. 5. Since the model is smooth, it follows that all of the small detail on the automatically drawn figure is attributable to errors in the simulation process. Some small-scale jitter is introduced by the automatic plotter, but most is due to the introduction of numerical errors through the use of finite steps in the simulation process. In a way, this is the synthetic analogy of noise and it can be reduced through the use of smaller steps in the computer with a consequent increase in the cost. One must therefore compromise and choose computation steps large enough to be economical and yet small enough that the desired results may be perceived. This is much like the choice of signal-to-noise ratio: it would be extravagant to strive for too much, but the ratio must be high enough that the signal can be identified.

Since each of the remaining ionospheric models is the same ambient Chapman layer with a single added anomaly, we may compare the resulting synthetic backscatter to that shown on Fig. 5 and attribute any differences to the anomalies. In this way, the effect of each anomaly can be separated from that due to other mechanisms which influence the time and frequency distribution of backscatter power.

B. Backscatter with Local or Tilted Anomalies

The first variation to be studied is the effect of the "local" anomaly in which minimum electron density occurs at the centerline 1200 km from the simulated HF sounder. The electron density as a function of height at the centerline is a parabola with its minimum at 200 km. The outer boundary of the depletion region would be a 100-km circle if plotted in cartesian coordinates of height vs ground range, but because of geocentric curvature, the actual boundary departs slightly from a circle.

For comparison with subsequent models, the most important feature of the local anomaly is its limitation in height: There is no change from ambient below 150 km or above 250 km. The effect of this spherical

depletion on radio rays is similar to the effect of a magnifying lens on light rays; that is, the rays that are off-center are refracted toward the centerline. The main complication arises here because the convergence effect is mixed with ionospheric refraction, making it somewhat difficult to visualize the total effect.

Synthetic backscatter computed with the local anomaly is shown in Fig. 8a. When compared to that derived from the ambient model, it is seen that there is a new "spike" in the backscatter at a time delay of about 16 msec, which is the round trip delay to the ground at twice the range of the anomaly itself. Ray plots show that there is focusing at 2400 km on the ground, as expected. It is particularly significant that this spike exists only over a limited range of frequencies because of the limited altitude interval occupied by the anomaly. At low frequencies, none of the rays is able to penetrate the ionosphere to the level of the bottom of the anomaly. When the frequency is too high, all the rays go over the anomaly. Thus it is seen that the altitude characteristic of the anomaly influences the frequency characteristic of the backscatter data. We will see that this altitude-frequency correspondence can be carried a step further to a more useful cause-effect relationship.

The "outward tilt" is the next anomaly inserted in the Chapman ionosphere and its effect is shown in the backscatter of Fig. 8b. This depletion region extends from the ground upward and, because of its unlimited altitude, the backscatter is influenced over a wider range of frequencies. Perhaps the most important point to notice is the increase in the delay of the backscatter spike with an increase in frequency. This is the key feature, indicating that the anomaly was tilted outward relative to the sounder.

The use of the inward tilt produces the backscatter of Fig. 8c, again unlimited in frequency because the anomaly is unlimited in height. Now, however, the delay of the backscatter spike decreases with increasing frequency, indicating that the anomaly is tilted inward. The magnitudes of the tilt angles such as those given on Fig. 8 are of course dependent on the choice of abscissa and ordinate scales, so the tilt changes would be more apparent if the display were compressed horizontally. In a previous

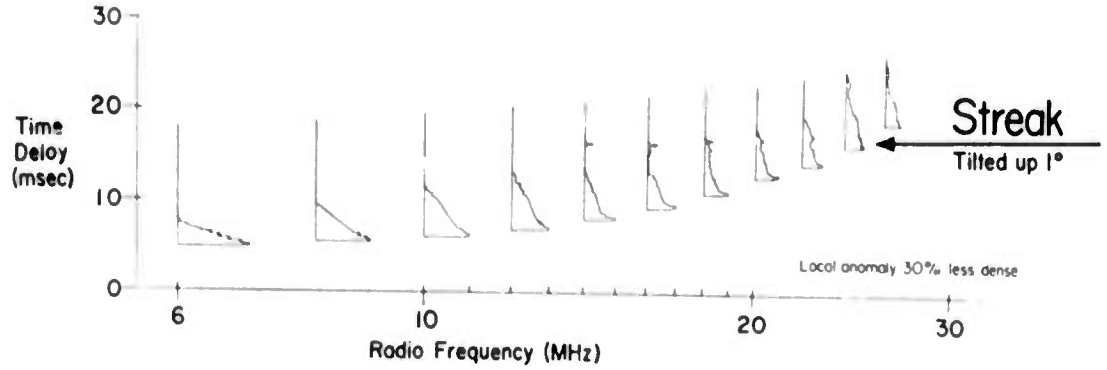

a. With the local anomaly

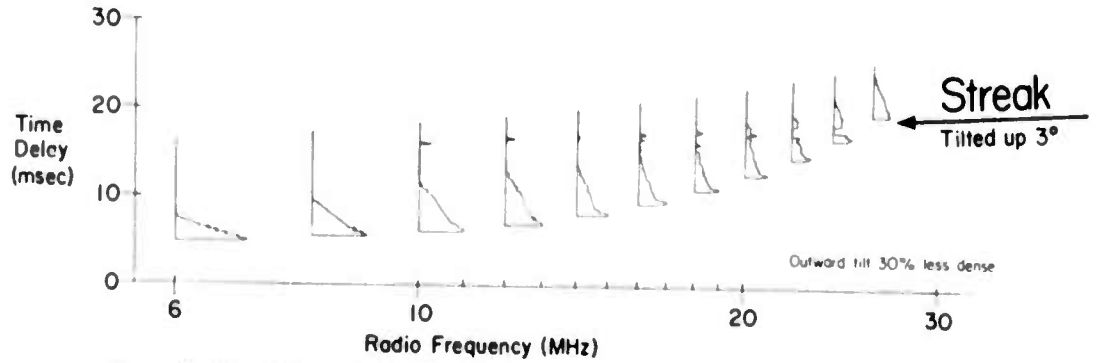

b. With the outward tilt

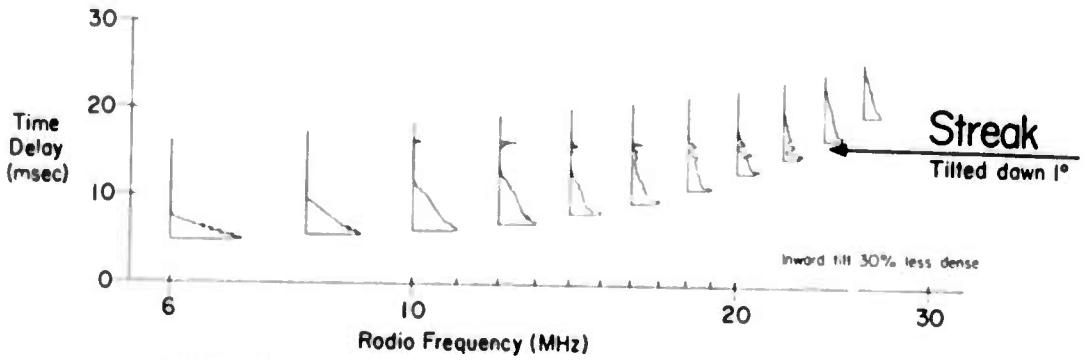

c. With the inward tilt

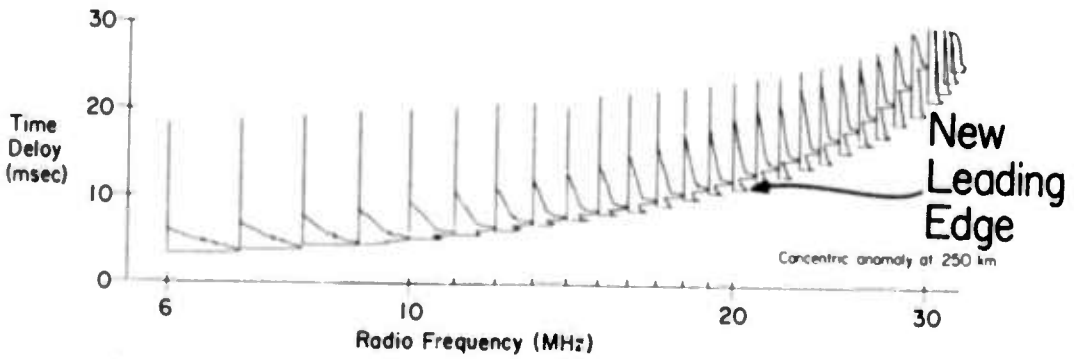

d. With the concentric anomaly

Fig. 8. SYNTHETIC BACKSCATTER COMPUTED WITH THE VARIOUS ANOMALIES. (These should be compared to Fig. 5.)

study, the author used a vertical anomaly that produced ray focusing on the ground at a fixed range independent of frequency (unpublished). That result motivated the present work, since it led to the suspicion that a tilted anomaly would produce a backscatter striation whose delay was a function of frequency.

The fact that the tilt of an anomaly affects the tilt of the associated streak is perhaps the most important conclusion of this study. On experimental backscatter data, tilted streaks or striations are often seen. One set of data is available with repetitive backscatter frames taken for 2 hours by a fast sounder so that it was possible to follow the progress of individual striations. This is given as Fig. 3 (Appendix). Six moving, tilted streaks can be found on the figure. In each of these examples, the delay decreases with increasing frequency and the entire echo moves inward toward the sounder. This echo behavior corresponds to an inward tilt moving toward the sounder; the direction of travel thus agrees with theoretical predictions that, in the F region, tilted gravity waves usually move only in the direction of tilt (Ref. 9). While these examples are not sufficient to support unambiguous conclusions, it is nevertheless encouraging that the direction of motion and the tilt direction agree with theory in each case. Further experimental investigation is clearly desirable. Also, we must investigate to see if other ionospheric models can cause tilted striations, for there is no guarantee that the interpretation given here is unique.

C. Backscatter with a Concentric Anomaly

When the concentric anomaly (actually a thin ionospheric layer) is inserted between 250 and 270 km, the calculated backscatter acquires the appearance shown in Fig. 8d. Comparison of this record with the ambient standard shows a new leading edge of the ground scatter with a shortened delay. It might be said that there is now a false leading edge--false in the sense that it represents the effect of a small perturbation on the larger ionospheric layer which alone would produce only the second (higher) leading edge of the two shown on the figure.

It was both gratifying and disturbing to find this effect. The discovery was gratifying because it permits the explanation of multiple, weak leading edges that are often seen in sweep-frequency backscatter. Examples are shown in Fig. 2, frames (d), (e), (g), (h), (j), (k), (m), (q),

(s), (t), (u), (v), (α), (β), (δ), (ξ), (π), and (σ). Frame (m) is probably the best example. It thus becomes possible to explain these common features by attributing them to small ledges in the ionization profile. One would expect that such ledges should be common since measures of electron density vs height acquired by radio sounding or by rocket probes usually show a profile much rougher than the idealized Chapman layer.

The phenomenon is somewhat disturbing if one anticipates using backscatter sounding as a means for determining the ionospheric structure at a distance. The difficulty arises because multiple leading edges can be caused by this mechanism and also by a number of others. Consequently, the appearance of a multiple leading edge may not be a unique indicator of a particular ionospheric structural form, but it is hoped that analysis will show how to discriminate among the possible causes. Multiple leading edges can be caused by magnetoionic splitting since the ordinary and extraordinary ray families have different skip distances. They may also be caused by the presence of different ionospheric structures on different azimuths. These differences affect the sounding due to the almost unavoidable presence of sidelobes and backlobes in the antenna beam.

Further, the double leading edge can be caused by the separate action of time focusing and range focusing, a factor that has apparently not been recognized before. To see what is meant here, refer to Eq. (1) and notice that the denominator contains both ΔT and ΔR. This means that the power received will be very large when either the time delay between adjacent rays approaches zero or the range difference between adjacent rays approaches zero. It has long been known that ΔR approaches zero at the skip distance, whereas ΔT approaches zero at the minimum time delay and the two do not occur simultaneously (Ref. 10). At any fixed frequency, the first backscatter to be received will be that from minimum time; Peterson has pointed out that this onset of the signal is comparatively strong because of the time focusing, here indicated by ΔT in the denominator of Eq. (1). In addition, when the energy returns later from the skip distance where ΔR approaches zero, there should be another signal enhancement attributable to the focusing of the rays in space. It might be said that the combined action of the antenna and the ionosphere produces an extremely high gain at this particular distance.

Because there are two separate sources of focusing, spatial and temporal, it would be expected that the leading edge would be double. This

effect has not been experimentally observed, partly because the time separation between the enhancements is small, partly because the effect is mixed in with the other three effects previously mentioned, and partly because the theoretical predictions that must precede an experimental test have not been adequately developed.

Because the four clearly distinct phenomena can cause a multiple onset of ground backscatter, investigators should approach with caution the interpretation of a measurement of the leading edge of ground scatter. If data from only a fixed frequency are available, it seems doubtful (to this author, at least) that one could discriminate between the possible causes. Such discrimination may be possible with sweep-frequency data because of differing systematic variations with change of frequency. For example, the magnetoionic effect and the ΔT-ΔR effect must decrease with an increase in frequency, but the synthesis of Fig. 8d shows that the layerlet effect increases with frequency.

The concentric anomaly is unrealistic because it covers the entire path. It seems more likely that such an anomaly would be of limited horizontal extent. One may examine the rays computed from the concentric models to deduce the effect of a limited anomaly, noting that rays that do not pass through the anomaly cannot be influenced by it. Application of this simple logic shows that a "concentric anomaly" of limited horizontal extent would create an extra backscatter leading edge over a limited frequency interval. The ray calculations show that, at lower frequencies, the rays that are able to penetrate to the level of the anomaly leave before reaching the range of the anomaly. When the frequency is too high, the rays that reach the anomaly are not refracted back to the earth.

The experimental data show that the false leading edges usually exist over only a limited interval of frequencies, unlike the synthetic examples. It is possible that most of the experimental measurements of multiple leading edges are attributable to bounded anomalies which are a little more than discontinuities in the electron density vs height profile. These may or may not be moving vertically. Repetitive backscatter records would show vertical motion if it existed, but unfortunately, the experimental data previously mentioned do not contain any multiple leading edges.

V DRAWINGS OF THE FOCUSED RAYS

Once rays are calculated, it is comparatively easy to have them automatically drawn by the plotting equipment that is associated with most large computers. These plots are surprisingly useful because they convey much information in a compact, readily understood way. Three examples showing 18-MHz rays are presented on Fig. 9. Part (a) was computed with the ambient model, and parts (b) and (c) with the outward tilt model. In all three, the bottom line represents the surface of the earth with range marked in 100-km increments. Rays originate at the left side, leaving the earth at successive half degrees of takeoff angle. On each ray is placed a tick mark orthogonal to the ray at every location where the accumulated group delay is a multiple of 100 μsec. From inspection of the pattern of the ticks, one can perceive surfaces of constant delay, which might be considered to indicate the successive positions of a short pulse at 100-μsec intervals. (This plot can be made by use of phase instead of group delay, in which case the surfaces represent wavefronts.)

Signal strength can be deduced from these drawings if one visualizes the rays as flux lines in an energy flow. This concept must be used with moderate caution because it is often incorrect; for example, neighboring rays frequently cross and ray theory does not work in such a circumstance. Nevertheless, the flux line idea works in such a wide region that it is a useful concept.

The rays in the ambient, Fig. 9a, show that the energy strikes the distant ground uniformly in both space and time because both the ray spacings and the delay surface spacings are uniform. When the outward tilt is added, spatial focusing occurs, as shown in Fig. 9b. The rays converge as they strike the ground near 2550 km, causing strong backscatter to be detected from that range. Those rays that take off at low angles and pass through the anomaly on their upward transit strike the ionosphere beyond the anomaly at an angle that is steeper than it would have been in the absence of an anomaly because the rays are refracted downward less while they are in the anomaly since the electron density there is lower than ambient. Since these are "lower rays," steeper incidence produces shorter

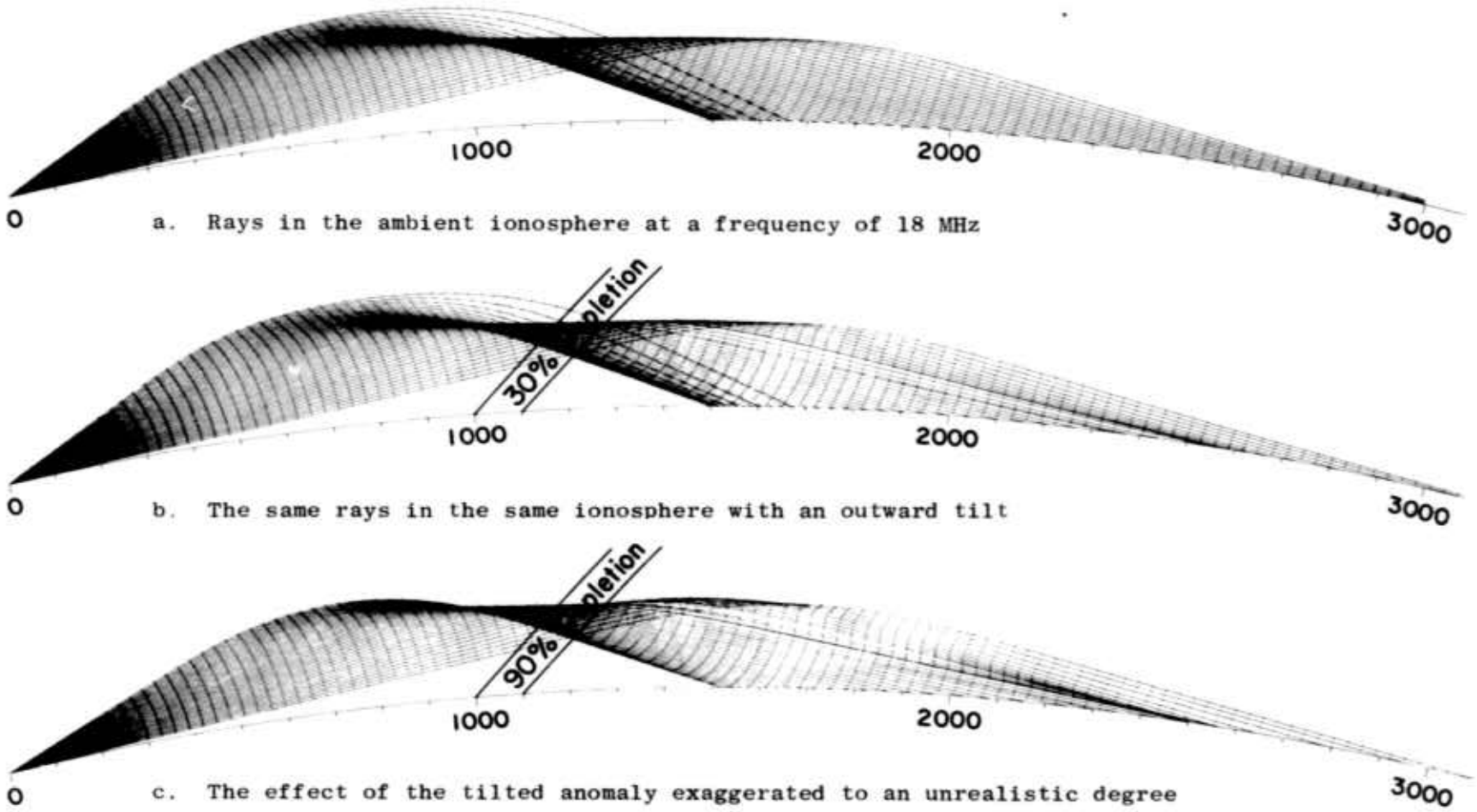

Fig. 9. COMPUTED RAYS WHICH SHOW THE MECHANISM OF FOCUSING. (Ticks are placed on each ray at group delay increments of 100 μsec to show the time distribution of energy.)

range and it can be seen that the low angle rays go a lesser distance because of the anomaly. The rays that encounter the anomaly at apogee are not much affected by it. They still go about 2500 to 2600 km, as they did in the ambient case, although the ray spacing is disturbed. However, the short-range rays that strike the anomaly on their downward leg are not refracted downward as strongly; consequently, they go farther than do their counterparts in the ambient ionosphere.

The combination of rays appears to be focused because the long distance rays are shortened and the short distance rays are lengthened in this manner. To illustrate the mechanism more clearly, Fig. 9 shows the calculation performed with a 90 percent depletion in the outward tilt. This exaggerates the effect to an unrealistic degree but serves to emphasize the distortion in the ray pattern. A few of the higher-angle rays have been left off this plot to clarify the display.

VI ADDITIONAL CALCULATIONS RELATED TO THIS STUDY

A shortened version of the preceding chapters has been submitted to the Journal of Atmospheric and Terrestrial Physics, which will devote a special issue to a symposium at which this paper was presented. (See Acknowledgment for details.) The remainder of this report will be devoted to computational details and additional calculations that will be primarily of interest to specialists who may wish to carry out further work of a similar nature. Those readers who are interested only in the physical significance of the results may choose to skim lightly through the remaining pages.

A. Other Ionospheric Models

Only five ionospheric models were previously mentioned, but many more were used during various phases of this study. Each of these models was assigned a three-digit ionosphere identification (IID) number. This identification system will be introduced here because it will be useful as an aid in tying together the remainder of the data. The ambient model was described in Chapter III; it has IID number 165. The local anomaly was IID 329 and there was also a more exaggerated anomaly of identical shape in which the central density was only 10 percent of ambient; this was IID 254. The outward tilt model was IID 327, and an exaggerated version of it (10 percent central density) was IID 325. Similarly, the inward tilt was IID 328; its exaggerated version was IID 326.

There were four concentric models, one of which had its base at an altitude of 250 km, as previously described. This was IID 320. A second version, IID 319, was identical except that its base altitude was 200 km. There were two variations of this latter model, which were designed to reveal a backscatter detail that will be discussed later. The two variations were IID 341 and 342. To fully specify a concentric model, it is only necessary to present a plot of electron density vs altitude. Four such plots given on Fig 10 thus fully define the four concentric anomalies. Table 1 summarizes all these IID numbers.

Chapter III provided descriptions of IID 165, 329, 327, 328, and 320, in that order. The rayplots of Fig. 9 were calculated from models 165,

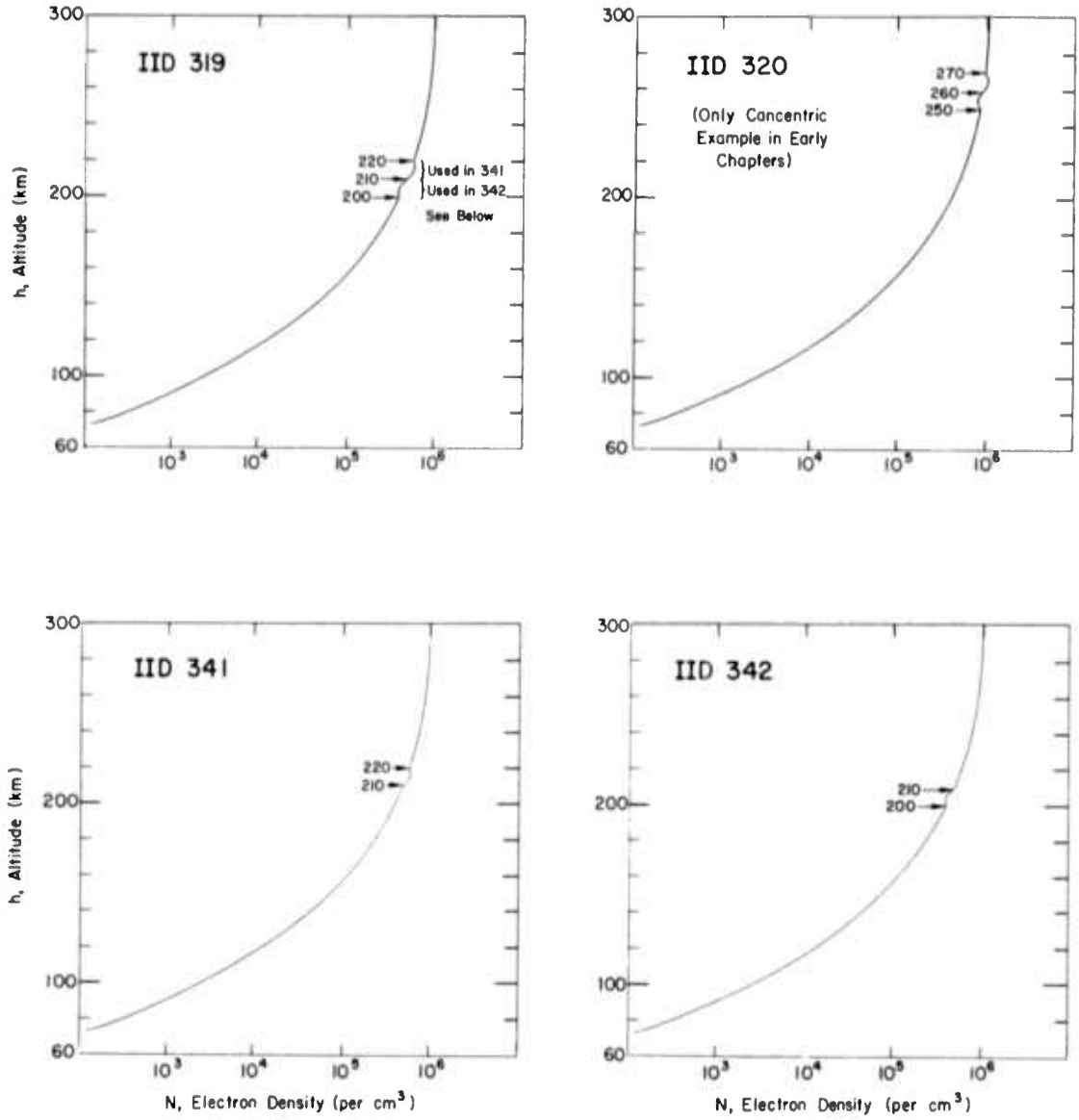

Fig. 10. FOUR CONCENTRIC ANOMALY MODELS.

327, and 325. In addition to the models outlined in Table 1, the local and tilted anomalies were tried with a central density of 90 percent of ambient. These models did not produce ray disturbances sufficiently strong to permit the easy identification of anomalous effects. Apparently, the noise in the computation is comparable to the effect of the 90 percent anomalies and presumably this could have been remedied by calculating with smaller steps.

Table 1

SUMMARY OF IID NUMBERS

IID Number	Description	
165*	Ambient Chapman Layer	
329*	Local Anomaly, Central ρ/ρ_o = 70%	
254	Local Anomaly, Central ρ/ρ_o = 10%	
327*	Outward Tilt, Central ρ/ρ_c = 70%	
325	Outward Tilt, Central ρ/ρ_c = 10%	
328*	Inward Tilt, Central ρ/ρ_o = 70%	
326	Inward Tilt, Central ρ/ρ_o = 10%	
320*	Concentric Anomalies ("Cycle" refers to Sine Wave of Fig. 7a)	Full Cycle, Base at 250 km
319		Full Cycle, Base at 200 km
341		Half Cycle, Top Half of IID 319
342		Half Cycle, Bottom Half of IID 319

*Described in Chapter III

It should be noticed that the local and tilted anomalies are all regions in which the electron density is more rarified than in the ambient model. In general, radio rays are refracted away from regions of electron concentration and thus the rays would be drawn toward the center of a rarified region and it would act as a converging lens acts upon light. The idea of a rarified region is sketched in Fig. 11a. In part (b) of the figure is shown a dense region in which one would expect that the rays would diverge. This was not simulated in this study and so, in a sense, we have attacked only one of the two fundamental types of anomaly. The limitation does not apply to the concentric models, which contain mixtures of over- and under-dense regions.

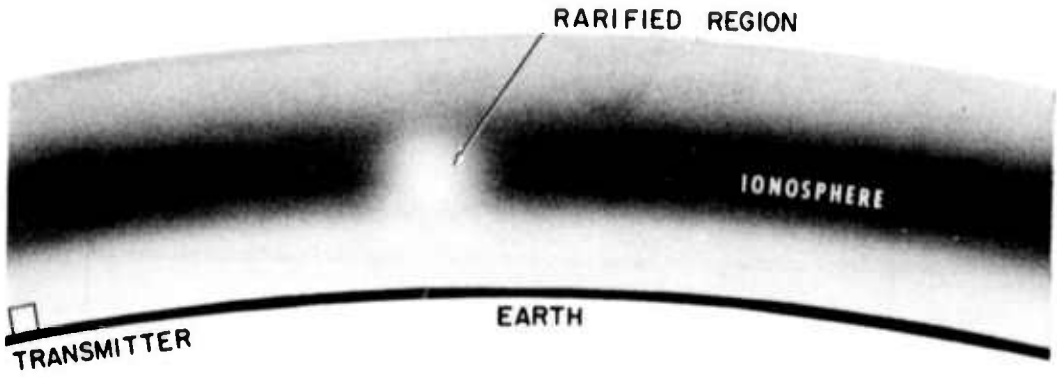

a. Rarified anomaly in which passing rays are refracted toward the center

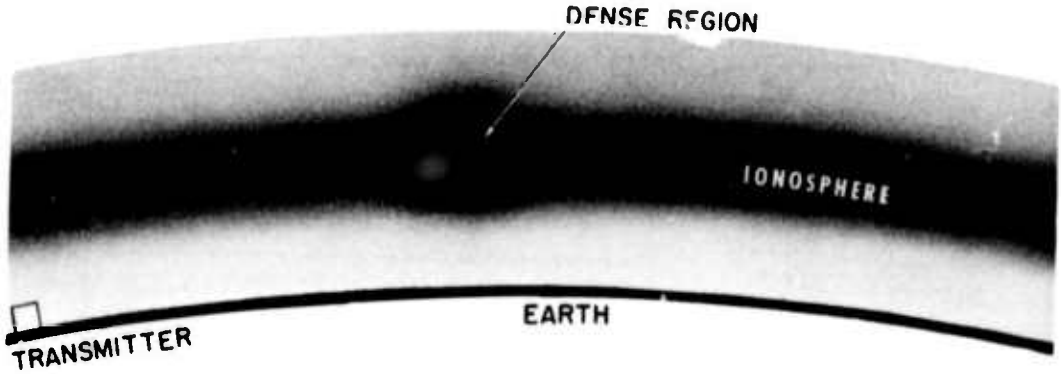

b. Dense anomaly in which rays refract away from the center

Fig. 11. TWO TYPES OF ANOMALIES.

B. Drawings of Rays in Various Anomalies

One of the most useful forms of computer output is the ray drawing, examples of which have been presented in Fig. 9. The main advantage of this form of output apparently stems from the fact that the data format is intuitively obvious. The main limitation of this form of data is that it shows effects for only a single frequency on a single plot. The ray drawings also suffer from the disadvantage that they cannot show very small perturbations in pattern uniformity because the drawing is necessarily analog and the scale is quite large.

To show frequency effects, one can show a number of ray drawings in the same ionosphere at different frequencies. This technique is used on Fig. 12, which shows rays at 5 frequencies in IID 329, the local anomaly with a central density 70 percent of ambient. In the third and fourth plots on this drawing, it will be noticed that the rays do not emanate from a single point and that they do not return to the earth but rather miss it by a few kilometers. These are two manifestations of an error in placement of the plotting pen on the paper. The numerical data computed for these rays were unaffected by this source of error. The first and third plots on the page lack any upper rays but, again, this is not a significant deficiency because the other rays were calculated at a different time and thus they could not be put on the same plot.

One can more readily see the significant effects on these plots by placing the eye near the plane of the paper on the right side and looking back lengthwise along the plot. This has the effect of compressing the horizontal axis and emphasizes vertical discontinuities. For oblique rays such as this, most of the refraction effects show up as vertical changes. In addition, however, there are changes in the time distribution of energy which can be seen in the pattern of tick marks. For example, at the discontinuity in the ray pattern, there is also a transverse shift in the time mark pattern, indicating that the energy that impinges on the ground is not only focused spatially but is also redistributed in time. Since the backscatter measurements are influenced by both temporal and spatial variations, the interruption in the smooth tick mark patterns is significant in an analysis of backscatter.

The top drawing on Fig. 12 was made with the local anomaly located at a distance of only 1000 km. The remaining four ray drawings had the anomaly located at 1200 km. The region of maximum ray pattern discontinuity is roughly twice the distance of the anomaly itself, except in the 26-MHz example where the skip distance exceeded 2×1200 km.

Figure 13 shows rays in the exaggerated local anomaly, IID 254. In all four cases illustrated, the anomaly was only 1000 km from the transmitter. By again sighting lengthwise down the drawings, it is easier to see the reason for the specific form of the ray discontinuities. There appears to be a considerable randomness in the ray pattern in this set of

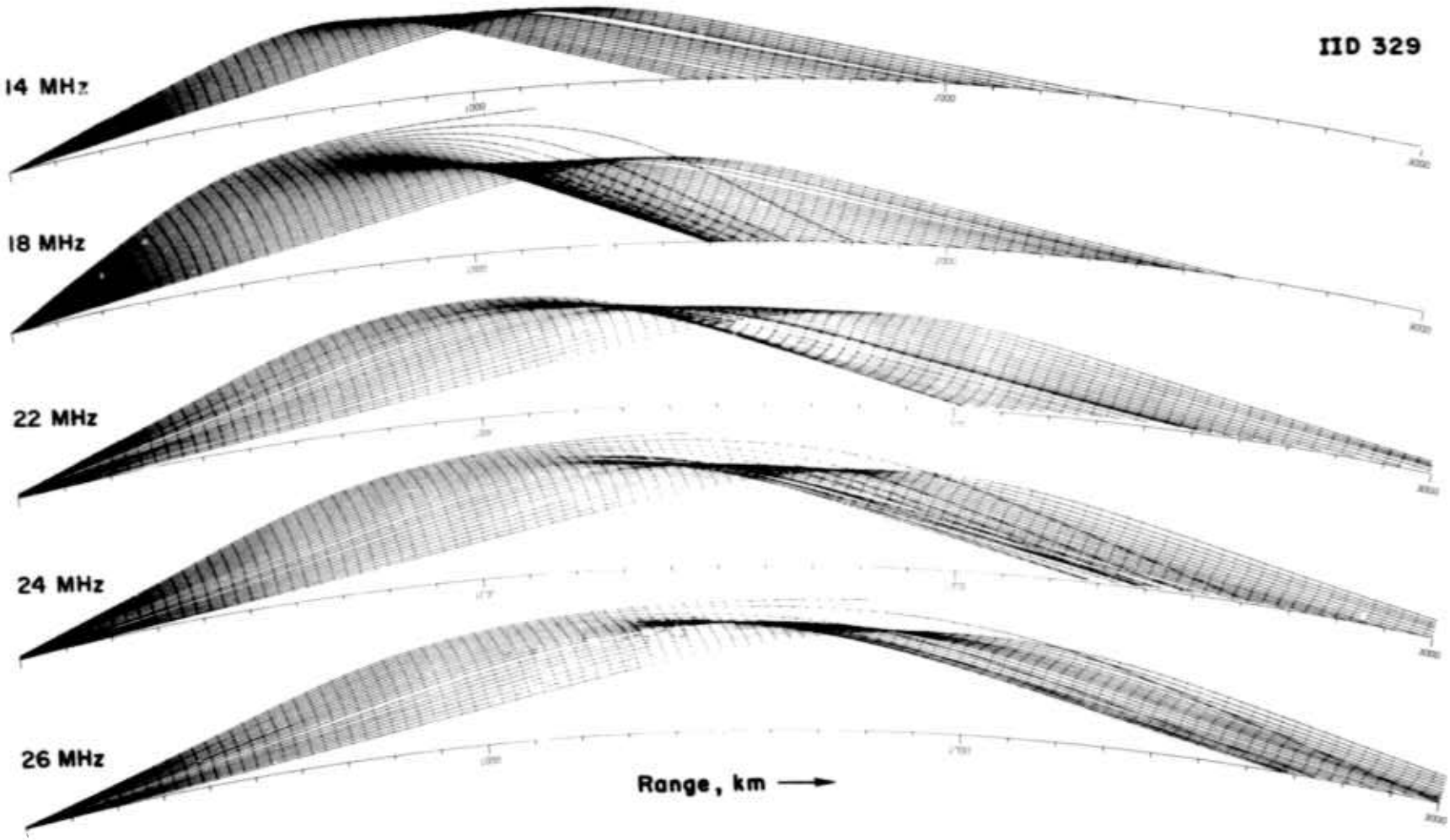

Fig. 12. RAYS IN THE LOCAL ANOMALY.

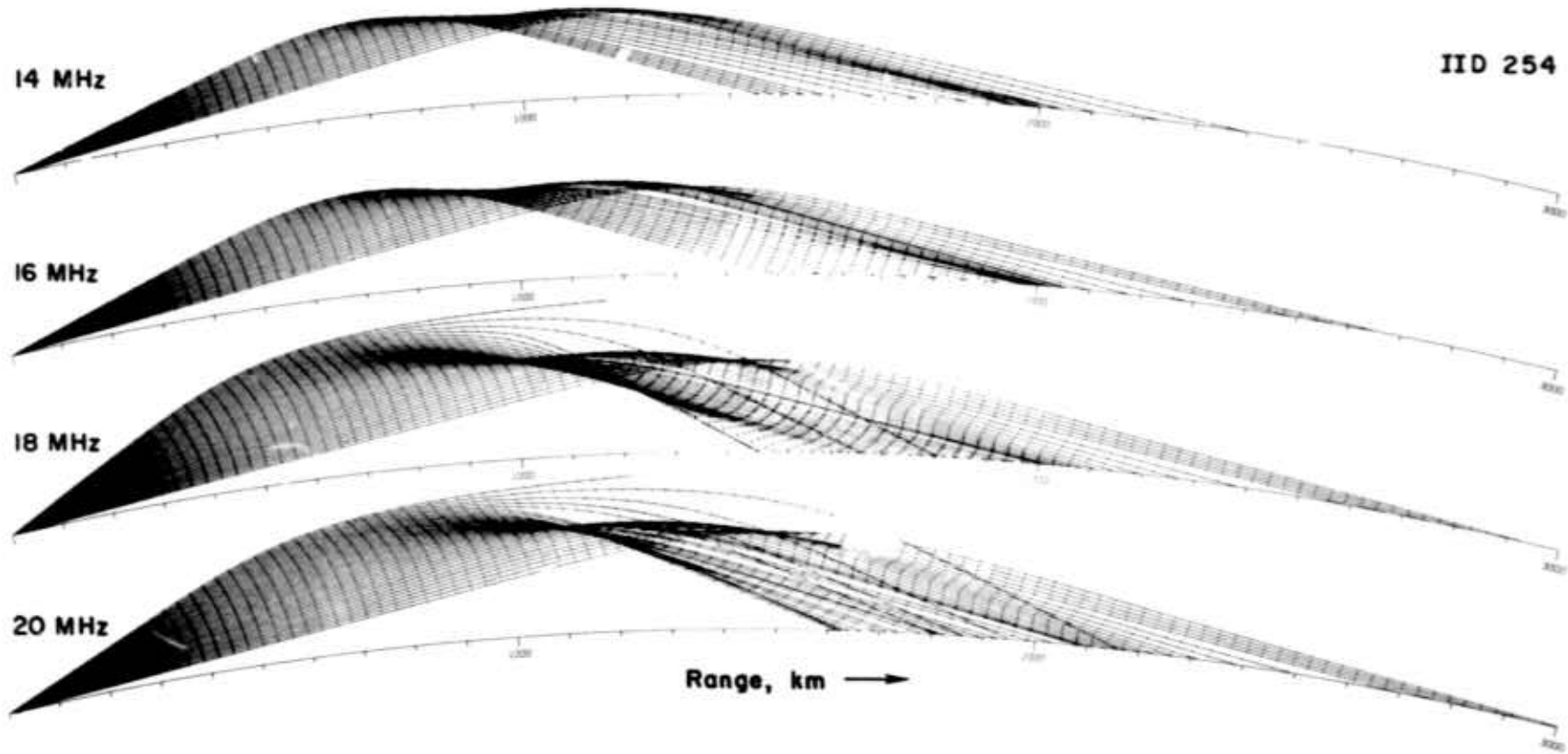

Fig. 13. RAYS IN THE EXAGGERATED LOCAL ANOMALY.

calculations. These rays were traced by a computer program, which makes an approximation that does not work well when the electron density is high and its gradient is also large and nearly horizontal. The 10 percent anomaly models (IID 254, 325, and 326) probably represent a case in which this raytracing program has marginal usefulness because these models possess severe horizontal gradients that may account for the disorder in these rays. Nevertheless, by examining them, one can clearly see the tendency of the rays to refract toward the centerline of the anomaly which has its center at an altitude of 200 km and at a range of 1000 km.

To understand this refraction effect, one must appreciate the difference between upper and lower rays. These two types of rays are usually not well defined but the author has found the following definition to be useful: If a ray in a given layer would have a shorter range if its takeoff angle were increased, then that ray is a lower ray. If the hypothetical increase in takeoff angle produced an increase in range, then the ray is an upper ray. Stated mathematically, a lower ray has a negative $dR/d\beta$ while an upper ray has a positive $dR/d\beta$.

To apply this upper ray-lower ray reasoning to the drawings of Fig. 13, notice that a ray that is traveling along an upward leg of an ionospheric transit may be refracted either upward or downward by the local anomaly, depending on whether it passes above or below the anomaly centerline. If the ray is refracted upward, then it enters a trajectory that corresponds to a higher takeoff angle. Therefore, if a ray is a lower ray and is refracted upward, its range will be shortened. Thus we see that there are two binary criteria and consequently there are four possible cases:

(1) A lower ray refracted upward will have decreased range.

(2) A lower ray refracted downward will have increased range.

(3) An upper ray refracted downward will have decreased range.

(4) An upper ray refracted upward will have increased range.

These relations usually hold true, but in some cases the refraction may actually change a ray from upper to lower. As a consequence, the reasoning becomes comparatively complex when the anomaly under study sits at half the skip distance, because then the rays that pass through the anomaly are readily changed from upper to lower (or vice versa) by a slight

refraction. Early attempts by the author to calculate rays in local anomalies led to some confusion which may now, with hindsight, be partly attributed to positioning of the anomaly at half the skip distance. This destroys the simple patterns of ray disturbance that have been shown in the preceding calculations. It may be that the anomaly effects on rays really do disappear at short ranges, for examination of the backscatter records included in this report will show that there are not many streaks at short ranges. Most are beyond 600 km.

With the above thoughts in mind, examine the 20-MHz rays on Fig. 13. Notice that the locus of apogees appears to follow three separate arcs. The first arc has its peak at a range of about 900 km, the second arc peaks at about 1250 km, and the third arc peaks at about 1600 km. These three arcs intersect at roughly 1100 and 1500 km. The farthest arc is composed of those rays that miss the anomaly altogether, having passed underneath. The middle arc is composed of the apogees of those rays that passed through the bottom half of the anomaly. Notice the pattern where these rays strike the ground. There is a deficiency of energy from about 2300 to about 2700 km where the rays diverge from one another. The cause of this divergence can be traced backward to the anomaly where it is seen that the rays are being drawn inward toward the center of the anomaly, that is, refracted upward. Thus, as the original takeoff angle at the starting point gradually increases, the range gradually decreases until the rays begin to strike the anomaly. Then the effective takeoff angle increases still more rapidly so that the ground range decreases still more rapidly and this leads to the deficiency of energy seen in the plot.

The shortest-range arc of apogees is formed of those rays that pass through the top of the anomaly. The pattern of these rays on the ground is not so well defined because they strike near the skip distance where slight deviations change the rays from upper to lower or vice versa. The local refraction of the rays while they are in the anomaly can clearly be seen in the upper rays at 18 and 20 MHz. Because the local anomaly is of parabolic cross section (in electron density vs distance), the highest electron density gradient occurs at the outer edge of the anomaly; this is where the inward refraction will be highest. Thus the downward refraction of the upper rays is clearly seen to occur at an altitude just short

of 250 km at a range just beyond 1000 km where the rays are rotated about the inner rim of the circular anomaly.

Figure 14 shows a large number of rays in the outward tilt These are the same rays that were used to make the synthetic backscatter of

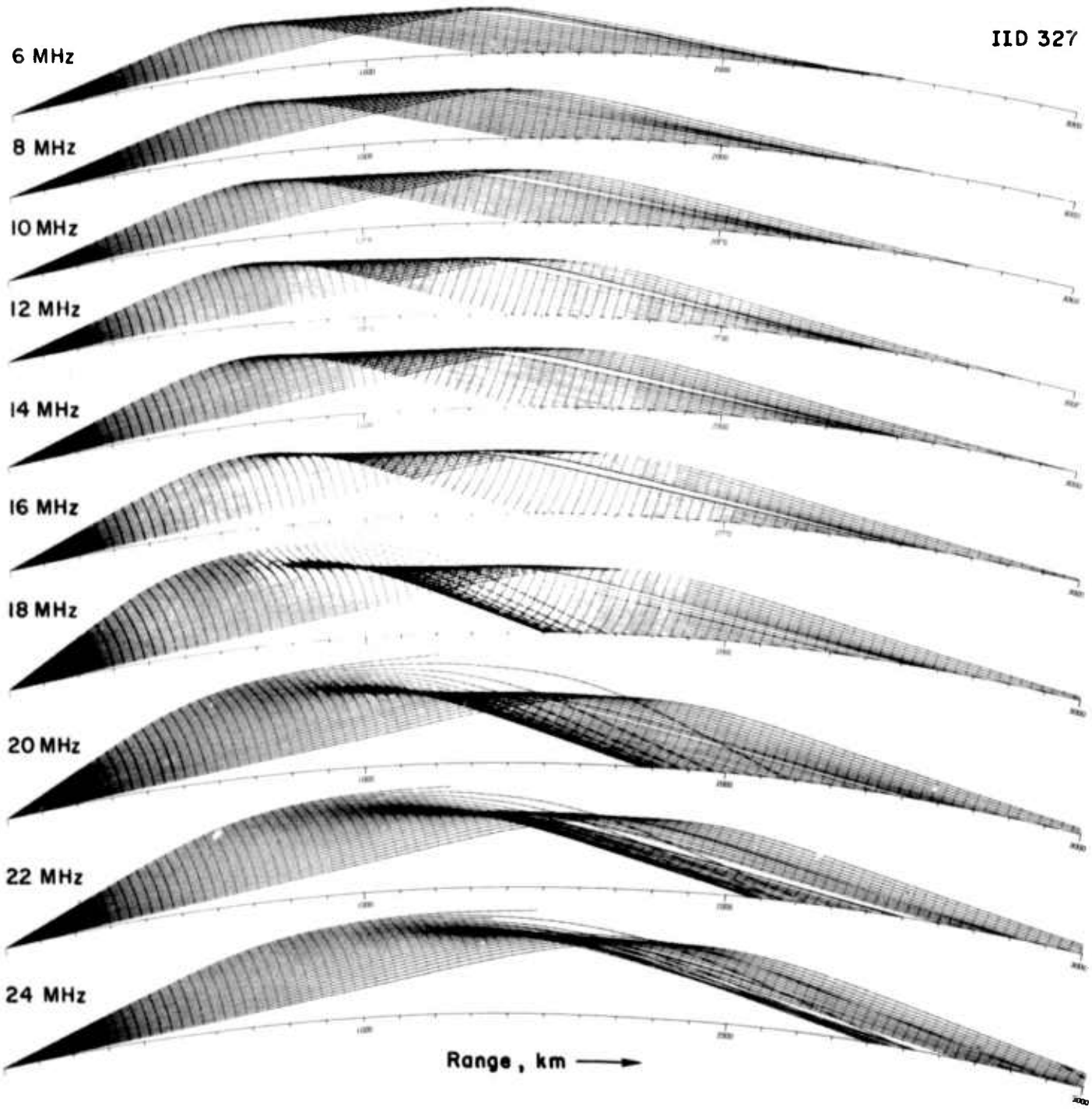

Fig. 14. RAYS IN THE OUTWARD TILT.

Fig. 8b. The 18-MHz example was also shown as part (b) of Fig. 9. From this family of rays, one can see the tendency for the range of the focusing region to increase with increasing frequency. It is also possible to gain some insight about the focusing mechanism, although this is more easily done with the ray drawings of Fig. 15 computed in the exaggerated equivalent of the same ionospheric model. Here, fewer rays are shown and also the upper rays are not included. The 18-MHz example is the same as that which was shown as part (c) of Fig. 9. By sighting lengthwise along the line of apogees, one can see an upward bulge in each ray family just beyond the region where the outward tilted anomaly passes through the apogees. Using the upper ray-lower ray guidelines given above, one can deduce the mechanism of focusing. This was described at length during the discussion of Fig. 9, but it is perhaps more clearly illustrated here where several examples can be compared. The basic reason for the upward bulge in the line of apogees is the fact that the electron density decreased so that in this region there was less barrier to the penetration of rays.

Figure 16 shows a number of ray calculations in the inward tilt model, IID 328. This should be compared to Fig. 14 to see the decrease in range of ray-focusing vs frequency as contrasted to the increase when the anomaly has an outward tilt. The exaggerated anomaly, IID 326, was used to generate the rays given on Fig. 17, which should be compared with Fig 15. By again examining the line of apogees, one can see the qualitative difference between the rays in the inward tilt and those in the outward tilt. The inward tilted anomaly is inclined toward the rays and so the beginning of its effect tends to be more abrupt while its ending tends to be more smooth than the corresponding features in the apogee lines on Fig. 15. To see this, notice that the upward bulge in the apogee lines on Fig. 15 is almost symmetric with respect to the bulge centerline. In Fig. 17, the upward bulge has a comparatively sharp left side, but the right side is so gradual that it is not clearly defined. Except for this minor difference, the focusing mechanism for the two kinds of tilted anomalies appears to be essentially identical.

Figure 18 shows an interesting comparison of rays at the same frequency in several different models. As a reference standard, the top figure shows rays in the ambient ionosphere and the upper rays have been deleted

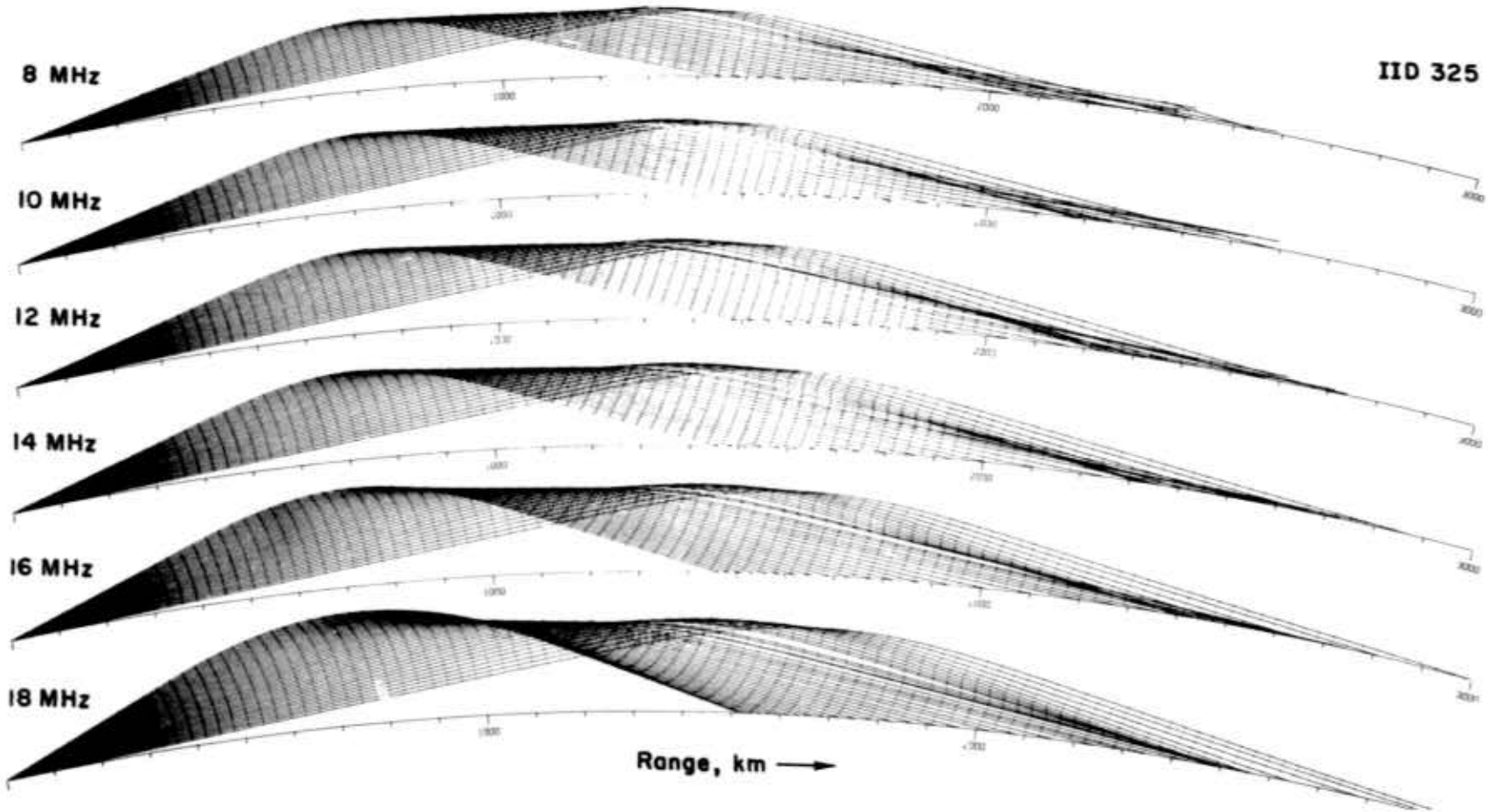

Fig. 15. RAYS IN THE EXAGGERATED OUTWARD TILT.

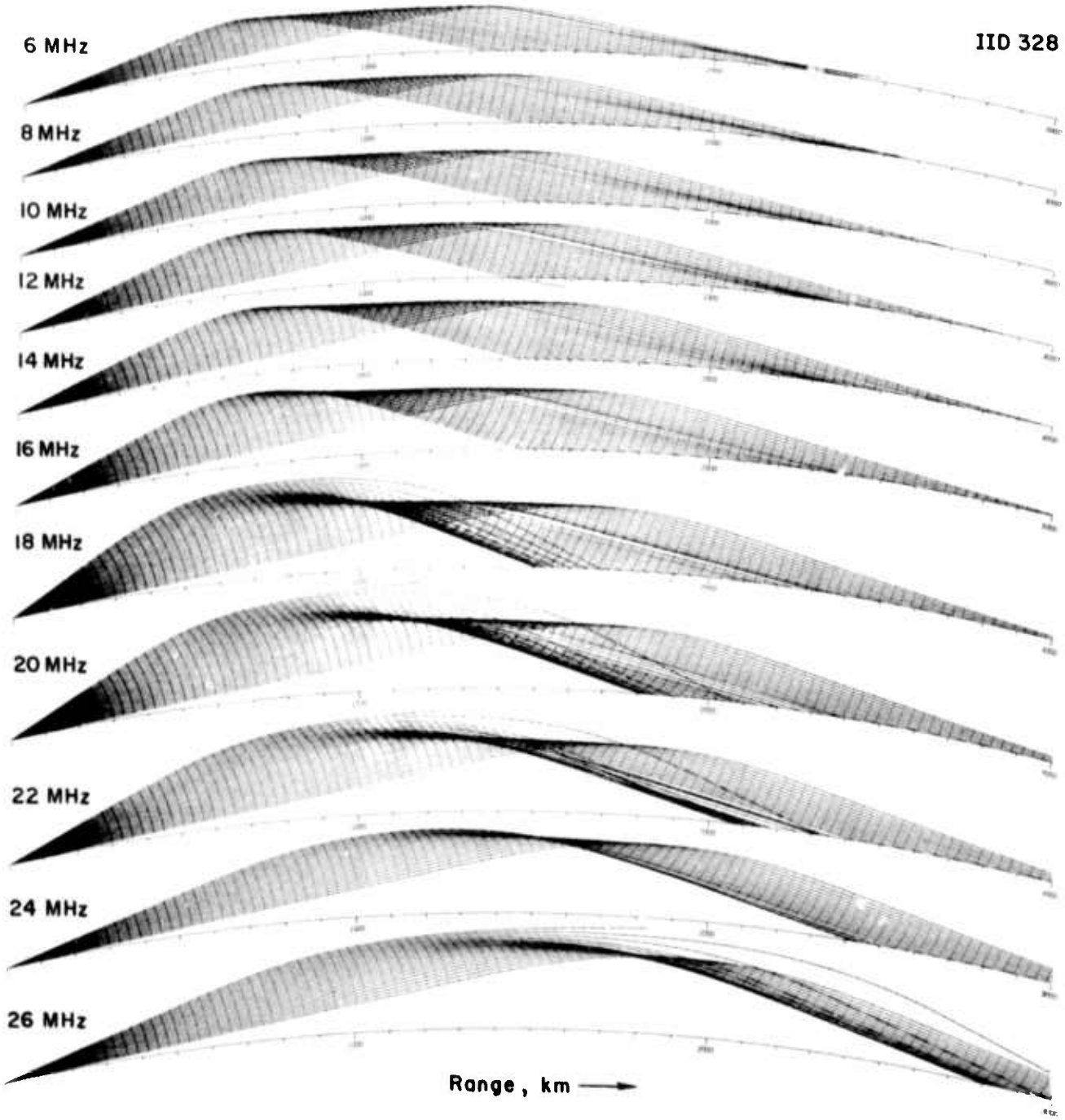

Fig. 16. RAYS IN THE INWARD TILT.

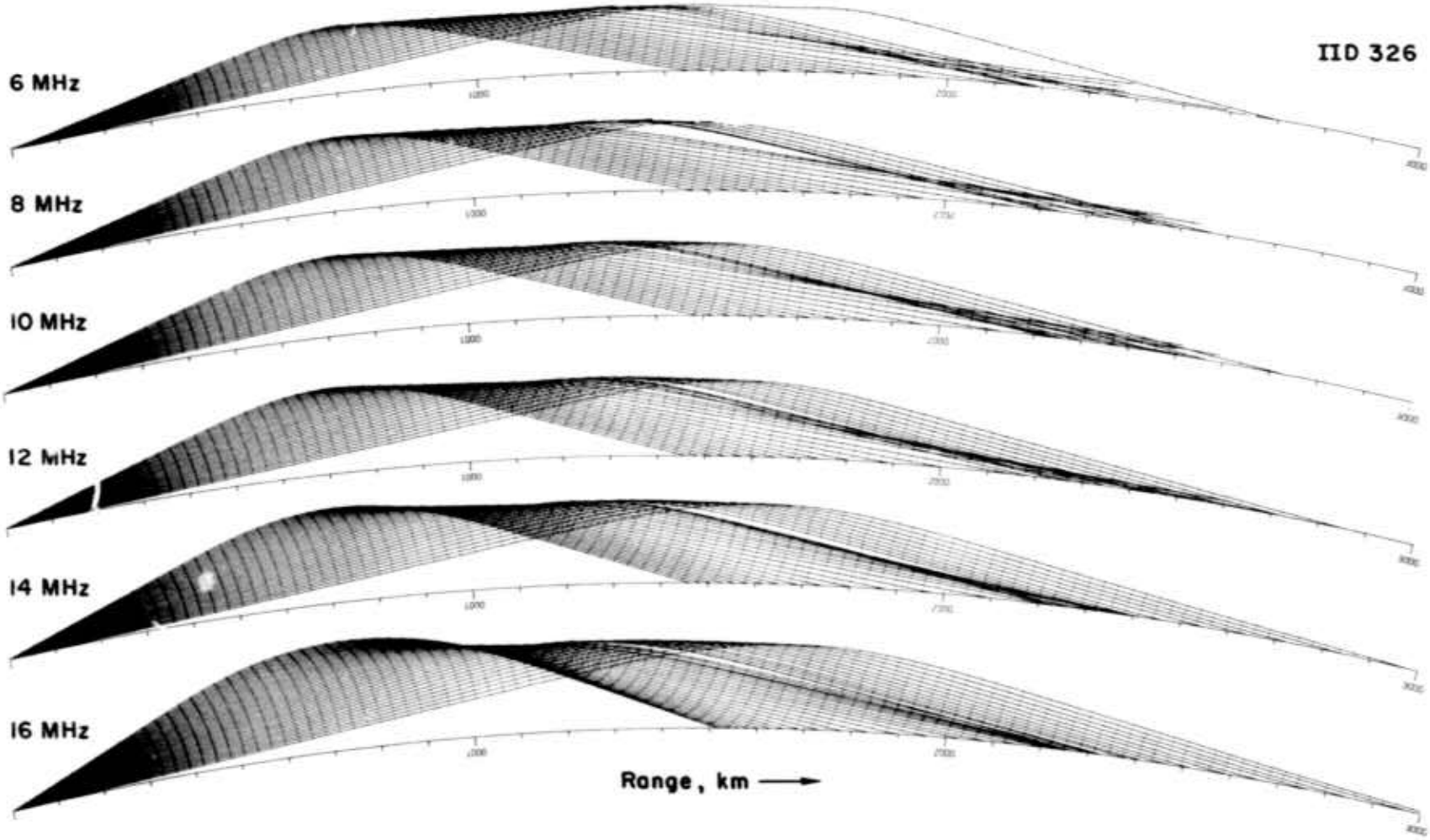

Fig. 17. RAYS IN THE EXAGGERATED INWARD TILT.

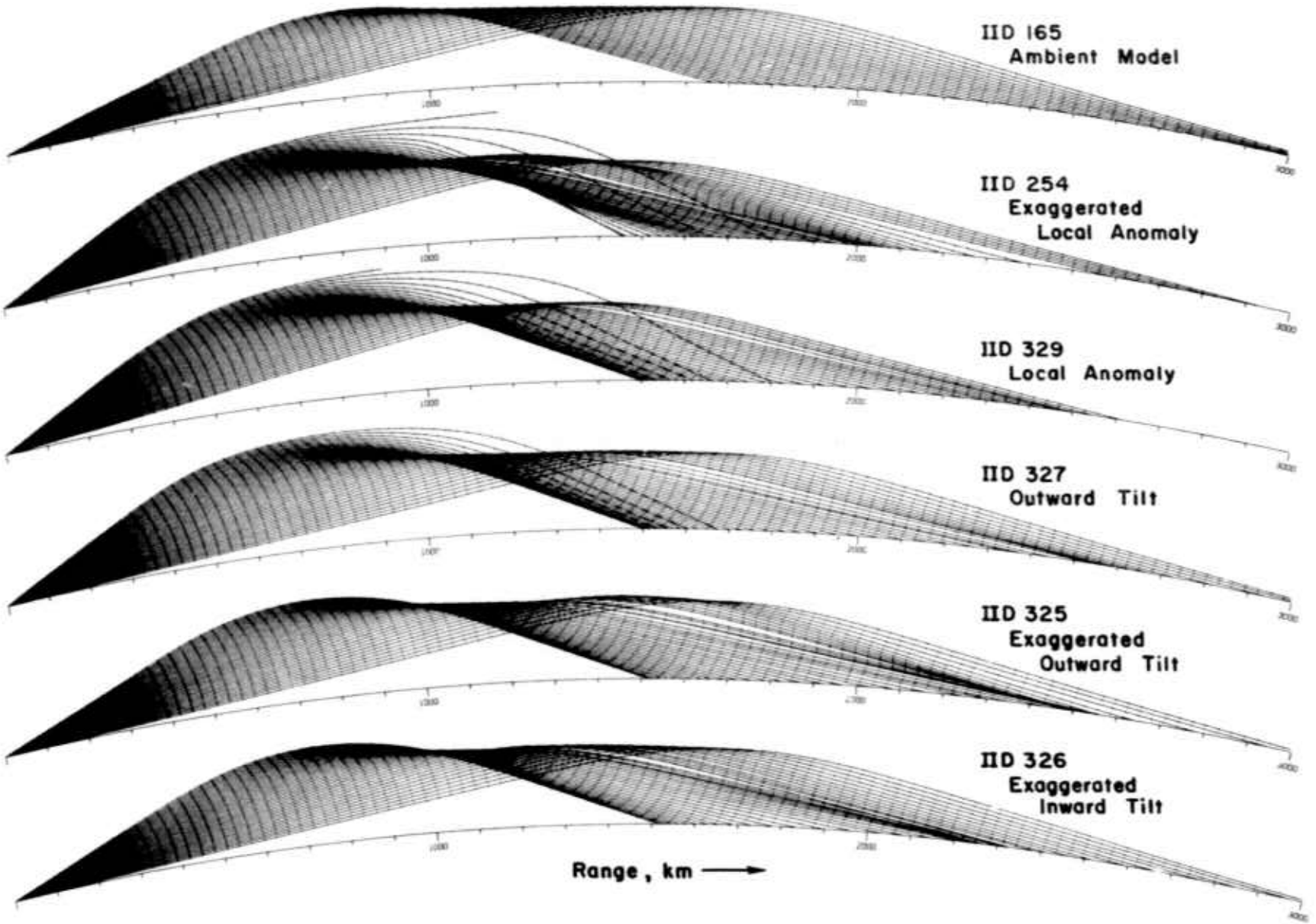

Fig. 18. RAYS AT 18 MHz IN MANY DIFFERENT IONOSPHERIC MODELS.

in order to emphasize the uniformity in the lower ray family. It is possible to detect some slight jitter in these rays; all such jitter is due to computation defects. The programmed calculation was identical to that used in producing the other ray drawings of this report.

Comparison of the lines of apogees for the three models with a 10 percent central density will serve to emphasize the three different qualitative behaviors of the rays in the three different anomaly types. For the local anomaly, the line of apogees is formed of three arcs. With the outward tilt, the line of apogees has a single upward hump, which is roughly symmetric about its own centerline. For the inward tilt, the hump in the line of apogees is sharply defined on the left side but less well defined on the right.

C. Backscatter under Various Circumstances

The set of backscatter calculations presented in Chapter IV had a logarithmic frequency scale and a dynamic range of 30 dB. Many other calculations have been carried out; some of the more useful examples will be presented here. There are three additional classes of backscatter records:

(1) backscatter from other ionospheric models besides those used in Chapter IV,

(2) calculations with the dynamic range set at 60 dB, and

(3) display with a linear frequency scale that changes the apparent echo shape.

Figure 19 shows backscatter from the exaggerated versions of the first three anomalies used to generate Fig. 8. All the calculation parameters are the same and the figure layout is similar, to facilitate comparison, but calculations in the exaggerated anomalies were carried out only at frequencies of 12, 14, 16, 18, and 20 MHz. (The program that plots the backscatter automatically adjusts the amplitude of each single-frequency record so that it has an abscissa span equal to that of a single megahertz.) It can be seen that the exaggerated anomaly creates a very strong disturbance in the backscatter, so strong in fact that there is no longer a clearly identifiable streak present.

Figure 20 shows the backscatter obtained with three different concentric anomalies. Part (a) of the figure shows the result when the

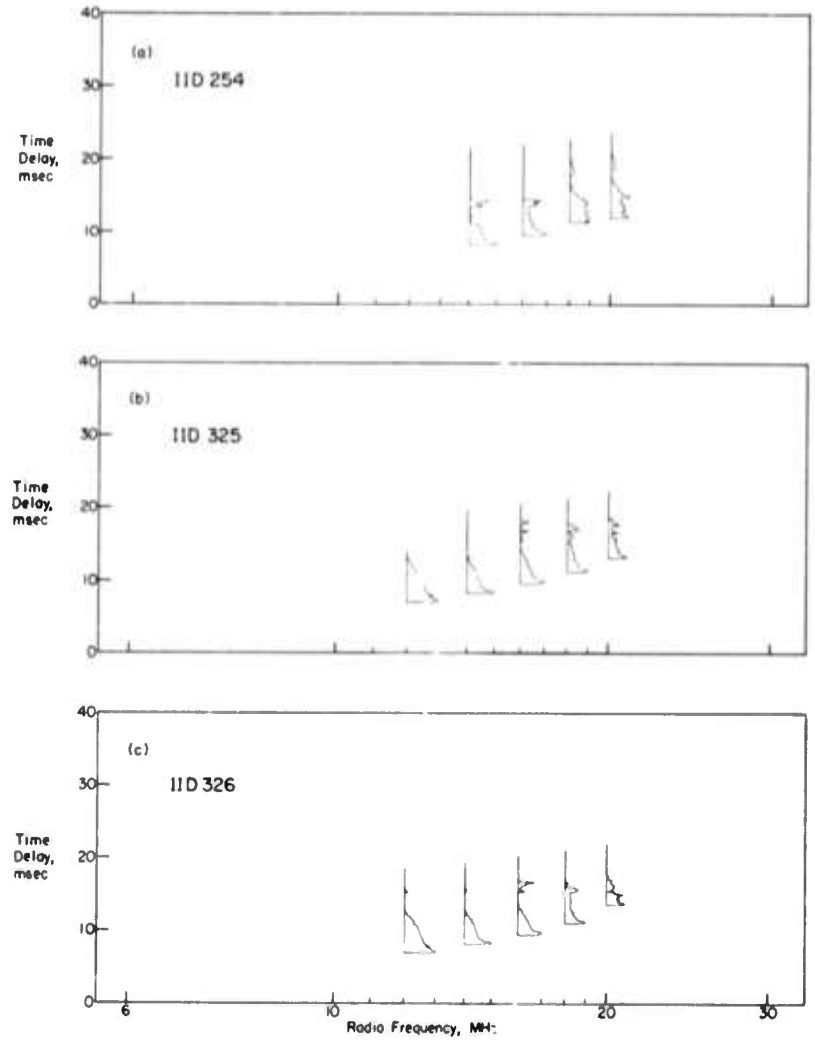

Fig. 19. BACKSCATTER IN THE EXAGGERATED ANOMALIES. (a) With the exaggerated local anomaly; (b) with the exaggerated outward tilt; and (c) with the exaggerated inward tilt.

full-cycle sinusoid density multiplier of Fig. 7a is moved downward 50 km relative to the location which was previously described. The backscatter computed with this model is shown in Fig. 20a and should be compared to that shown in Fig. 8d, which is otherwise the same. Notice that there are two major new effects on Fig. 20a, not on Fig. 8d:

(1) The false leading edge appears at a lower frequency, but the reduction in minimum time delay is not nearly as marked at the high frequencies. In fact, the effect of the anomaly practically disappears above 25 MHz in Fig. 20a, whereas the effect

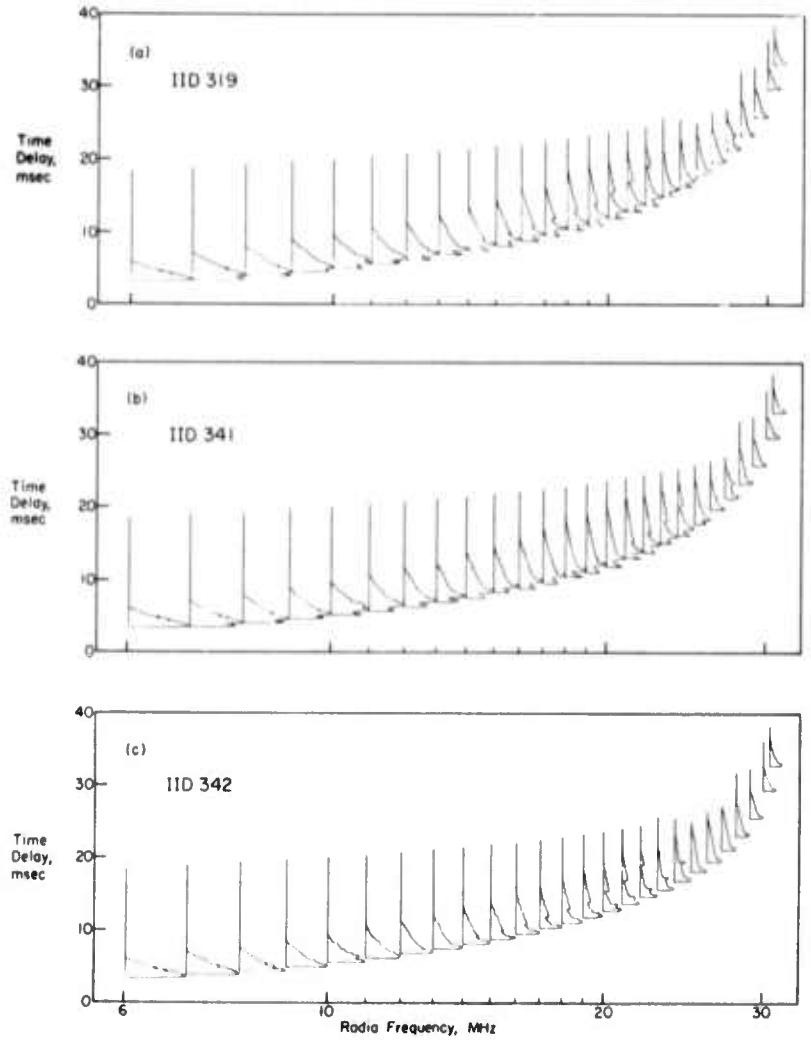

Fig. 20. BACKSCATTER IN OTHER CONCENTRIC ANOMALIES. (a) Full sinusoid multiplier with base at 200 km; (b) positive half cycle of sinusoid, electrons added above 210 km; and (c) negative half cycle of sinusoid, electrons deleted above 200 km.

of the anomaly exerted dominant control over the backscatter at high frequencies in Fig. 8d. This different relative behavior is attributable to the fact that the higher frequency rays have higher apogees, which are more strongly influenced by the higher anomaly.

(2) There is another apparent leading edge within the body of the backscatter, which first appears at approximately 13 MHz just beyond the strongest peak in the backscatter. At higher frequencies, the effect becomes more pronounced, and its time delay is more rapidly increasing with respect to frequency than that of either of the other two signal enhancements. The effect finally disappears at 23 MHz.

In an effort to understand why these two separate effects should occur, the raysets were examined and the pattern of the numbers appeared to indicate that the first leading edge could be attributed solely to the positive half cycle of the sinusoid, while the last leading edge could be attributed to the negative half cycle (that is, to the rarefaction). It is difficult to be certain of this cause-effect relation from an examination of tabulated numbers, and so a check was conducted by making two ionospheric models, one with the positive half cycle and the other with a negative half cycle. These are IID 341 and 342, which have previously been described.

With the positive half cycle (electrons added between 210 and 220 km), we obtained the backscatter shown on Fig. 20b. With the negative half cycle (electrons removed between 200 and 210 km), we obtained the backscatter of Fig. 20c. Comparison of these two backscatter plots with that of Fig. 20a shows that there is indeed a tendency for the positive half cycle to produce the added leading edge at shortest time delay and for the negative half cycle to produce only the longest time delay effect. However, the separation of the two effects is not complete. In Fig. 20b, there is some evidence of a third leading edge, which begins at 19 MHz and extends up through 24 MHz, a higher frequency than before. In Fig. 20c, the fully developed effect is seen just as it was in part (a) of the figure, but in addition there is a new signal enhancement, which appears at 19 MHz and can clearly be identified through 24 MHz.

In some of the charts that follow, raypath parameter relations will be presented which will clarify the mechanisms underlying these backscatter discontinuities. At this point, we have only seen that if we insert a particular ionospheric model into the computer, out comes a new and different backscatter anomaly.

Backscatter with 60-dB Dynamic Range. In Chapter II, Part C, it was explained that the backscatter simulation program has a variable "dynamic range," which, in fact, controls the total number of decibels of the computed backscatter that will be presented on the display. After the amplitude is computed at each fixed frequency, all other amplitudes are compared with the maximum. If the dynamic range setting is 30 dB, for example, then the computer is instructed to discard any echo that is not within 30 dB of the maximum. For example, if the peak backscatter

echo power were 10^{-7} W, then the display would present only echo components that exceed 10^{-10} W, that is, 30 dB less than 10^{-7}.

All of the preceding data has been calculated with a dynamic range setting of 30 dB. In this section, we will show many of the same records calculated with a 60-dB setting. This tends to produce unrealistic effects because the approximate backscatter simulation technique introduces larger errors than does the more rigorous technique described in Ref. 1. Nevertheless, the 60-dB setting can be useful because some of the echo components lie between 30 and 60 dB. The sharp trailing edges seen in the 60-dB backscatter are not real but are caused by approximations. In most of this backscatter, the amplitude should die off gradually with increasing time delay, much as it appears to do on the 30-dB records. By computing the original rays with a finer integration step and using finer time steps in the backscatter synthesis, it should be possible to achieve better realism in the 60-dB records by use of these same programs without any modification. However, we have not attempted to do this since it is our general practice to use the more rigorous backscatter simulation technique for the examination of smaller details.

Figure 21a shows 60-dB backscatter in the ambient model and can best be compared to the example shown in Fig. 5. At the higher frequencies on the 60-dB model, it is seen that the trailing edge has the artificial sharp cutoff previously mentioned. Also, at the low signal levels at the lower frequencies, it is clear that the stairstep structure in the echo amplitude vs time delay is attributable to the finite number of rays that were calculated. Neither of these effects would appear if we had calculated a very large number of rays originally. It can be seen from Fig. 5 that the calculation parameters were adequate for a 30-dB presentation, however.

Parts (b), (c) and (d) of Fig. 21 should be compared with Fig. 8. With a higher dynamic range, it is possible to see the streak structures over a wider frequency range. For example, in the outward and inward tilts, the streak is present at 8 MHz but it is so weak that it can be seen only on the records with a higher dynamic range. Similarly, the local anomaly creates a weak effect at 12 MHz, which is seen only on the 60-dB record.

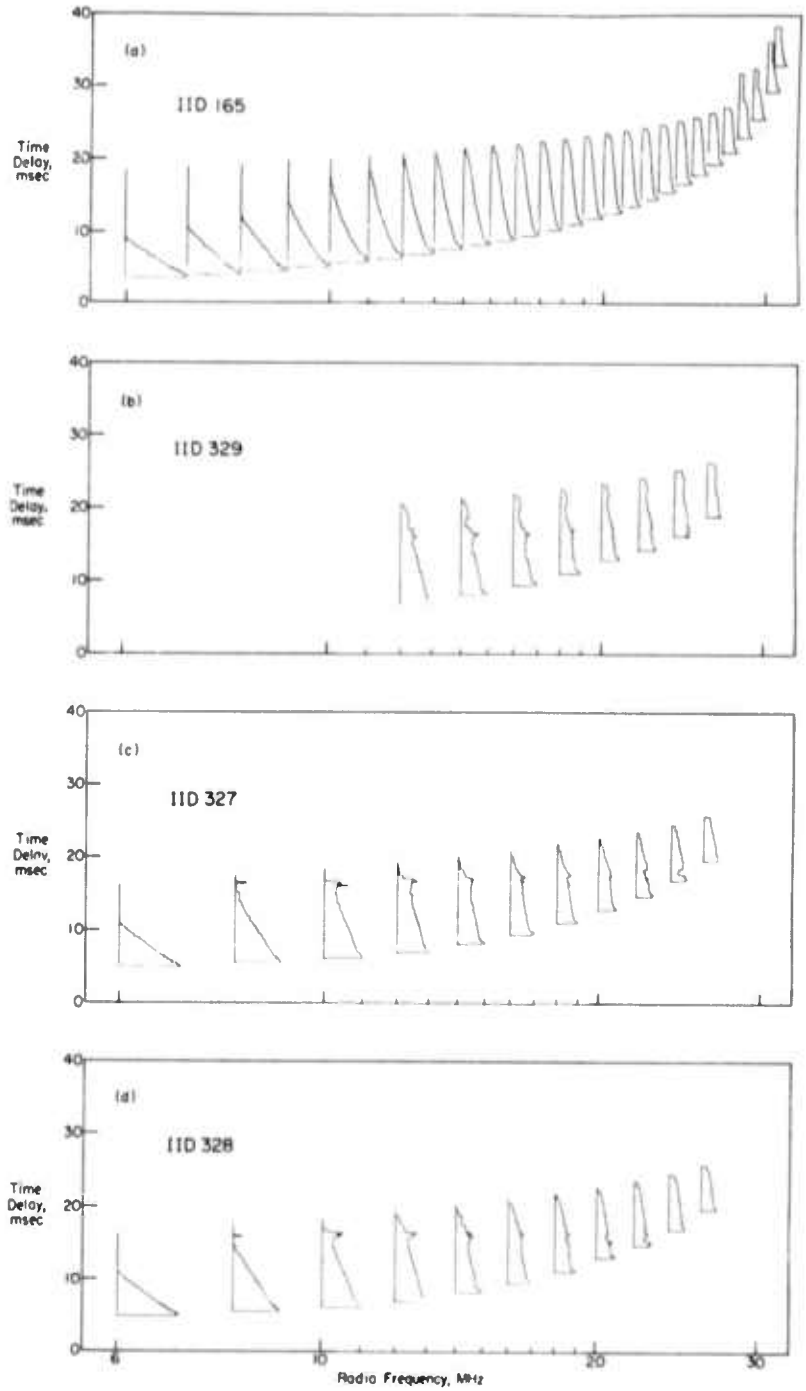

Fig. 21. BACKSCATTER IN AMBIENT AND LOCALIZED ANOMALIES WITH 60 dB DISPLAYED. (a) With the ambient ionospheric model; (b) with the local anomaly; (c) with the outward tilt; and (d) with the inward tilt.

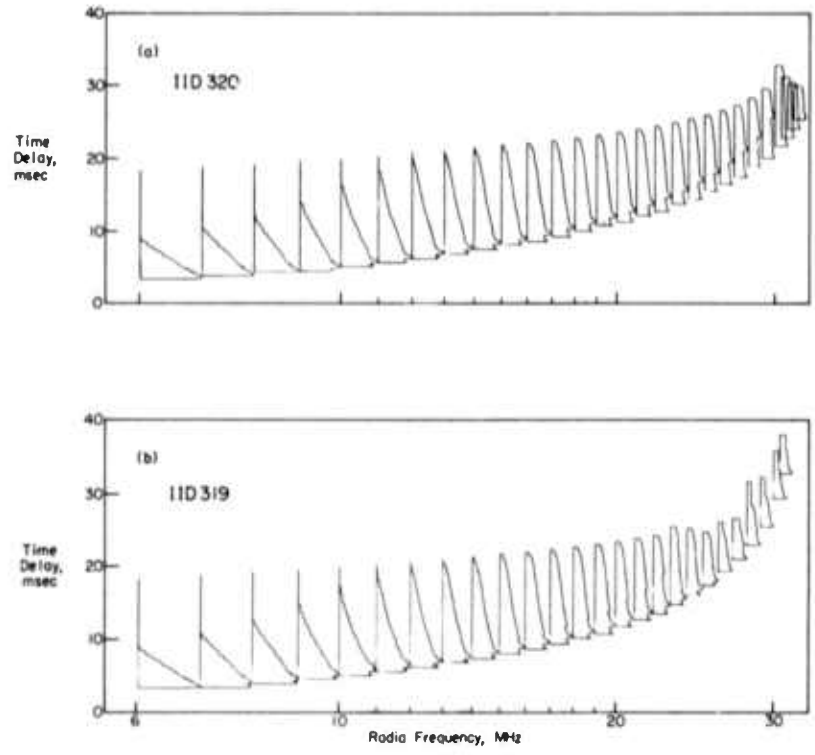

Fig. 22. BACKSCATTER WITH CONCENTRIC IONOSPHERIC MODELS DISPLAYED TO 60 dB. (a) With the full cycle sinusoid based above 250 km and (b) with the full cycle sinusoid based above 200 km.

Figure 22 shows 60-dB backscatter in the two concentric ionospheres, one with the anomaly based at 250 km and the other with the anomaly based at 200 km. Little additional information is seen on these records; they serve but to show that the 30-dB dynamic range setting was a better choice. In fact, on part (b) of Fig. 22, the third signal onset is just barely visible whereas the same third onset is clearly seen in the 30-dB record shown on Fig. 20a. Thus, in this case, the 30-dB setting shows all the useful information more clearly than does the 60-dB record. This is an interesting example which shows that too much dynamic range can be detrimental.

Figure 23 introduces the linear scale by showing the same data with both a logarithmic and a linear frequency axis. As a general rule, those who do analysis usually desire to have a logarithmic frequency axis on HF sounder data because it greatly simplifies many calculations. The axis can be used in a more general way when it is logarithmic because, in a

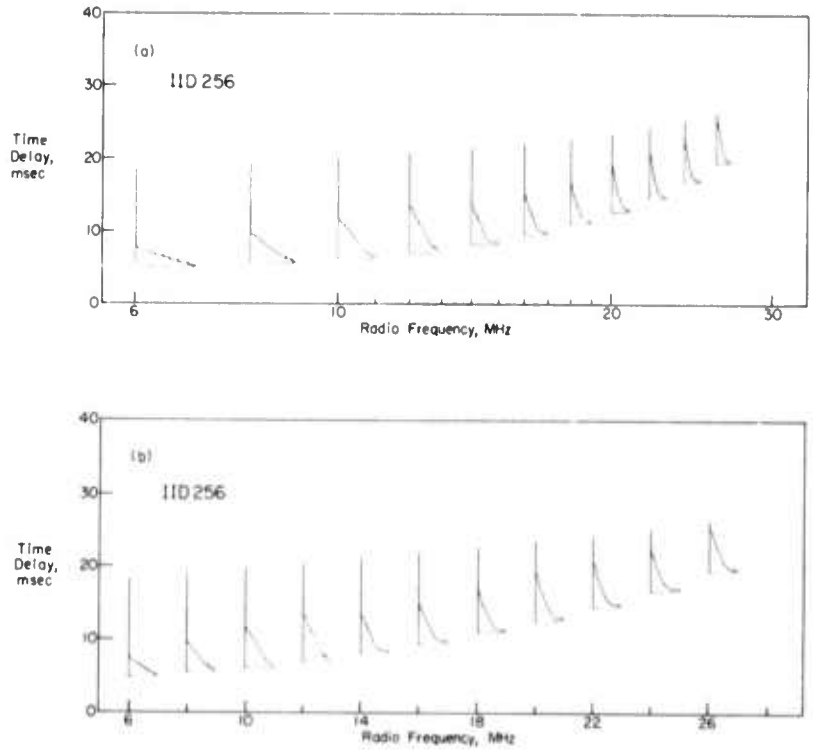

Fig. 23. COMPARISON OF BACKSCATTER OBTAINED WITH THE AMBIENT MODEL DISPLAYED WITH LOGARITHMIC AND LINEAR FREQUENCY SCALES. (a) With a logarithmic scale and (b) with a linear scale.

sense, it operates as one of the axes of a slide rule. For example, if we calculate the shape of sweep frequency backscatter for a certain ionospheric model with a critical frequency of 10 MHz, then that backscatter shape is identically the same as would be calculated with the same ionosphere if all electron densities were cut to half provided that all radio frequencies on the backscatter record are cut by $1/\sqrt{2}$. The frequency scaling can be done with a simple horizontal shift, provided that the frequency scale is logarithmic. This scaling works because we neglect the geomagnetic field so that the index of refraction is simply $\sqrt{1 - 80.6N/F^2}$, and thus the 2's cancel.

Those whose primary occupation is the gathering of sounder data tend to favor the use of a linear scale because it is much easier to construct equipment that will produce records with a linear scale. As a consequence, most experimental backscatter data have a linear frequency scale. This is

unfortunate for analysis because the shape of backscatter depends markedly on whether the frequency axis is linear or logarithmic. If the electron density everywhere is cut in half and we calculate backscatter with a linear frequency scale, then not only do the frequencies change but also the overall shape of the backscatter echo will change. It is not possible to use the sliding scale concept to eliminate the added complexity.

In order to serve these two communities of users, the backscatter simulation program plots synthetic backscatter twice, once with the linear scale and once with the logarithmic scale. A few of the linear examples are shown here to illustrate the changed appearance. On Fig. 23b, with the linear axis, it is seen that the peak abscissa displacement of each fixed frequency record is the same regardless of frequency, because now every single megahertz spans the same distance on the abscissa. In subjective appearance this is an advantage, but there is no actual practical benefit due to this new equality of amplitudes because the approximate backscatter simulation program does not calculate absolute amplitude in the first place. A normalization has already taken place before the program chooses whether to use a linear or logarithmic scale.

Figure 24 shows the original backscatter set from Fig. 8 replotted with linear frequency axes. The layout is identical to that of Fig. 8, but no new information is added. Notice the changed appearance of the backscatter with the linear axis.

D. Reflectrix Drawings for Different Ionospheric Models

As was stated previously, the ray drawings and backscatter drawings are useful, but it is sometimes difficult to understand propagation phenomena simply from examining these particular data displays. Another kind of data display that often lends additional insight is called the reflectrix. This construction was introduced by Lejay and Lepechinsky (Ref. 11), who coined the name for it. In fact, the reflectrix has been defined for use only with a symmetric ionosphere model such as has been used here for the ambient ionosphere and for the concentric anomalies. With the local or tilted anomalies, the reflectrix must be redefined.

Figure 25 serves to define the reflectrix, provided the electron density model is concentric with the earth. When the ionosphere contains

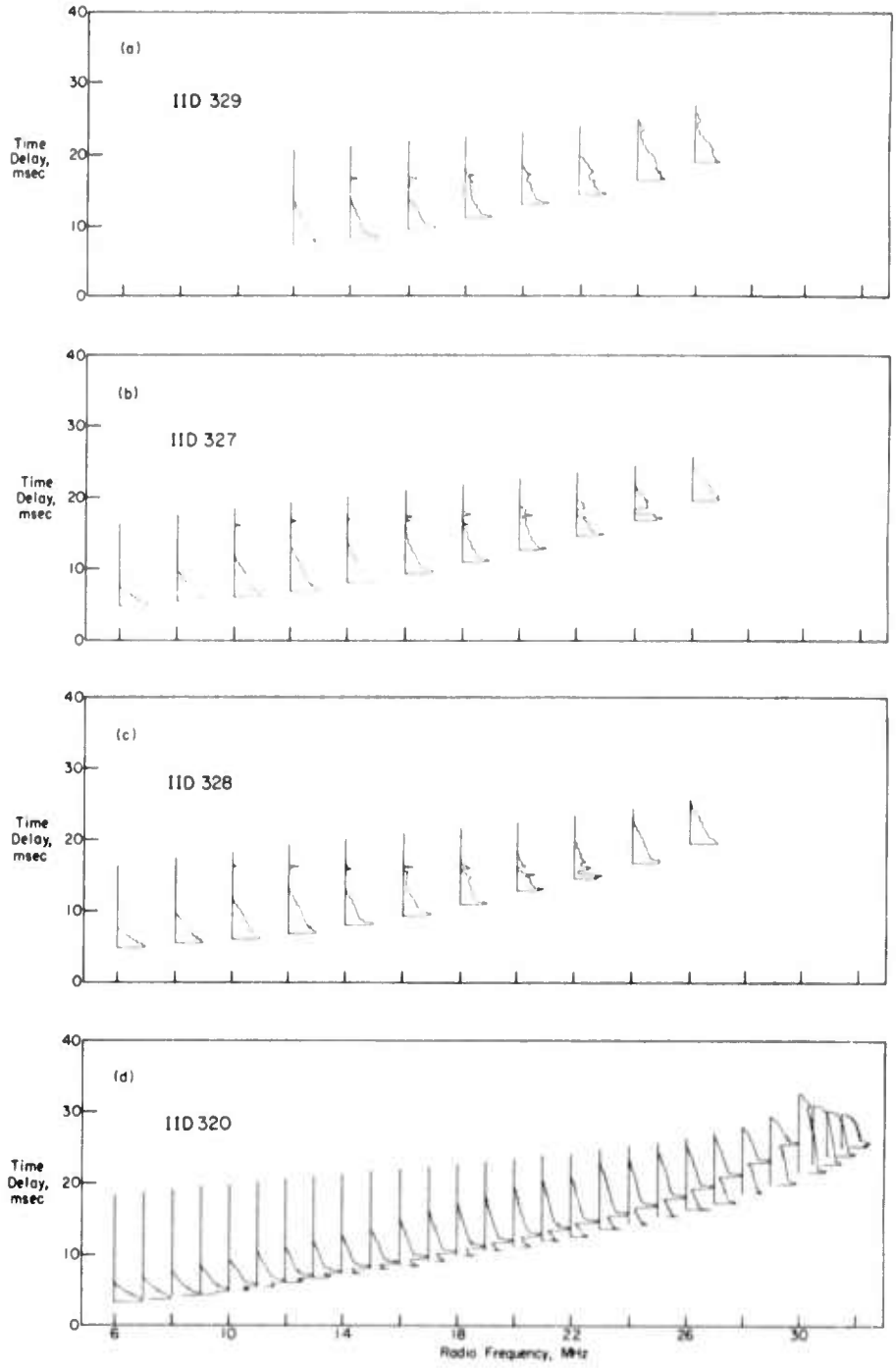

Fig. 24. BACKSCATTER WITH THE ORIGINAL SET OF ANOMALIES DISPLAYED WITH A LINEAR FREQUENCY SCALE. (a) With a local anomaly; (b) with the outward tilt; (c) with the inward tilt; and (d) with the concentric anomaly.

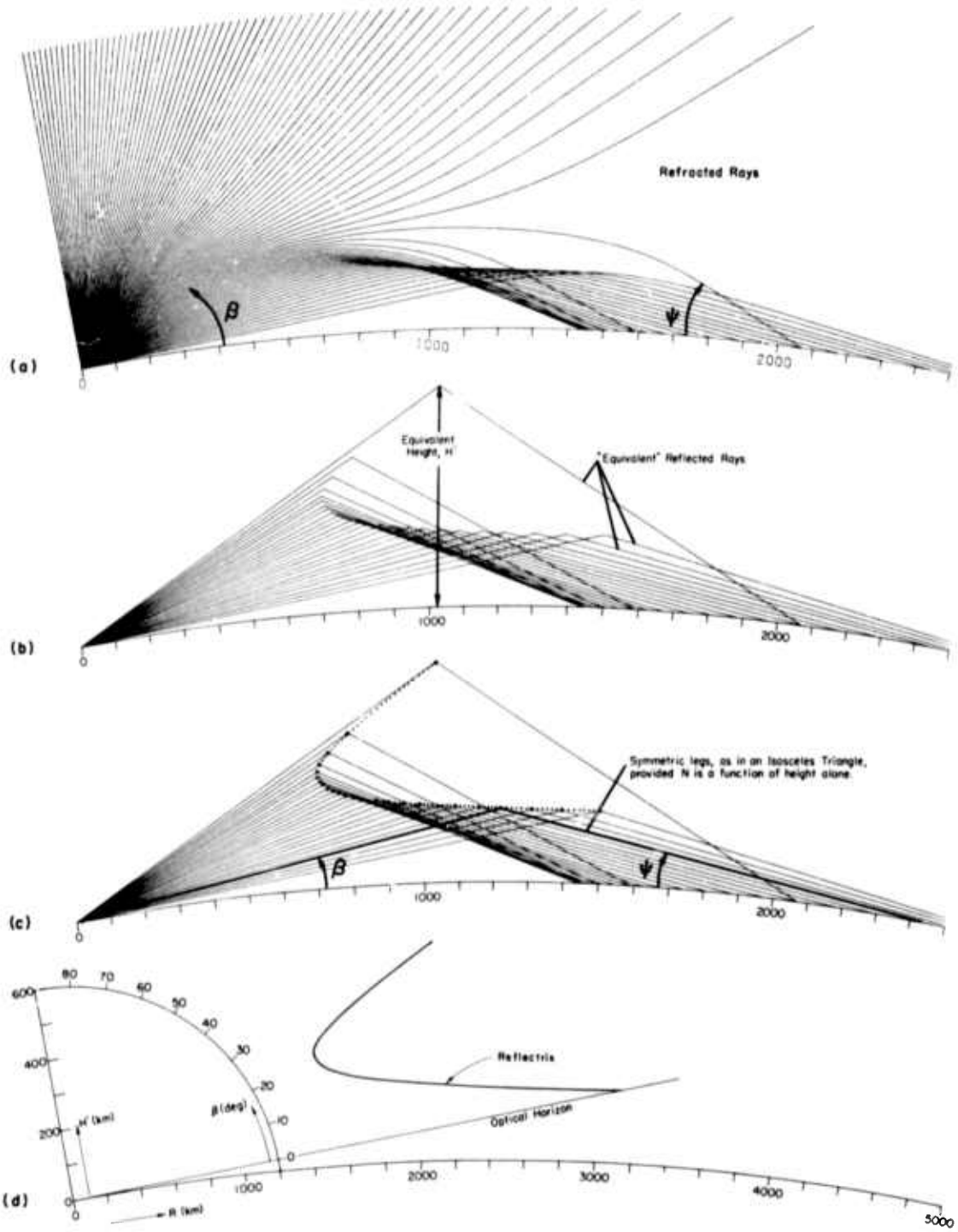

Fig. 25. DEVELOPMENT OF THE REFLECTRIX.

nonvertical gradients (tilts), there is no conventional definition and the author chooses to use the following: "Range" is the total range of the ray, and "equivalent height" is the height of the intersection of the two straight lines which are extensions of the ray at the two points where it encounters the earth. In this case, the takeoff angle axis is necessarily meaningless. For the concentric ionosphere, it was possible to have all three axes because they are redundant; that is, in a symmetric ionosphere, if one knows two of the three parameters R, H', β, then one can calculate the third without further information. In a tilted ionosphere, this is no longer true; as a consequence, one can no longer use all three axes simultaneously. This is why the definition of the reflectrix has been restricted to concentric ionospheres. In tilted ionospheres one could choose to preserve β and R, or H' and β, or H' and R. We have chosen the latter alternative here, but the reader is cautioned that this is not a universally accepted definition.

Figure 26 shows (a) a reflectrix as it comes from the automatic plotter and (b) a version that has been cleaned up by a draftsman. During the automatic plotting, we place a small x at the location of each rayset and then draw a line from the center of that x to the center of the next x which is located by the next rayset in a deck of cards. The line is drawn only when the two successive raysets have the same radio frequency. The line that joins two raysets is straight; therefore it is seen in the upper-ray regions where the rays are sparse that the curve is no longer apparently smooth but is composed of visibly separate straight-line segments. Of course, this is an artifice that can be eliminated by computing more rays in the upper ray region.

The automatically drawn plots are often useful because one can obtain a measure of signal strength by observing the closeness of spacing of the individual x's. In the drafting process, we eliminate the x's and substitute a smooth curve, which is easier to read, but it lacks an indication of the takeoff angle spacing of the rays from which the reflectrix was constructed. Because this section of the report is intended primarily for raytracing specialists, the reflectrixes will be presented here directly as they were plotted without any redrafting, except for the addition of a few labels where they seem advisable.

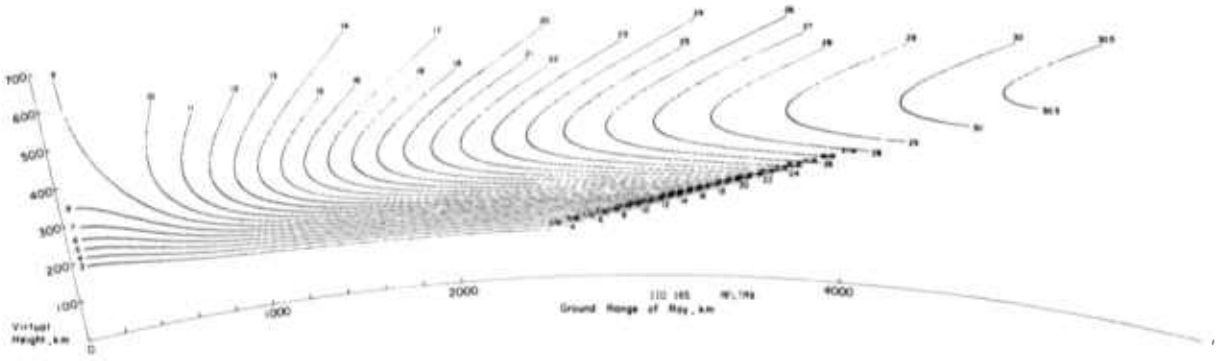

a. The reflectrixes as automatically plotted

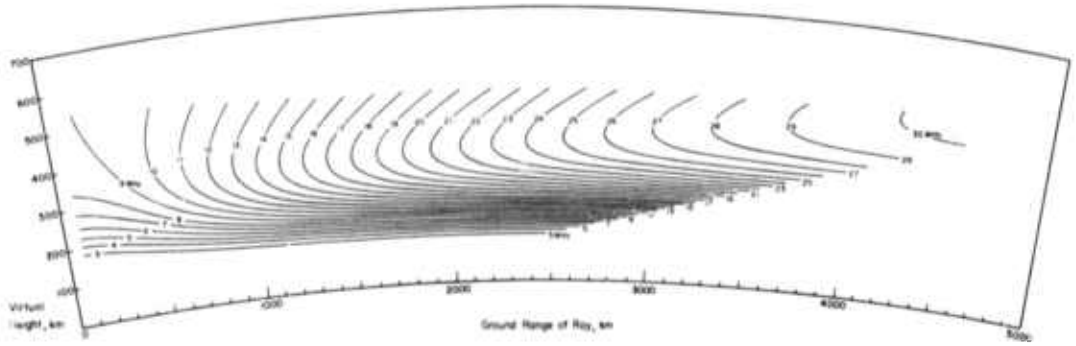

b. The same reflectrixes drawn by a draftsman

Fig. 26. REFLECTRIX SHAPES IN THE AMBIENT IONOSPHERE.

Both reflectrixes from Fig. 26 were calculated for the ambient model at each megahertz. In the tilted ionospheres, it was our practice to compute only the even megahertz rays as an economy measure.

Figure 27 shows the reflectrixes in the local, outward tilt and inward tilted anomalies. The rays for frequencies of 10 MHz and below were not calculated in the local anomaly because it could be seen in the ambient ionosphere that such rays would not have reached the altitude of the anomaly and thus would not have been affected by it. From the comparison of parts (a), (b), and (c) of Fig. 27 one can clearly see how the range and time delay of the anomaly disturbance exhibit a frequency dependence that is markedly influenced by the shape of the anomaly. With a local anomaly, part (a), the disturbances in the ray pattern are located almost directly above 2400 km. With the outward tilt in part (b) of the

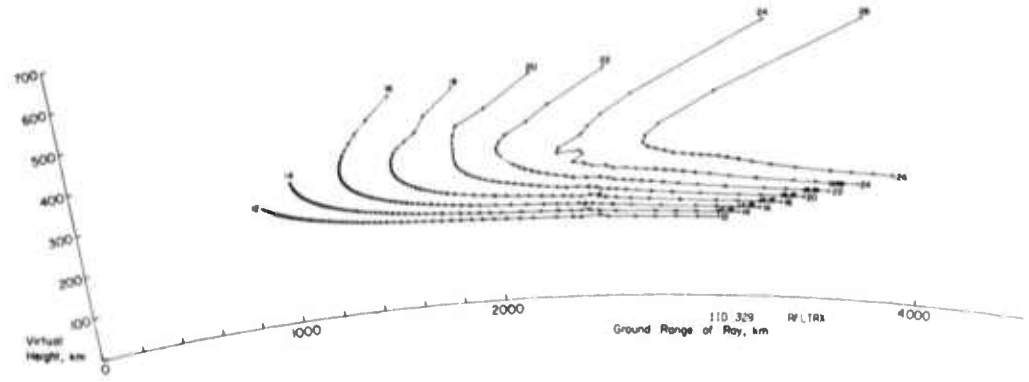

a. With the local anomaly

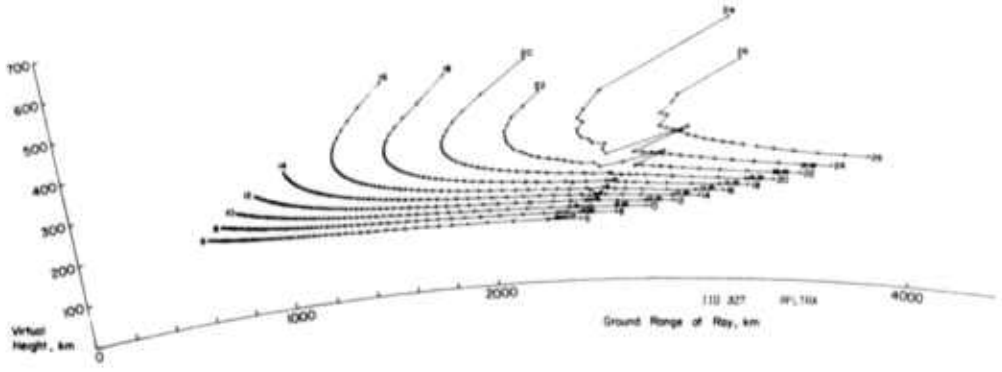

b. With the outward tilt

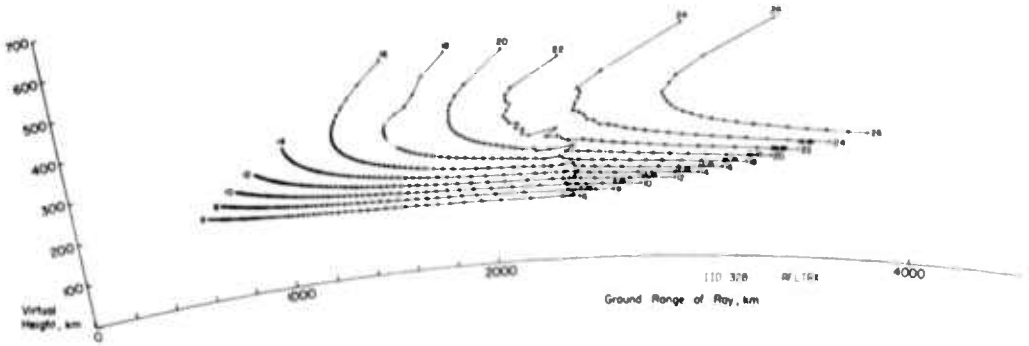

c. With the inward tilt

Fig. 27. REFLECTRIXES IN THE LOCALIZED ANOMALIES.

figure, it is readily apparent that the effect moves to a greater range at a greater time delay with an increase in frequency while the opposite trend is shown with the inward tilt on part (c).

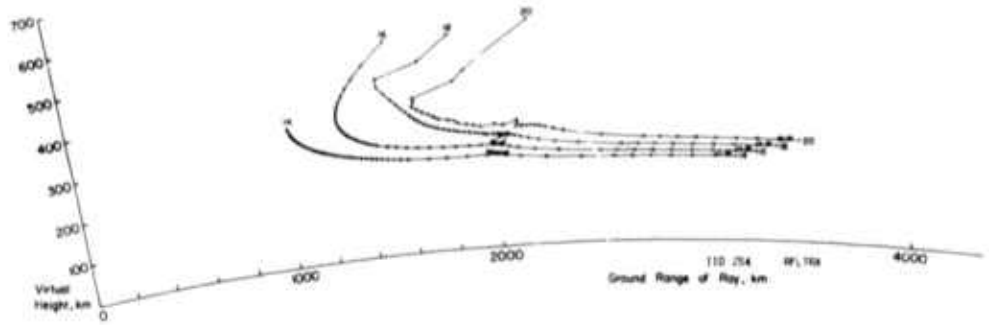

a. With the exaggerated local anomaly

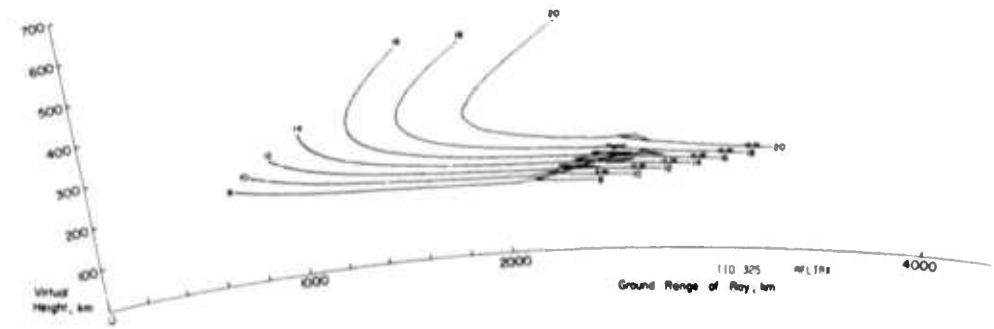

b. With the exaggerated outward tilt

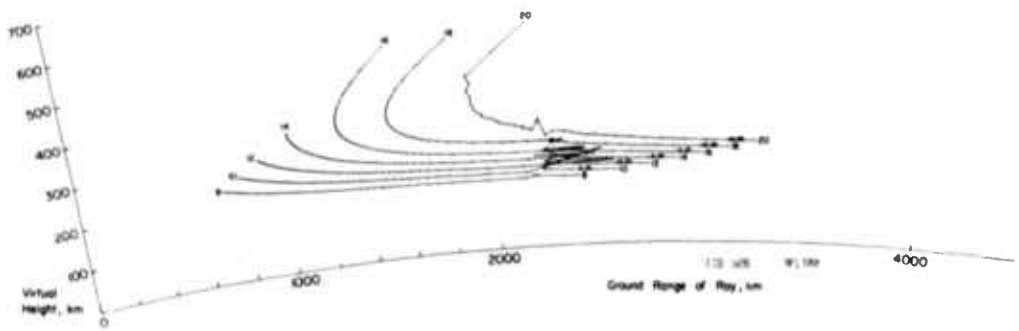

c. With the exaggerated inward tilt

Fig. 28. REFLECTRIXES IN THE EXAGGERATED ANOMALIES.

Figure 28 shows the reflectrix calculations for the exaggerated versions of the local and tilted anomalies. It is probable that much of the fine structure on these curves is due to some form of computation error. In particular, the erratic behavior of the rays of the skip distance at a few selected frequencies is probably a manifestation of some form of error that occurs when the rays pass through the anomaly near their apogee.

Notice, for example, the 20-MHz rays in Fig. 28a and 28c. It seems (on intuitive grounds, at least) that the disturbance of the ray pattern should be less random than it appears in these examples. The computation of a ray as it passes through an anomaly is somewhat difficult because the process is necessarily one of sampling the electron density and its gradient at a finite number of locations along the raypath. The ray structure is influenced by the way in which the samples are selected and it appears that we have not found an optimum solution here. The errors that arise in the program are accentuated in the exaggerated disturbances, which were, in fact, constructed primarily to test the severity of the electron disturbances that could be accommodated by the raytracing program.

Figure 29 shows reflectrix structures in the four concentric models. Since these lack any horizontal gradient, the original reflectrix definition of Fig. 25 is fully applicable and the takeoff angle axis has validity on this figure.

The effect of a concentric anomaly is a small-scale version of the effect of a regular ionospheric layer. To see what happens when an E layer is added underneath an F layer, the reader can refer to Ref. 12 where the author has shown a variety of reflectrix shapes. Ideally, the curve which characterizes one frequency should not cross any other curve which applies to some other frequency. We see in Ref. 12 that the presence of a two-layer structure can cause just such a crossing to occur. Thus, this undesirable effect occurs in a circumstance that is very common. Many other reflectrix plots (not shown here) were almost unreadable because of the large number of crossings that made it difficult to follow the pattern of the lines.

E. A Modified Form of the Reflectrix

Reference to the reflectrix explanation of Fig. 25 (or to the more detailed description given in Ref. 12) will serve to show that the distance from the origin to a point on the reflectrix should provide a measure proportional to the group delay of the ray. This is because the theorem of Breit and Tuve (Ref. 13) states that the group delay along a ray is equal to the delay at the speed of light along the equivalent straight-line ray, at least in a flat earth-flat ionosphere situation.

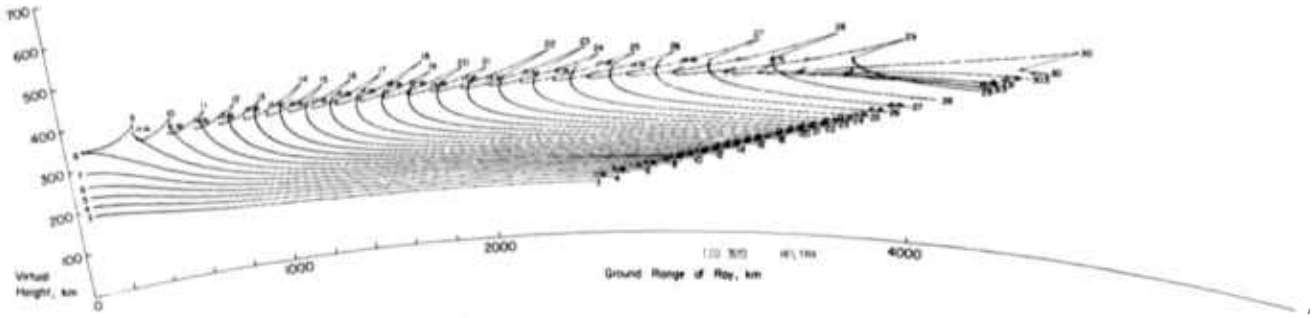

a. With the full cycle sinusoid based above 250 km

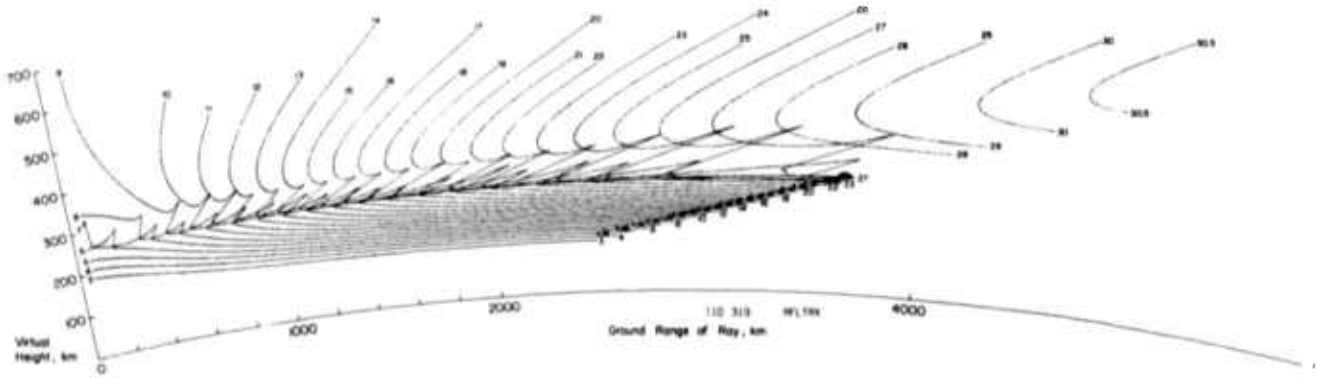

b. With the full cycle sinusoid based above 200 km

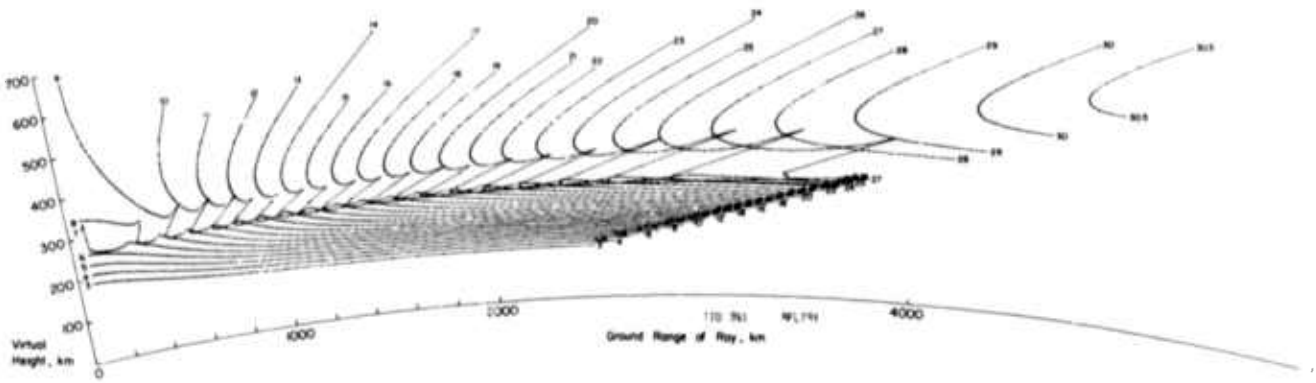

c. Positive half cycle of sinusoid, electrons added above 210 km

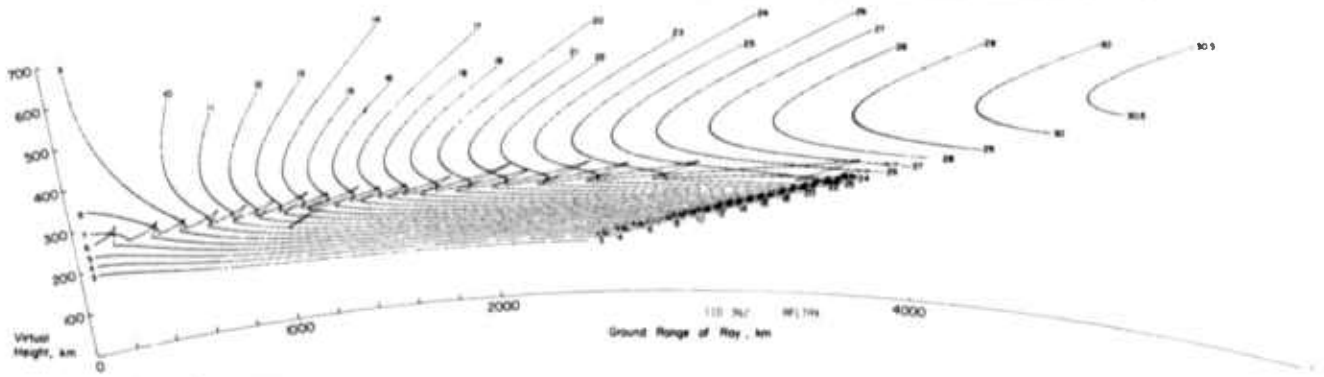

d. Negative half cycle of sinusoid, electrons deleted above 200 km

Fig. 29. REFLECTRIXES IN THE CONCENTRIC ANOMALIES

This is approximately true in a curved earth-curved ionosphere geometry, but there is a degree of error that is worse at longer distances.

When interest is centered upon ground backscatter, then one of the most interesting ray parameters is the range vs group delay. The takeoff angle has a comparatively minor significance, and an approximate measure of takeoff angle would be sufficient. In the reflectrix, the takeoff angle information is exact, but the time delay information is approximate. We would like to have exact time delay information and approximate takeoff angle information. This can be accomplished by a slight modification of the reflectrix for which the author has coined the term, "timetrix." In the timetrix construction, the distance of a point from the origin of the plot is fixed by the distance that light would travel in half the transit time of the ray. For this, the drawing scale of Fig. 25, part (a), (b), or (c) is used. Thus, when the drawing scale is doubled as it is in the transition to part (d) of Fig. 25, then the distance of a reflectrix point from the origin is equal to the total distance that light would travel during the ray transit time, that is, to the group path of the ray. As in the reflectrix, the range of a ray is used as the second parameter fixing the location of a point. The equivalent height, H', is now slightly different from that which was defined in Fig. 25, the difference being a direct measure of the error in the theorem of Breit and Tuve when it is applied to curved earth-curved ionosphere geometry. Similarly, there is a slight error in the takeoff angle measure using the simple protractor construction of Fig. 25d. This error seldom exceeds 3°, however, and it is this severe only at the longer ranges.

Figure 30 shows the timetrix for the ambient ionosphere and should be compared with Fig. 26, which shows the identical data in reflectrix construction. On Fig. 30, at any frequency, the initial backscatter will be received via that ray that is nearest the origin; this can be located by striking an arc centered on the origin that is tangent to the appropriate curve. Analysis of backscatter can be aided by considering the intersection of an expanding circle, centered on the origin, with one of these timetrix curves. One can thus follow the progress of the energy by all modes as a function of time. In Ref. 12, this process of reasoning was fully explained but only in reference to a reflectrix, where the process

is approximate. The interested reader may refer to that explanation which, when applied to the timetrix, is exact.

The comparison of Fig. 30 with Fig. 26b can be used to establish the amount of error in the Breit and Tuve theorem in the following manner: Select any point and locate it on both the timetrix and the reflectrix. For this process, it is easiest to use a high-frequency upper-ray, for there the error is greatest. On the reflectrix, measure the distance of the point from the origin. The theorem of Breit and Tuve would tell us that this is the time delay of the ray. The same measurement on the timetrix yields the actual time delay and the difference of the two measurements is then the error in the theorem. It can thus be seen that the theorem is quite good for most purposes, particularly when one considers how little is known about the ionospheric structure which is used in the original generation of the reflectrix or timetrix.

Figure 31 shows timetrix structures for the local and tilted anomalies, and Fig. 32 shows these structures for the concentric anomalies with a figure layout identical to that used in the corresponding reflectrix displays of Figs. 27 and 29. At first glance, it may seem that these two sets of figures are identical, but closer examination will show that there are some easily perceptible differences between the timetrix and reflectrix presentations. This is particularly true in the details of the disturbance of the ray structure by the anomalies. The figures are shown here primarily as an aid to specialists who may otherwise have wondered how much error is introduced in the reflectrix construction as a means of

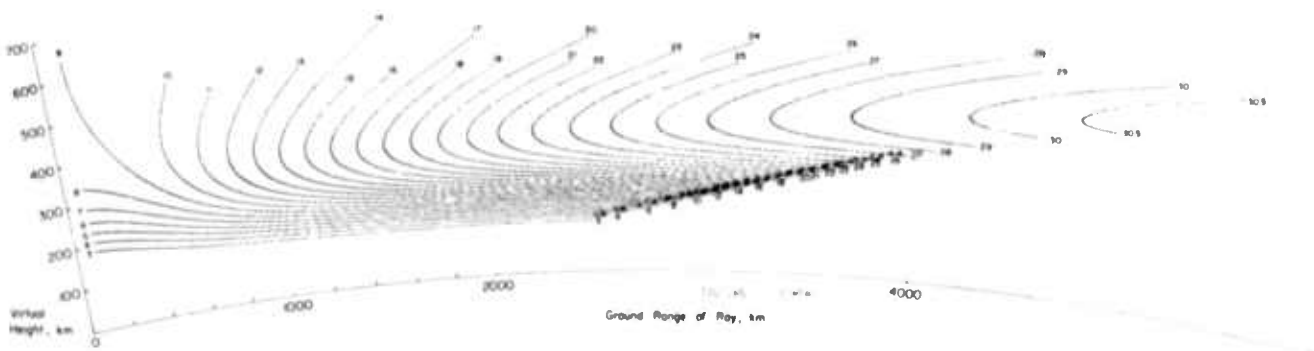

Fig. 30. THE TIMETRIX STRUCTURE IN THE AMBIENT IONOSPHERIC MODEL.

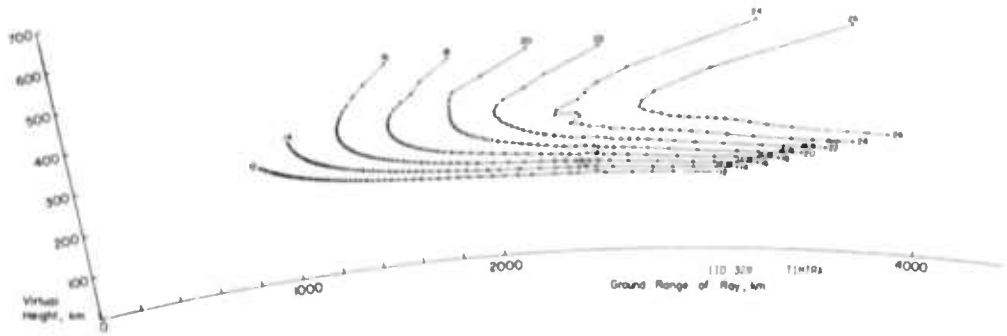

a. With the local anomaly

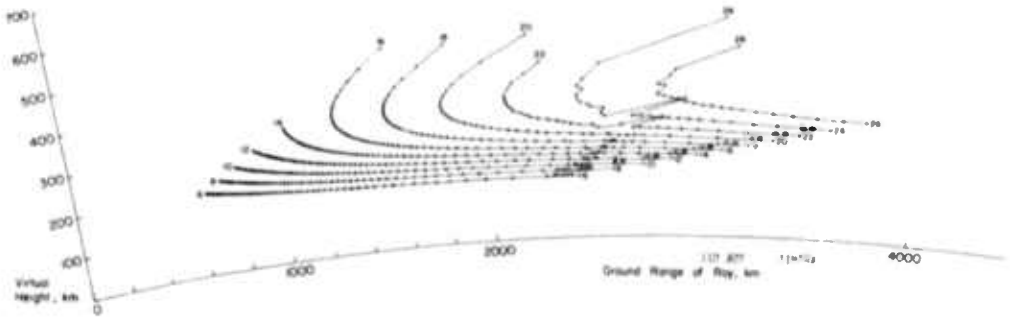

b. With the outward tilt

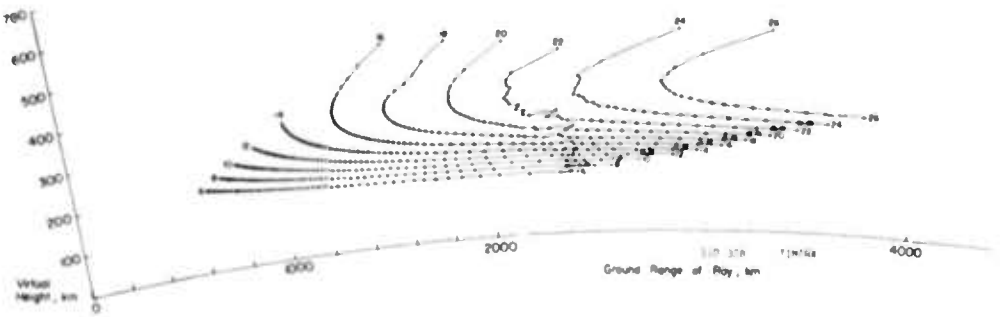

c. With the inward tilt

Fig. 31. TIMETRIX STRUCTURES IN THE LOCAL AND TILTED ANOMALIES.

measuring time delay through the Breit and Tuve theorem. It appears reasonable to conclude that the reflectrix will serve most practical purposes quite well, but that, for some specialized applications, the timetrix (or one of several other possible modifications) might be superior.

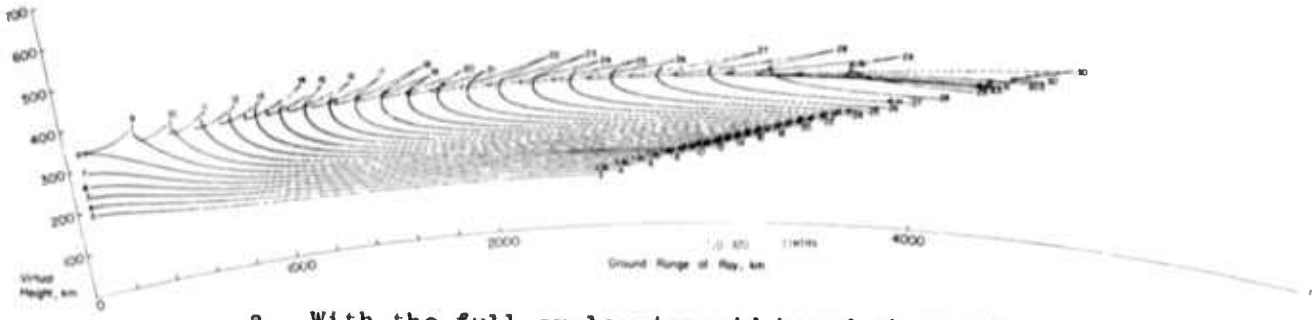

a. With the full cycle sinusoid based above 250 km

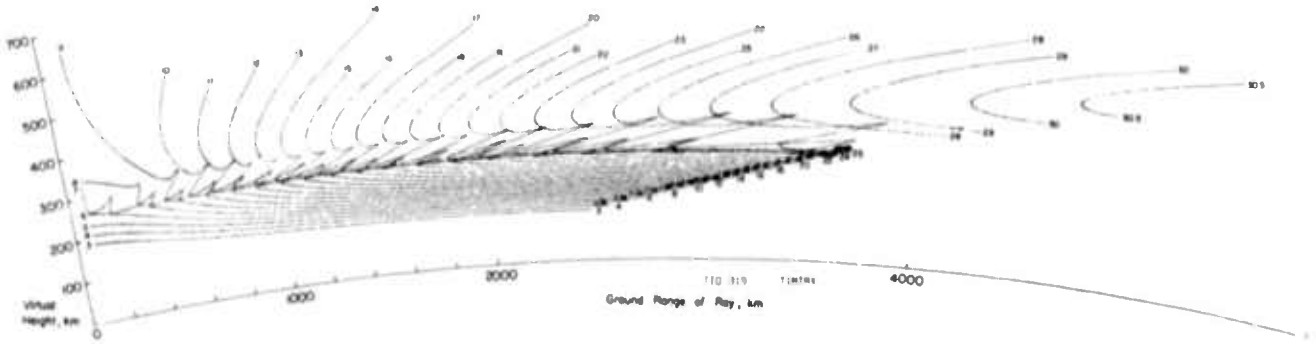

b. With the full cycle sinusoid based above 200 km

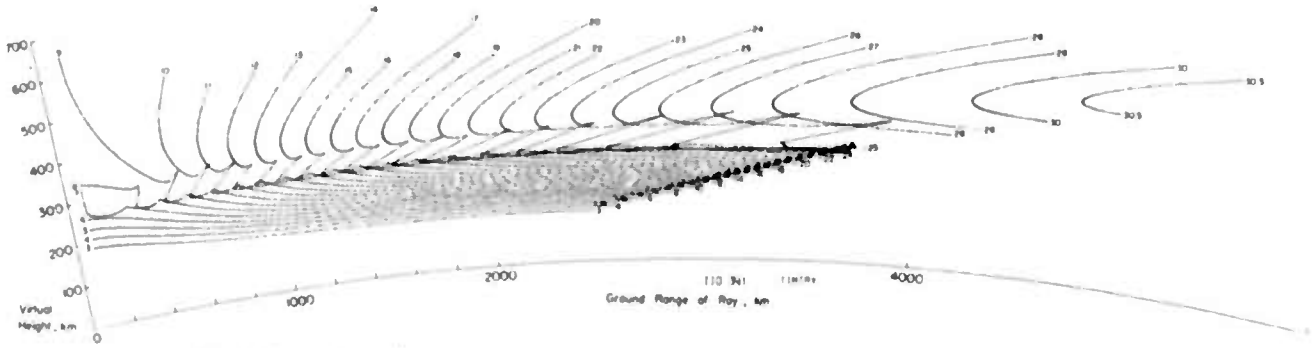

c. Positive half cycle of sinusoid, electrons added above 210 km

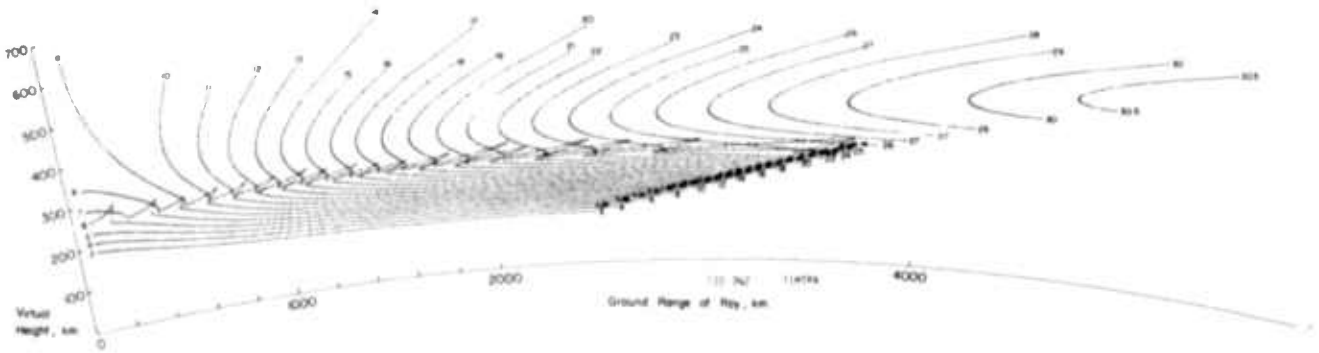

d. Negative half cycle of sinusoid, electrons deleted above 200 km

Fig. 32. TIMETRIX STRUCTURES IN THE CONCENTRIC ANOMALIES.

F. The "Param Plot," A Graphical Construction Designed To Show Relationships among Rays

It was noted in the preceding section that the reflectrix (or time-trix) structures often cross one another in a way that often makes it impossible for the viewer to determine the pattern of the lines. Nevertheless, the constructions do serve a useful purpose because they show the relationship of raypath range, group delay, takeoff angle, frequency, and virtual height in a concentric ionosphere. The usefulness of the construction lies in the large number of these parameters that are included on a single graphical presentation.

Two years ago, the author set out with the intention of finding the optimum graphical presentation of a family of rays, which should ideally show the relationship among a variety of parameters by means of curves that do not cross one another as do the reflectrixes. Among the desirable ray parameters are the following:

radio frequency

range, measured along the ground

group delay

phase delay, or number of wavelengths along a ray

takeoff angle of the ray

arrival angle (may differ from takeoff angle only in a tilted ionosphere)

apogee height

virtual height, computed from takeoff and arrival angle

virtual height, computed from group delay

absorption along the path

total Faraday turns along the path.

If the geomagnetic field is included in the calculations, then of course one would like to display all of the above parameters for both the ordinary and extraordinary rays. Obviously, the list contains far too many parameters to be presented on a single chart. As will be seen, the readability of the chart decreases rapidly as the number of parameters increases.

In an effort to decrease the magnitude of the problem to manageable dimensions, interest was centered on only a few of the ray parameters:

(1) We neglect the magnetic field for this first effort.

(2) We choose to display range, group delay, and radio frequency because these are primary measurable quantities.

(3) We choose takeoff angle (equivalent to arrival angle in a non-tilted ionosphere) because power density is a function of the rate of change of other parameters with respect to takeoff angle.

(4) As a fifth parameter, we have chosen apogee height, that is, the height of the top of any ray. This serves partly to tell at a glance the region of the ionosphere that exerts dominant control over any given ray since most of the bending occurs at apogee. Perhaps most important, however, is the fact that it was found by experimentation that the apogee could be used as one of two axes in a plot that had very desirable characteristics.

(5) Since group delay is almost proportional to range, lines of constant group delay would look very much like lines of constant range. Furthermore, comparisons between the time delays of two rays is generally carried out at a fixed range. Consequently, we have found it desirable to subtract from each time delay the time it would require for the speed of light to traverse the surface of the earth underneath the ray. We then deal in "excess group delay," T_e, which is defined by the relation $T_e = T_g - R/c$ where T_g is group delay, R is ground range, and c is the speed of light.

Using the five parameters, we plotted a sample set of data in many possible ways, using each possible pair of parameters as abscissa and ordinate. The remaining three parameters were used to define families of curves plotted in the field. Thus there were ten possible plots considered; of these, the best was the plot in which ground range served as the abscissa and apogee height served as the ordinate. On this display, if the ionosphere is nontilted, none of the curves within a family ever cross one another; therefore, it is not possible to make an ambiguous graph. Furthermore, the three families of parametric curves, defined by takeoff angle, radio frequency, and excess time delay, all tend to cross one another at roughly 60° angles, which is optimum for least confusion. Finally, the overall shape of such a plot is roughly such that it fills most of a rectangular area and thus the information can be compactly displayed on a page. This latter criterion is important and

failure to meet it was one of the most serious shortcomings of an otherwise desirable display in which range and takeoff angle served as the two axes.

Figure 33 shows a param plot, which has been drawn with rays calculated through the ambient ionospheric model. A single-color param plot is extremely difficult to read, partly because the computer-drawn curves have a small scale jitter that serves to break up the flow of the line pattern. This makes it difficult for the eye to follow the progress of a family of lines in the presence of other similar families. It was possible to read the single-color param plot in the ambient ionosphere, but even the addition of a simple E layer to the model introduced enough additional complexity to make the single-color version virtually useless. This is probably the main disadvantage of the param plot representation, since multicolor reproduction like that of Fig. 33 is expensive in these reports and virtually impossible to incorporate in other media. For example, technical journals rarely reproduce color, and no office copying machines will preserve the color of a picture.

To overcome the need for color, the remaining param plots in this report will be presented with only the curves that are parametric in frequency. This will serve our purpose here, but does not solve the basic problem. It would be very useful if a practical parameter plotting format could be devised, for then the output of a raytracing program could be much more readily preserved and communicated to other workers. Figure 33 is included here primarily to show what we are striving for, in the hope that other workers may become interested in this display problem and attempt to improve upon it.

In a sense, a param plot is a map of the characteristics of a particular ionospheric profile as it affects radio waves. So long as all wave sensors are on the earth's surface, the param plot presents most of the useful information that can be obtained. For example, the radio signal strength is a direct and fairly simple function of the derivative $d\beta/dR$, which can be obtained directly from the param plot. Although not presented here, phase path difference information is inherently included in the form of excess group delay. Thus, one could postulate a change in critical frequency and thereby compute the induced frequency shift in some

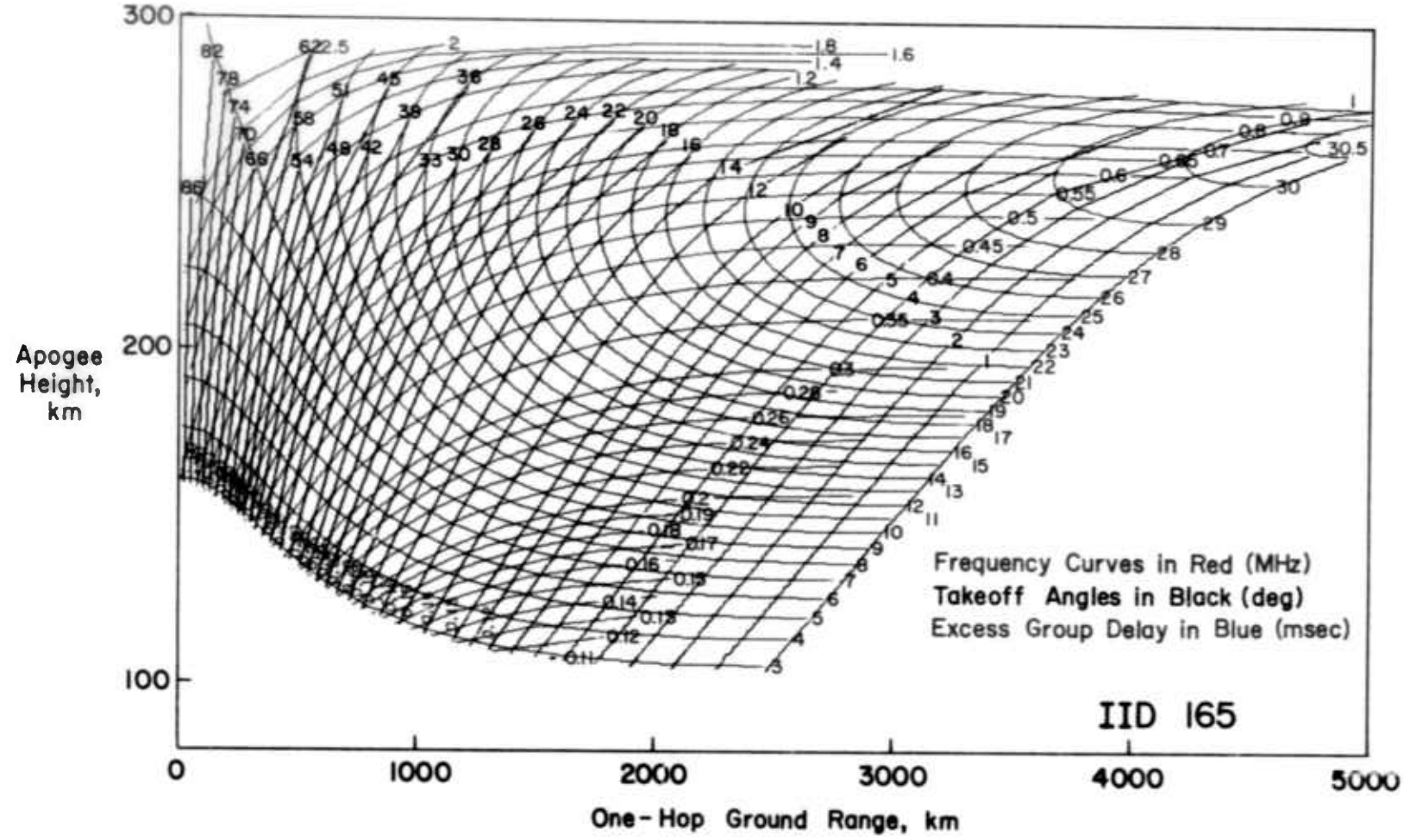

Fig. 33. THREE COLOR PARAM PLOT IN THE AMBIENT IONOSPHERIC MODEL.

hypothetical carrier signal. Possibly the only serious deficiency is the lack of absorption or Faraday rotation information on the chart, but it is clearly impractical to try to add other families of curves to Fig. 33. One might consider supplying additional transparent overlays providing additional information on the same abscissa and ordinate axes; this should work well. However, from a practical standpoint, it is even more objectionable than the use of color to require the availability of transparent overlays.

Figure 34a shows the frequency curves of a param plot generated from the rays computed in the outward and inward tilt models. These curves should be compared with the red curves on Fig. 33; it can be seen that there is indeed a disturbance with a tilt corresponding to the anomaly tilt. It is the author's impression that most of the small structural detail should be ignored because it is probably inserted by the imperfect ray calculation method that was used. However, a very important point can be made on this drawing which has not been evident in any of the previous data displays, and therein lies the value of the param plot.

The tilted vertical bars in the drawings enclose the region containing most of the rays that have their apogees within the disturbances. It is only possible to draw such a region on the plot because of the choice of axis labels, range, and height. If the ionosphere had contained no tilts whatsoever, then each ray apogee would be located at exactly half of the total range of the ray. With this idea as an approximation, the tilted vertical bars are drawn by plotting the height vs range of the inner and outer surfaces of the anomalies, allotting a factor of two to allow for the fact that the abscissa represents a total horizontal range rather than apogee range. Thus, it is not strictly true that the boundaries include all those rays and only those rays whose apogees lie in the anomalies because the rays are not symmetric in this ionosphere. (This follows because the ionosphere is not concentric with the earth.) Nevertheless, it can be seen that the primary effect of the anomalies is exerted only on those rays that fall within the boundaries shown on Fig. 34a and b.

It can be seen why this should happen if one applies the logic that was described in Chapter V during the discussion of the ray drawings

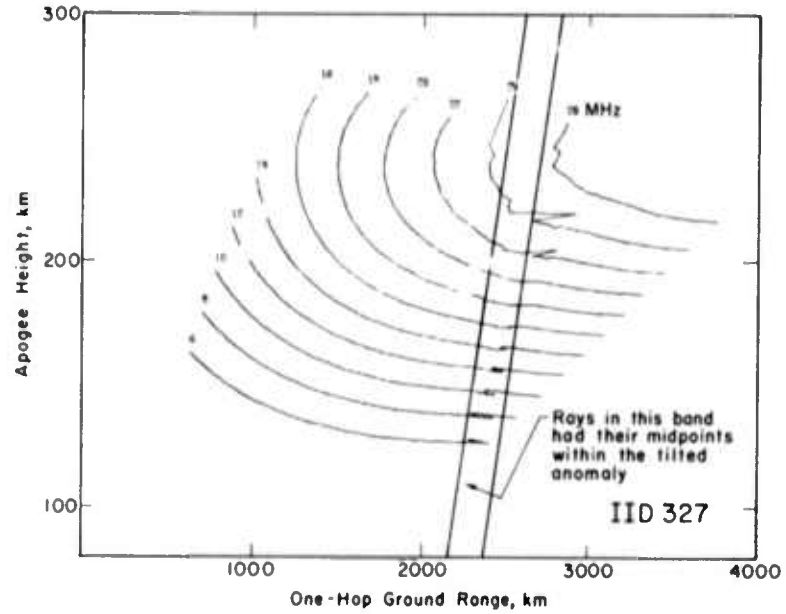

(a)

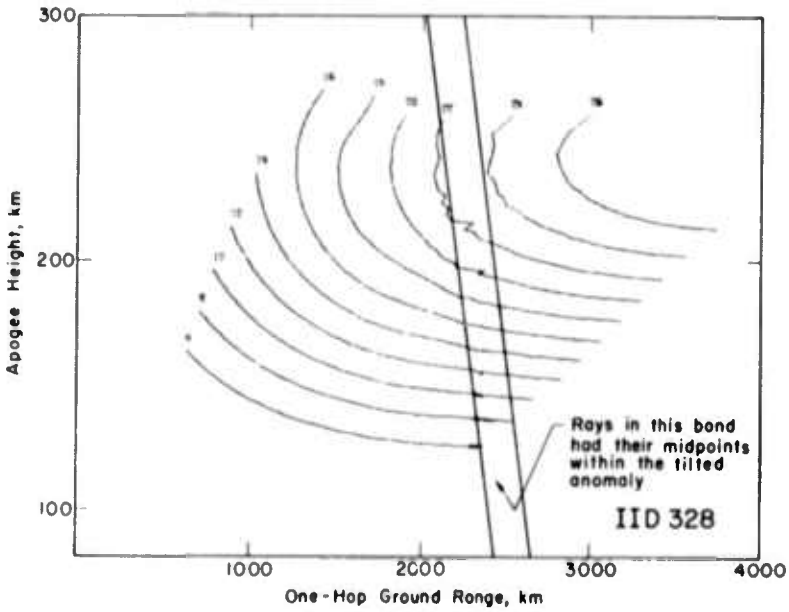

(b)

Fig. 34. PARTIAL PARAM PLOTS IN THE TILTED ANOMALY MODELS

through the outward and inward tilts. The effect is simple when one examines the disturbance of the lower rays only. Those rays that strike the anomaly on their upward transit acquire a shortened range and those rays that strike it on their downward passage acquire a lengthened range so that the meeting of the two families takes place near the rays with apogees in the disturbance. This simplicity of logic can be seen in the param plots if one examines the lower rays from 20 MHz downward. Each ray family appears comparatively unaffected except at the location where the apogees pass through the anomaly, where there is a noticeable discontinuity. However, notice on Fig. 34a that the 24- and 26-MHz effect is comparatively complicated since it occurs near the skip distance where the anomaly can change upper rays to lower and vice versa. The inward tilt causes this effect at 22 and 24 MHz.

Now it can clearly be seen why the height-range behavior of the anomaly affects the frequency-time behavior of the ground backscatter. The excess time delay changes from about .14 msec at 6 MHz to .45 msec at 24 MHz as we follow the progress of the anomaly effect upward through the rays on the param plots. (These curves have not been included here, but they were computed.) For the purpose of this discussion, we can assume that the range axis also represents the time axis since this change in excess delay is comparatively minor. The relation between height and frequency is almost linear as can be seen by examining the spacing between the various frequency curves at their intersection with the tilted anomaly. Thus, altitude is equivalent to frequency during the passage of the radio waves. Similarly, range is converted into time delay because the total distance exercises dominant control over the time delay. The ionosphere adds some effect, tending to increase time delay at higher frequencies, but it is a minor addition to the effect of the tilt. This is important in understanding the reason for the upward tilt bias in the backscatter streaks, however. Refer to Fig. 8 and notice that the local anomaly produces a streak that is tilted upward about 1°. The outward tilt adds a positive 2° increment and a negative tilt subtracts 2° from this 1° prevailing tilt. The prevailing tilt is attributable to the effect of the ionosphere. The additional 2°, plus or minus, is attributable to the tilt of the anomaly.

Thus, the param plots have permitted us to deduce the reason for the 1° bias in the tilts on Fig. 8.

Figure 35 shows param plots for the four concentric anomalies. Again, it is reasonably valid to assume that the range axis provides a measure of group delay since the excess delay curves add a comparatively minor perturbation to numbers computed by simply converting range values to time values. Figure 35a shows the frequency curves for the rays used to generate the backscatter of Fig. 8d. The concentric anomaly was located high enough in the ionosphere that there were no propagating rays with apogees in the ambient model above the anomaly. This explains why the backscatter from the high concentric anomaly was more simple than the backscatter from the lower concentric anomaly. Figure 35b shows the lower anomaly and now we see that there are a large number of rays with apogees above the anomaly. Most of the single frequency curves have three distinct minimum range points. (They similarly have three minimum time points.) Consequently, there should be three distinct enhancements in any single frequency backscatter calculation; indeed, this was the case in Fig. 20.

On Fig. 35b notice that the upper two noses on any single curve are never far apart in range. This is why the added enhancement in the backscatter never departed very much from the normal leading edge of the backscatter on Fig. 20a. However, notice that the comparison of Fig. 35a and b shows a systematic difference between the structure of the rays and the two ionospheres. The ambient leading edge of the backscatter is preserved on Fig. 35a in the form of rays that reach their minimum range at an altitude of roughly 230 km, well <u>below</u> the anomaly. However, on Fig. 35b, the reproduction of the ambient leading edge of the backscatter is attributable to rays that have their apogees at about 250 to 270 km well <u>above</u> the concentric anomaly, Presumably, an anomaly located at some intermediate altitude would cause a different effect. Thus it appears that a traveling anomaly moving vertically in the ionosphere should cause widespread disturbances throughout the body of any sweep frequency backscatter echo structure. It should be possible to gain a full understanding of the phenomena by using ray plots, param plots, and synthetic backscatter plots in conjunction with each other. We have not carried this study further, but it does appear to be an area in which more research is desirable.

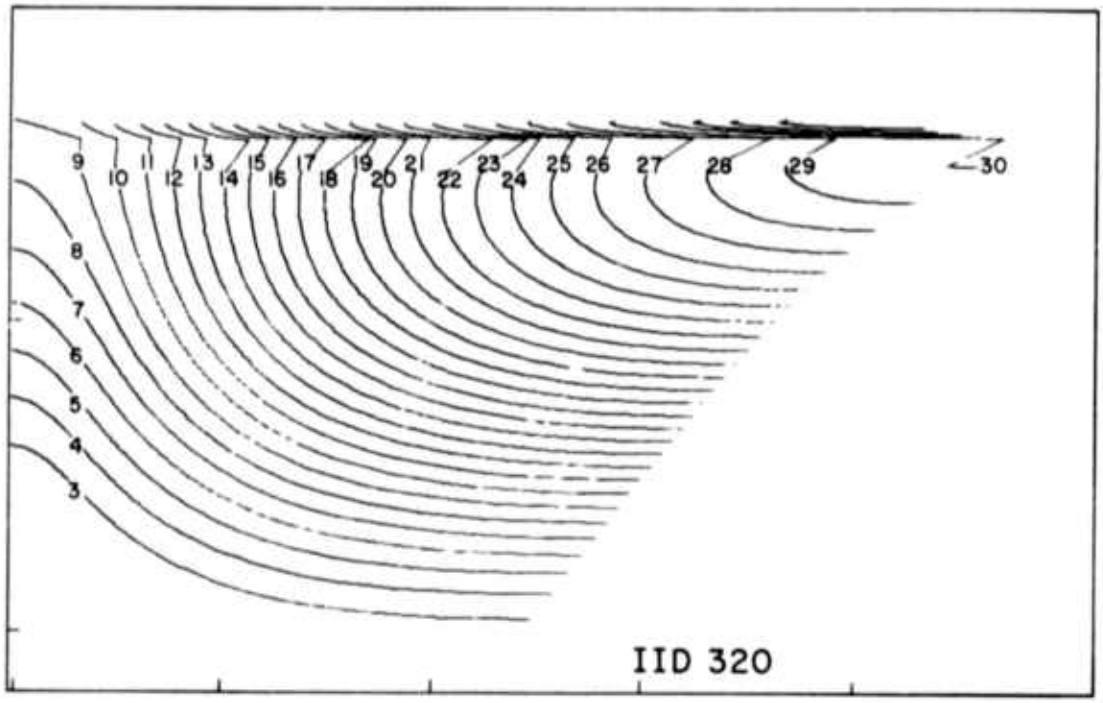

a. With the sinusoid above 250 km

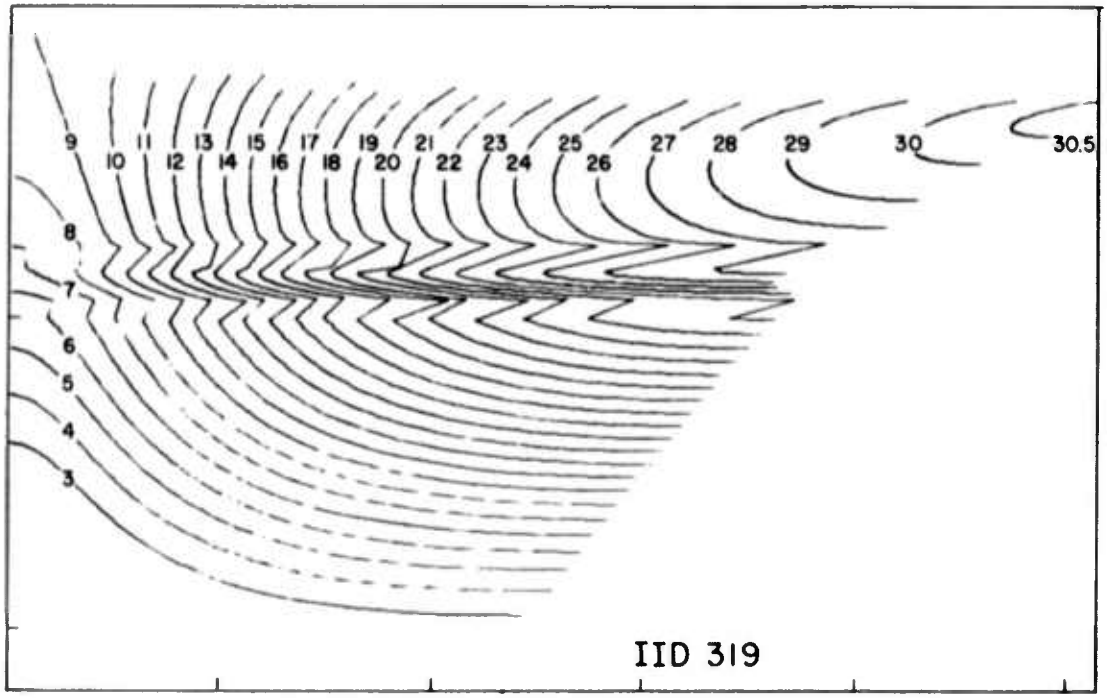

b. With the sinusoid above 200 km

Fig. 35. PARTIAL PARAM PLOTS IN THE CONCENTRIC ANOMALY MODELS.

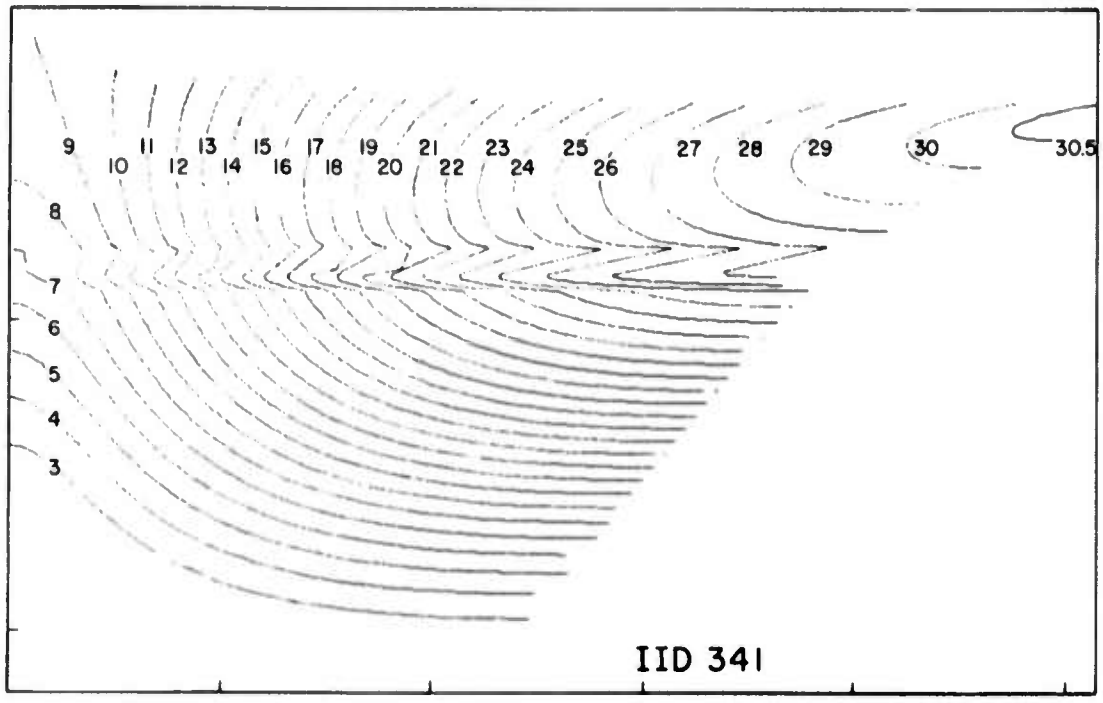

c. Positive half cycle of sinusoid, electrons added above 210 km

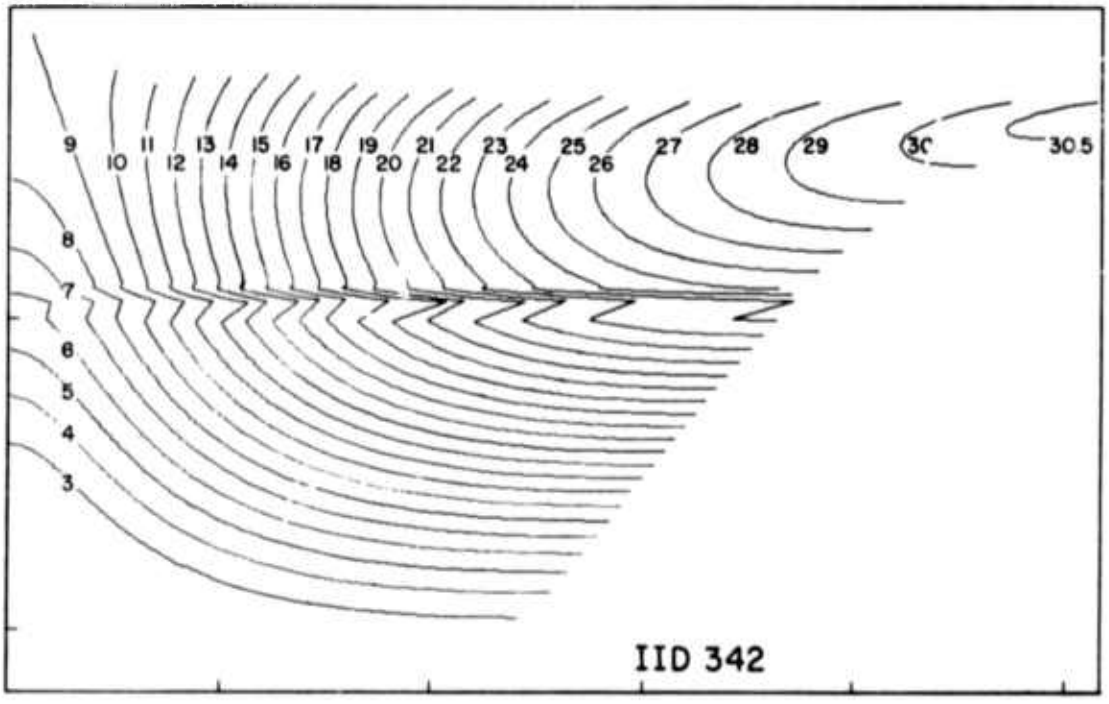

d. Negative half cycle of sinusoid, electrons deleted above 200 km

Fig. 35. CONTINUED.

Figure 35c and d show the effect of propagation in the partial concentric anomalies which are generated by separating the positive and negative half cycles of the sinusoid disturbance which was used to generate ionosphere IID 319. The reason for the structure of the backscatter can now be seen by applying logic similar to that discussed above. It does appear on the basis of this calculation that it would be possible to make a simple electron addition of such a nature that the third backscatter enhancement is suppressed, but it would require careful model structuring. Perhaps the lesson to be learned is that the appearance of two new backscatter enhancements, before and after the ambient leading edge, are indications of a single phenomenon similar to that shown in Fig. 35b, c, or d.

VII CONCLUSIONS

In displays of sweep frequency backscatter sounding data there are often streaks in the data which are nearly parallel to the frequency axis. Here it has been shown that these streaks may be attributed to the presence of localized irregularities in the ionosphere approximately midway between the sounder and the scattering ground. When striations are tilted (that is, when their time delay varies with frequency), the tilt may be attributed to a geometric tilt in the parent anomaly. This cause-effect relationship has been partially verified by an observation that the direction of tilt and the direction of motion of individual striations agree with the predictions of atmospheric gravity wave theory, at least for the six examples available. It was also found that the frequency interval spanned by a backscatter striation should indicate the height interval occupied by the anomaly.

Finally, it has been shown that horizontally disposed anomalies ("layerlets") in an otherwise smooth ionospheric layer give rise to new leading edges on the backscatter records. Other mechanisms can cause similar multiple leading edges; discrimination among the possible causes may be feasible but has not been demonstrated.

REFERENCES

1. T. A. Croft, Computation of HF ground backscatter amplitude, Radio Sci. 2 (New Series), 7, Jul 1967, pp. 739-746.

2. B. F. Fogle, private communication (see Acknowledgment), 1967.

3. R. D. Hunsucker and L. H. Tveten, Large traveling-ionospheric-disturbances observed at midlatitudes utilizing the high resolution h.f. backscatter technique, J. Atmos. Terr. Phys. 29, 8, 1967, pp. 909-916.

4. G. D. Thome, Incoherent scatter observations of traveling ionospheric disturbances, J. Geophys. Res. 69, 19, Oct 1964, pp. 4047-4049.

5. C. R. Gilliland, Sweep-frequency backscatter with calibrated amplitude, Rept. SEL-65-095 [TR No. 111, Contract Nonr-225(64)], Stanford Electronics Laboratories, Stanford, Calif., Oct 1965.

6. T. A. Croft, The synthesis of sweep-frequency ground backscatter by digital computer, Rept. SEL-65-002 [TR No. 84, Contract Nonr-225(64)], Stanford Electronics Laboratories, Stanford, Calif., Jan 1965.

7. P. O. Laitinen and G. W. Haydon, Analysis and prediction of sky-wave field intensities in the high frequency band, U. S. Signal Corps R. P. A. Tech. Rpt. 9, RPU-203, Fort Monmouth, N. J., Aug 1950.

8. D. C. Baker and J. A. Gledhill, An unusual travelling disturbance in the F-region of the ionosphere, J. Atmos. Terr. Phys. 27, 1965, pp. 1223-1227.

9. C. O. Hines, Internal atmospheric gravity waves at ionospheric heights, Can. J. of Phys. 38, 1960, pp. 1441-1481.

10. A. M. Peterson, The mechanism of F-layer propagated backscatter echoes, J. Geophys. Res. 56, 2, 1951, pp. 221-237.

11. P. Lejay and D. Lepechinsky, Field intensity at the receiver as a function of distance, Nature, 1950, pp. 306-307.

12. T. A. Croft, HF radio focusing caused by the electron distribution between ionospheric layers, J. Geophys. Res. 72, 9, 1967, pp. 2343-2355.

13. G. Breit and M. A. Tuve, A test of the existence of the conducting layer, Phys. Rev. 28, 1926, p. 554.

APPENDIX

FIG. 3. BACKSCATTER AT 2 MINUTE INTERVALS, ARRANGED TO SHOW MOTION BY PAGE FLIPPING.

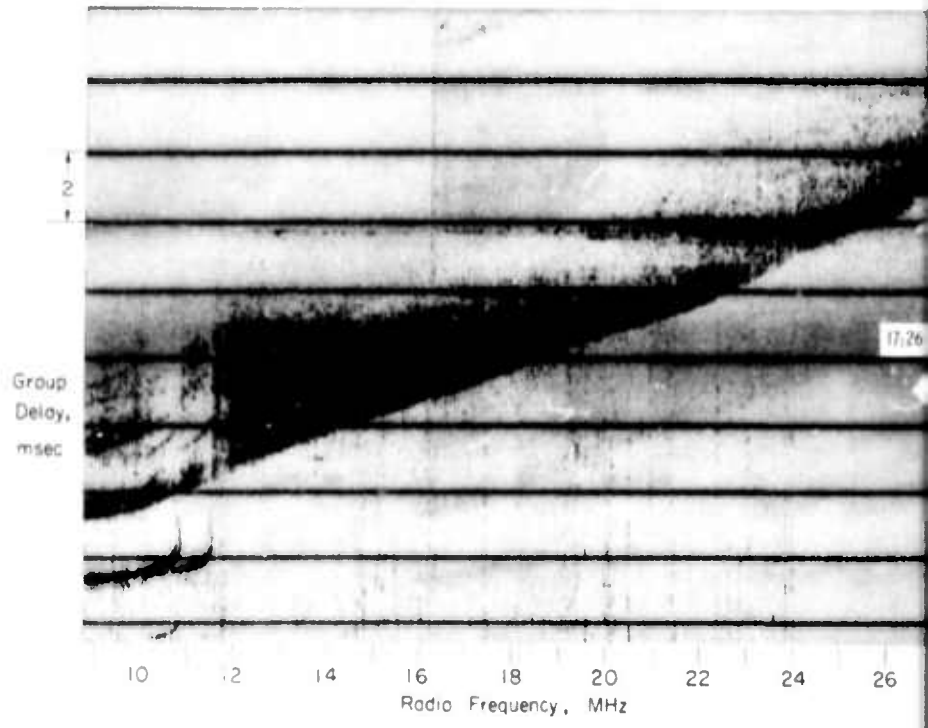
2
Group
Delay,
msec
17:26
10
12
14
16
18
20
22
24
26
Radio Frequency, MHz

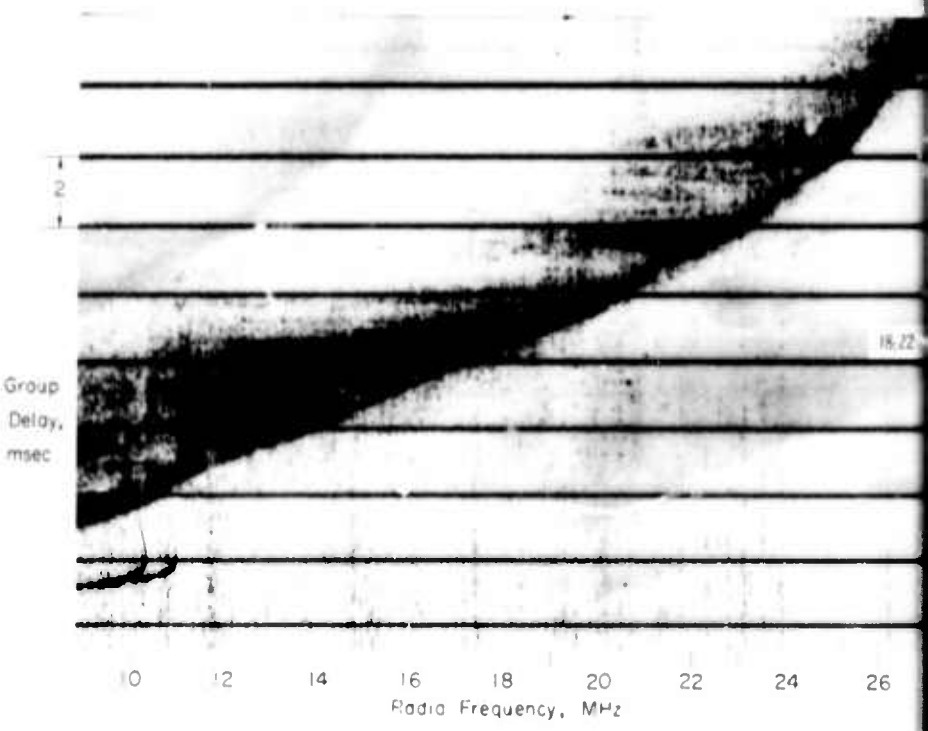
2
Group
Delay,
msec
18:22
10
12
14
16
18
20
22
24
26
Radio Frequency, MHz

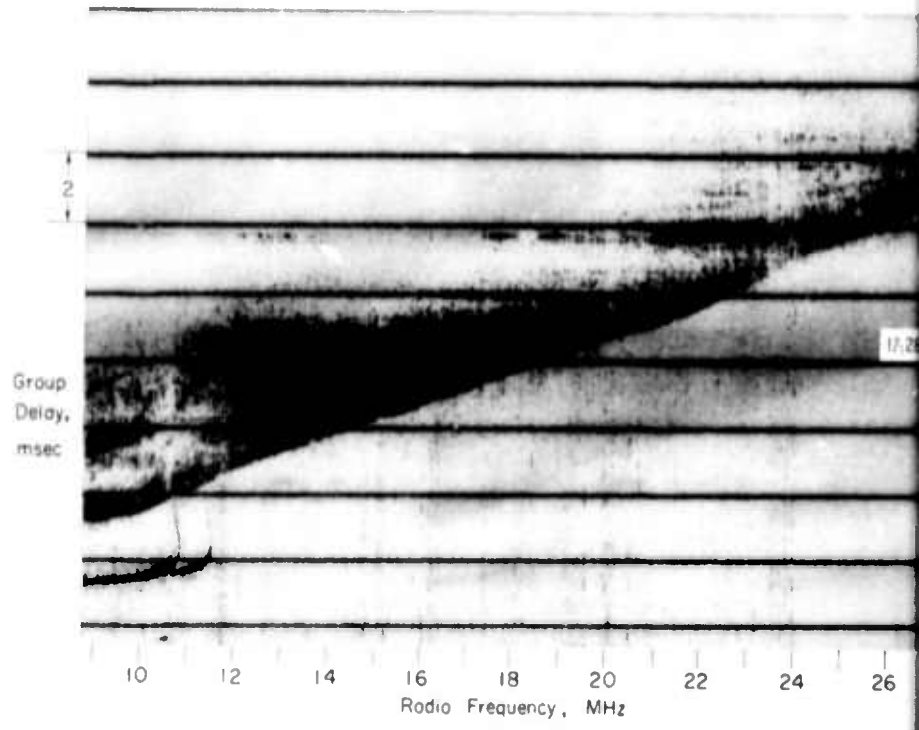
2
Group
Delay,
msec
10
12
14
16
18
20
22
24
26
Radio Frequency, MHz

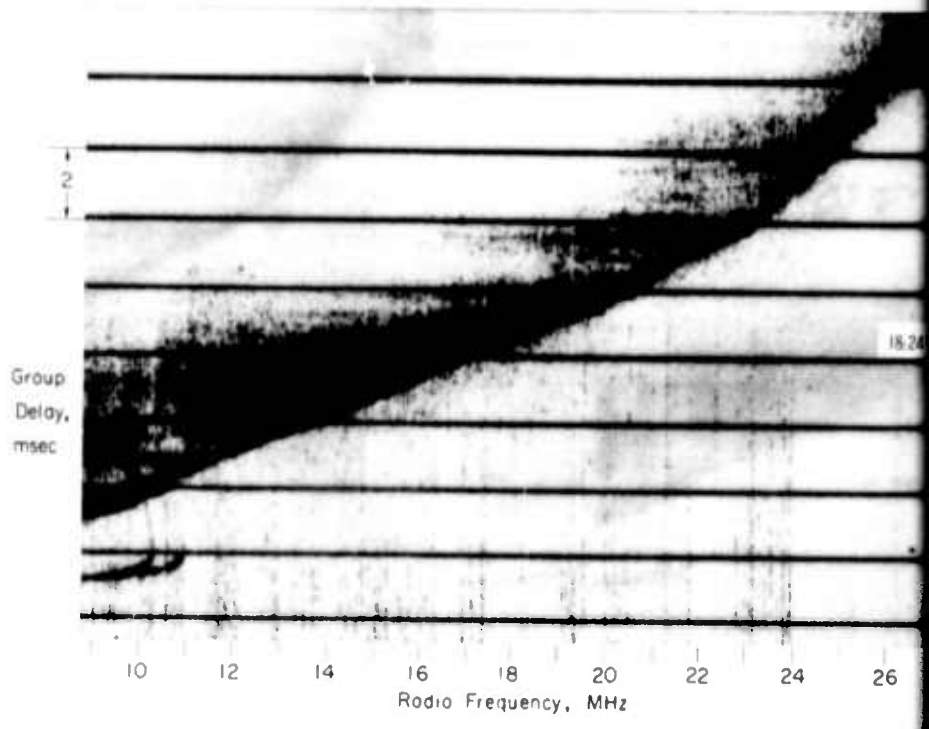
2
Group
Delay,
msec
10
12
14
16
18
20
22
24
26
Radio Frequency, MHz

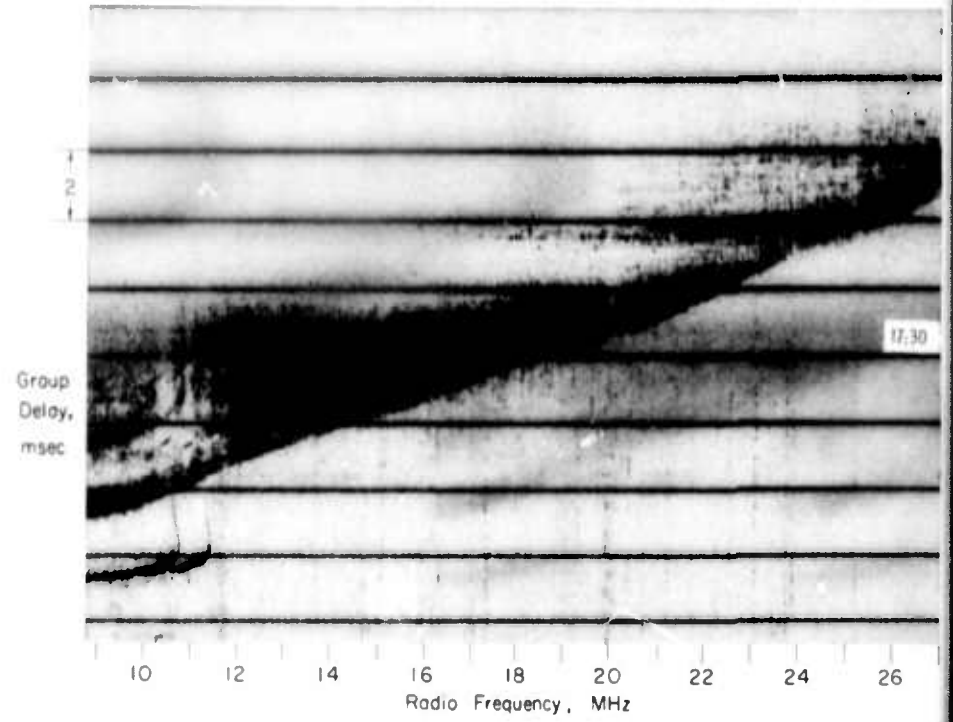
2
Group
Delay,
msec
17:30
10
12
14
16
18
20
22
24
26
Radio Frequency, MHz

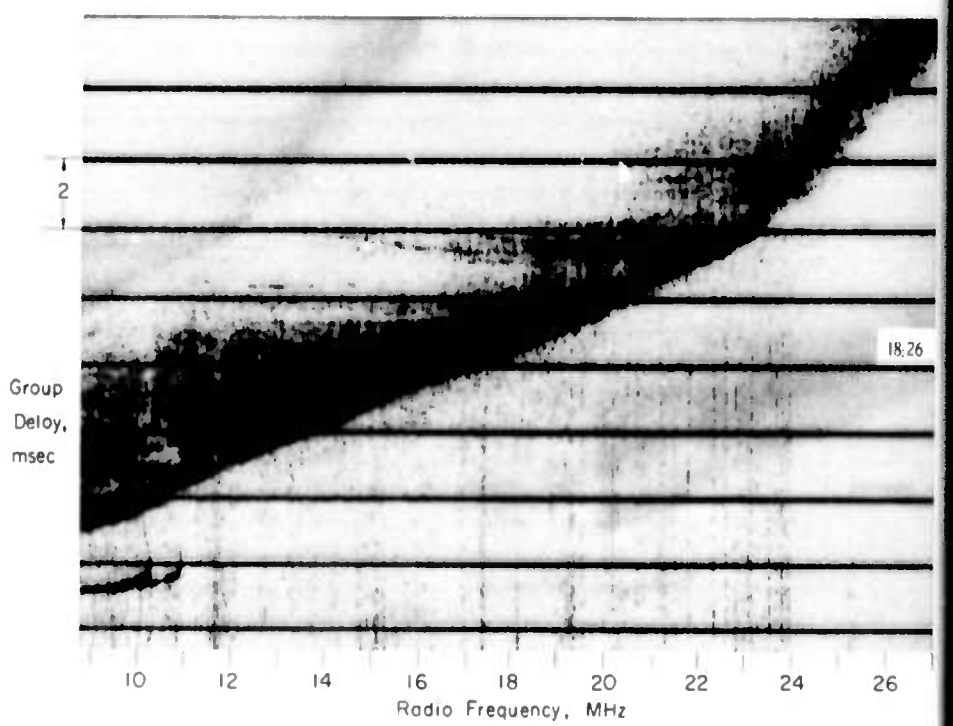
2
Group
Delay,
msec
18:26
10
12
14
16
18
20
22
24
26
Radio Frequency, MHz

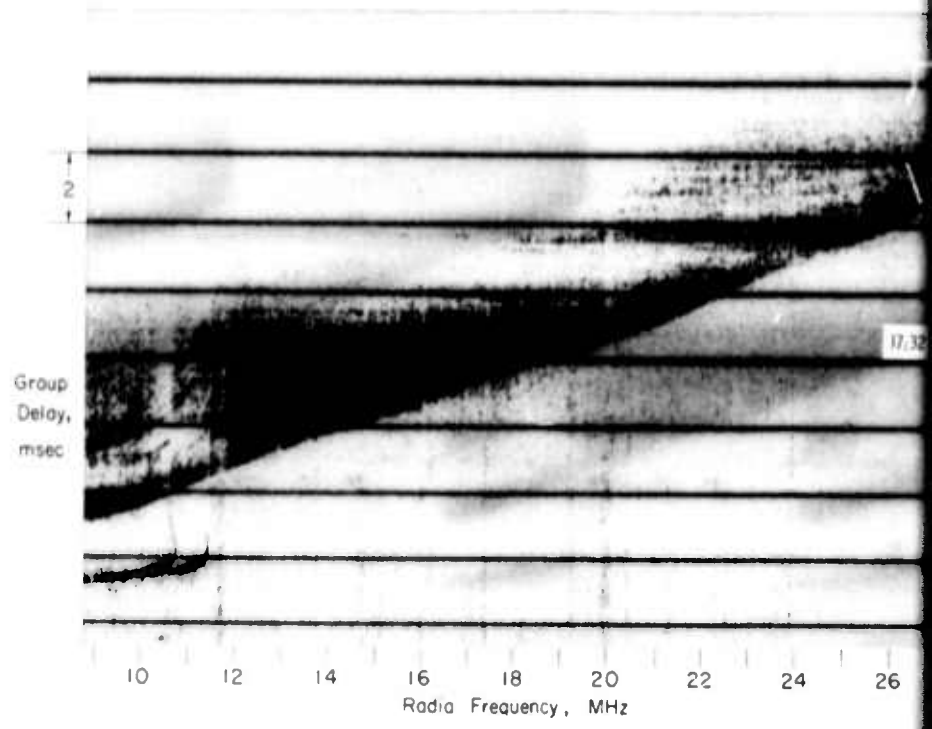
2
Group
Delay,
msec
10
12
14
16
18
20
22
24
26
Radio Frequency, MHz

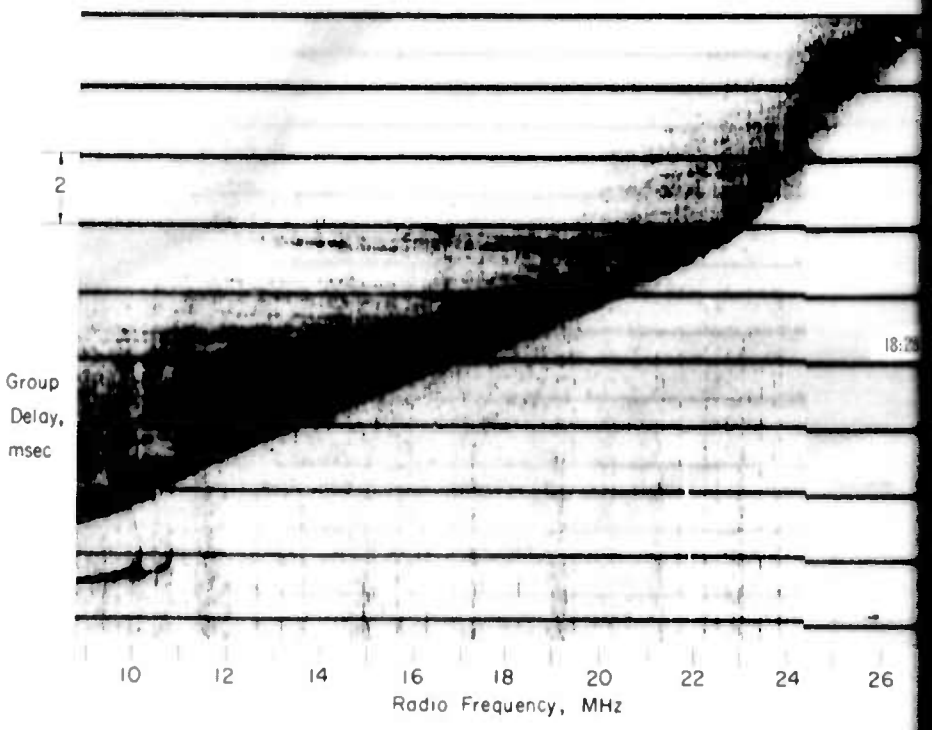
2
Group
Delay,
msec
10
12
14
16
18
20
22
24
26
Radio Frequency, MHz

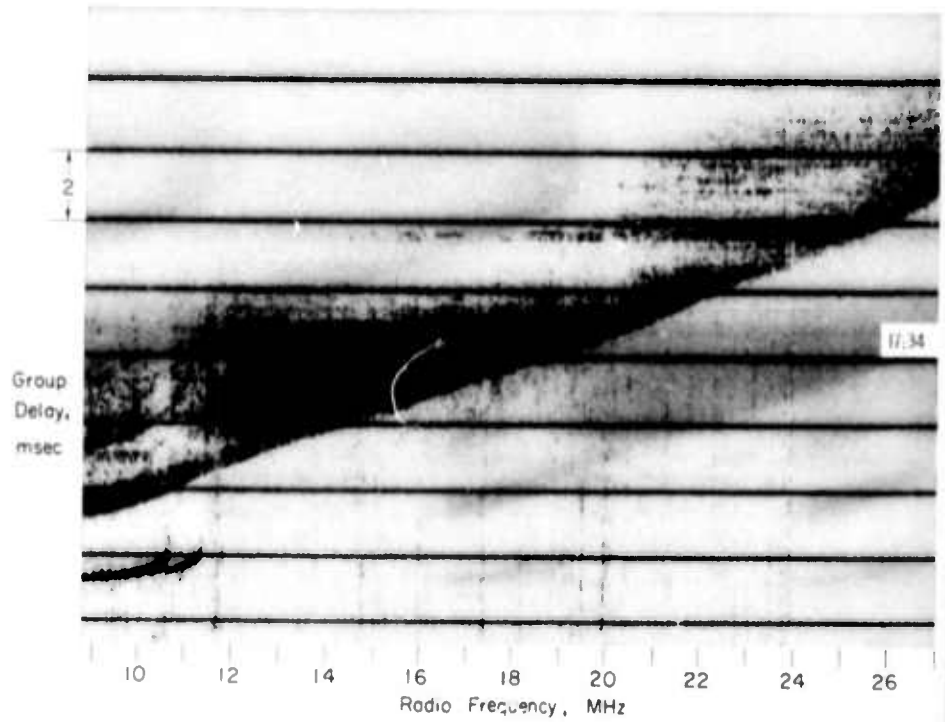
2
17:34
Group
Delay,
msec
10
12
14
16
18
20
22
24
26
Radio Frequency, MHz

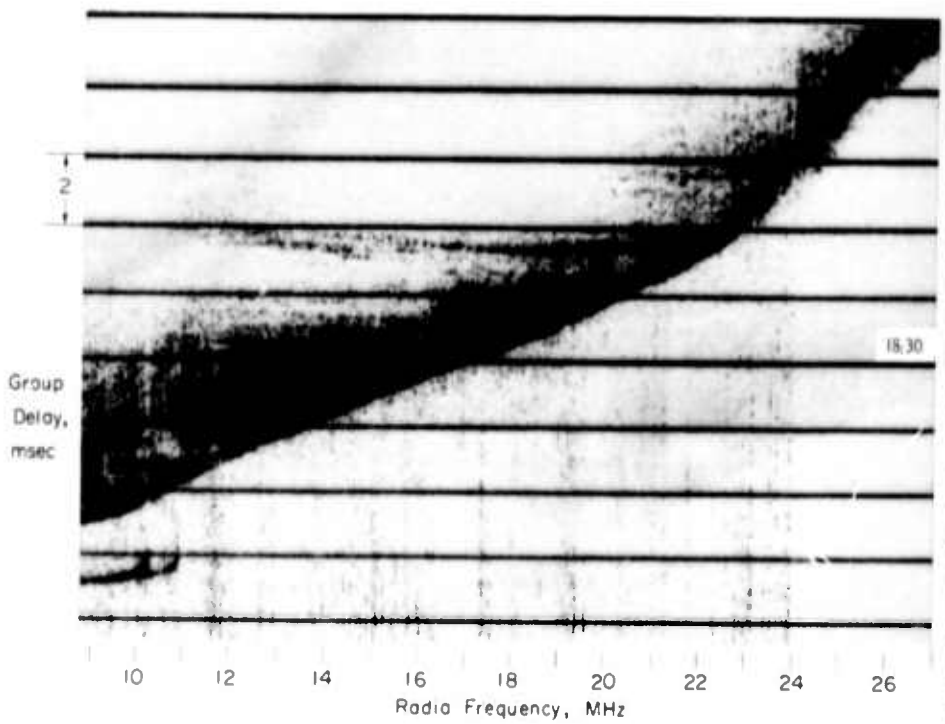
2
18:30
Group
Delay,
msec
10
12
14
16
18
20
22
24
26
Radio Frequency, MHz

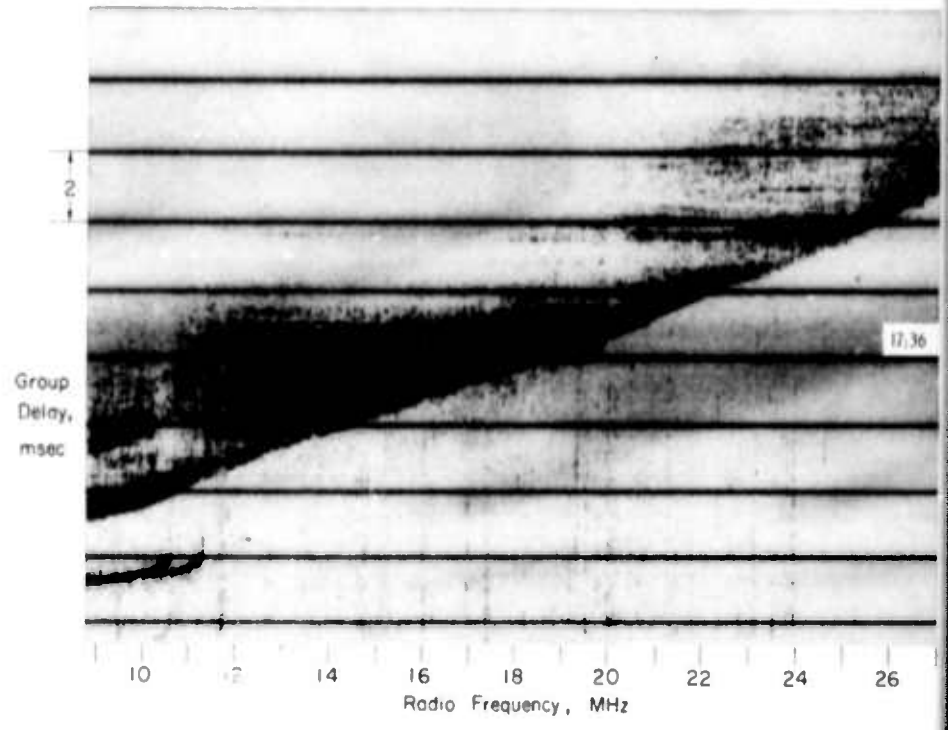
2
17:36
Group
Delay,
msec
10
12
14
16
18
20
22
24
26
Radio Frequency, MHz

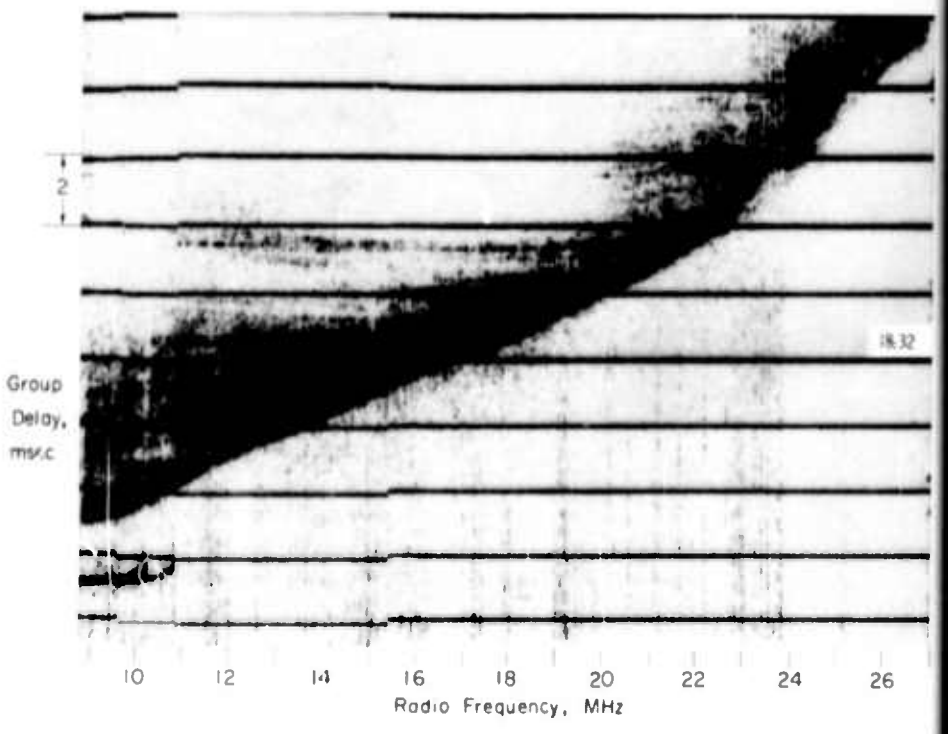
2
18:32
Group
Delay,
msec
10
12
14
16
18
20
22
24
26
Radio Frequency, MHz

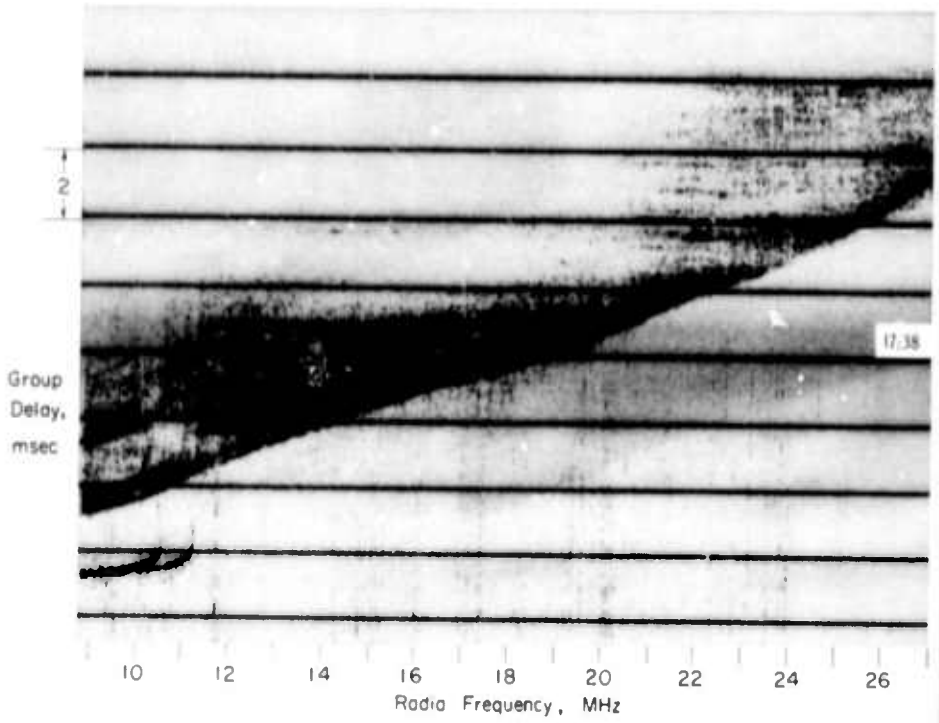
2
Group
Delay,
msec
17.38
10
12
14
16
18
20
22
24
26
Radio Frequency, MHz

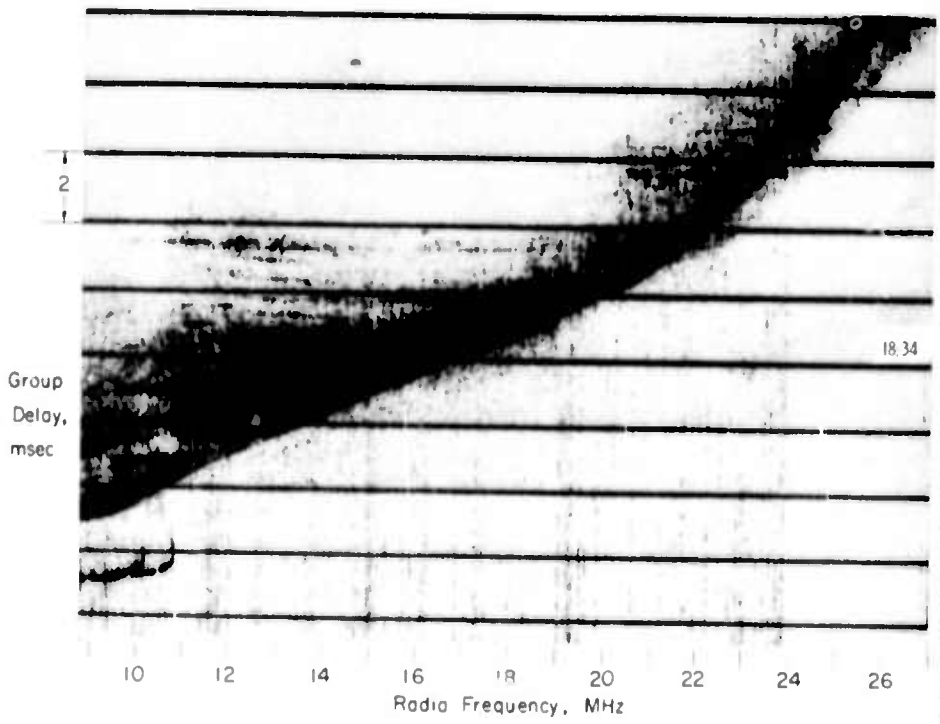
2
Group
Delay,
msec
18.34
10
12
14
16
18
20
22
24
26
Radio Frequency, MHz

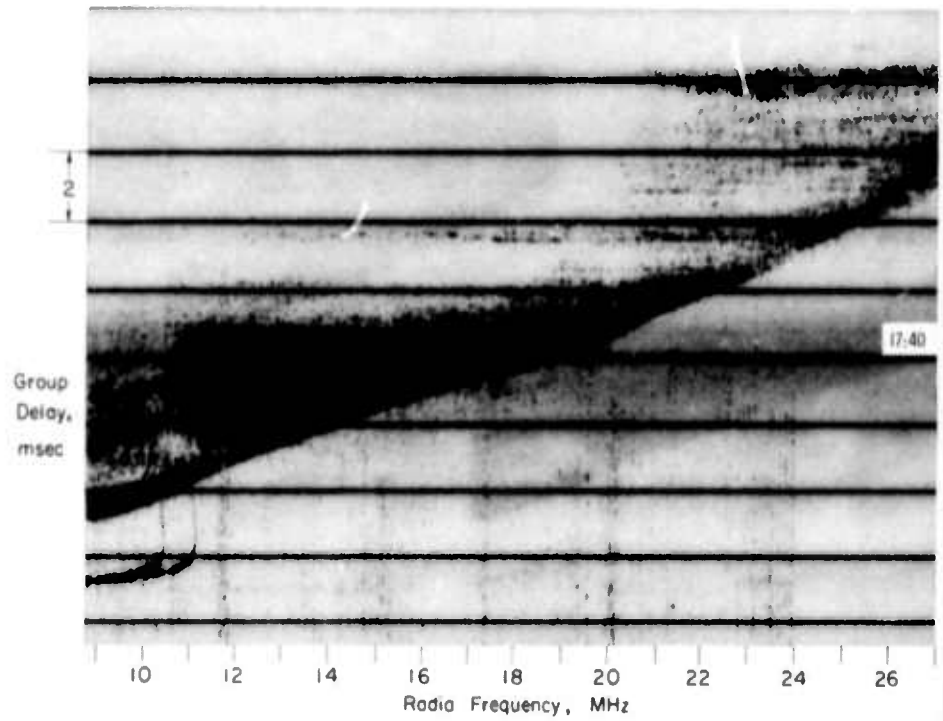
2
17:40
Group
Delay,
msec
10
12
14
16
18
20
22
24
26
Radio Frequency, MHz

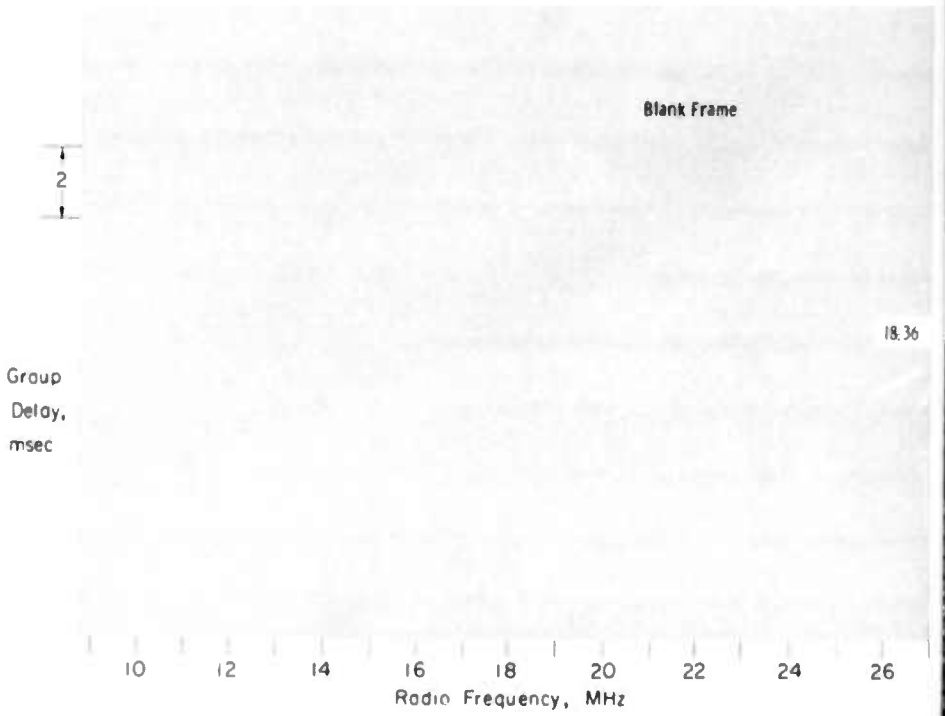
Blank Frame
2
18:36
Group
Delay,
msec
10
12
14
16
18
20
22
24
26
Radio Frequency, MHz

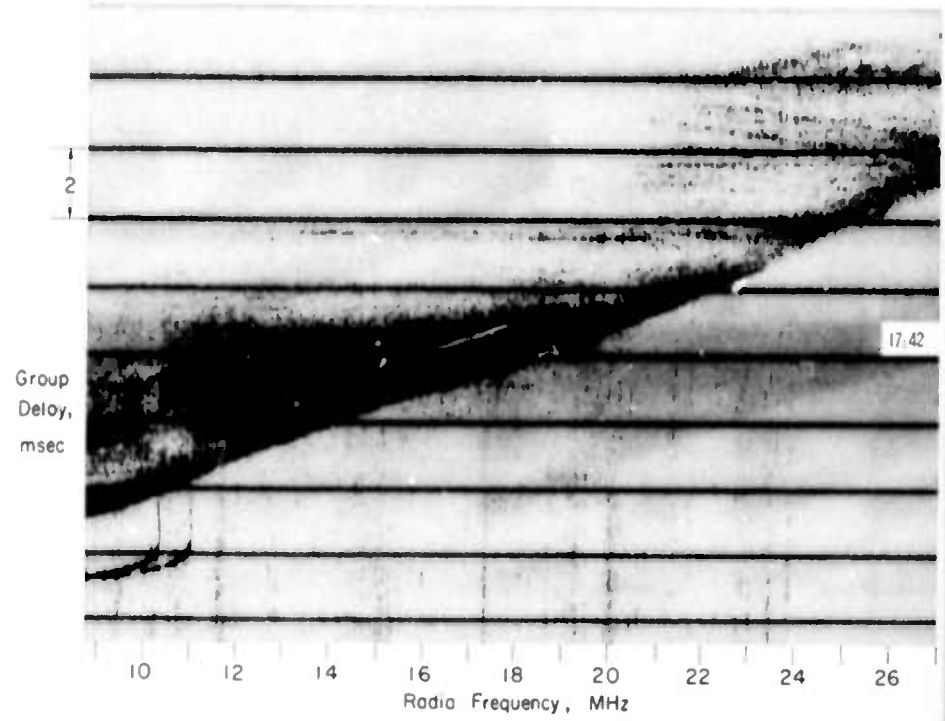
2
17:42
Group
Delay,
msec
10
12
14
16
18
20
22
24
26
Radio Frequency, MHz

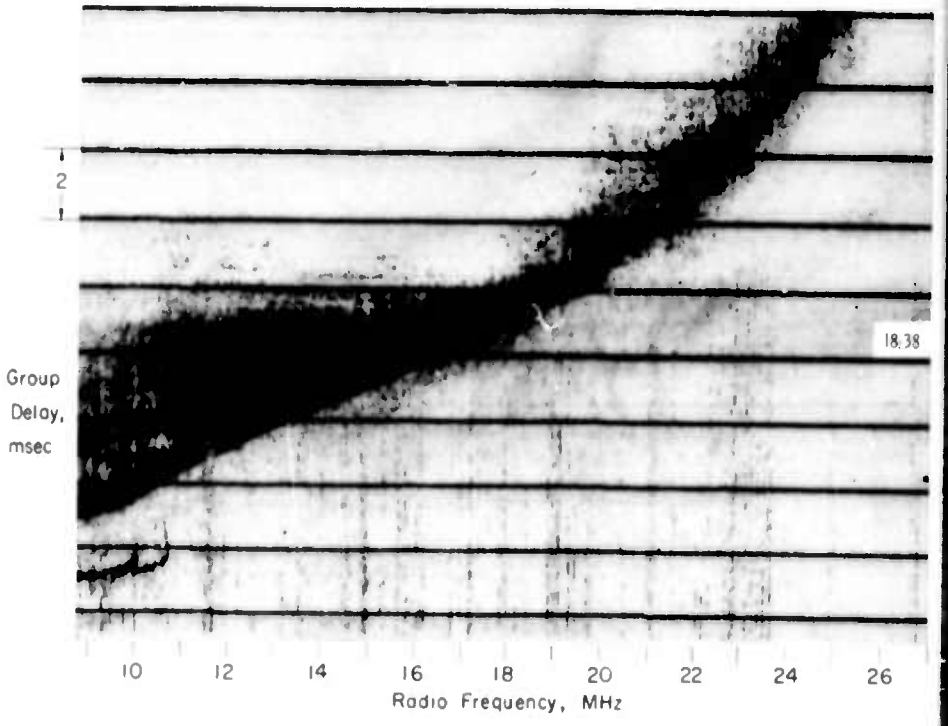
2
18:38
Group
Delay,
msec
10
12
14
16
18
20
22
24
26
Radio Frequency, MHz

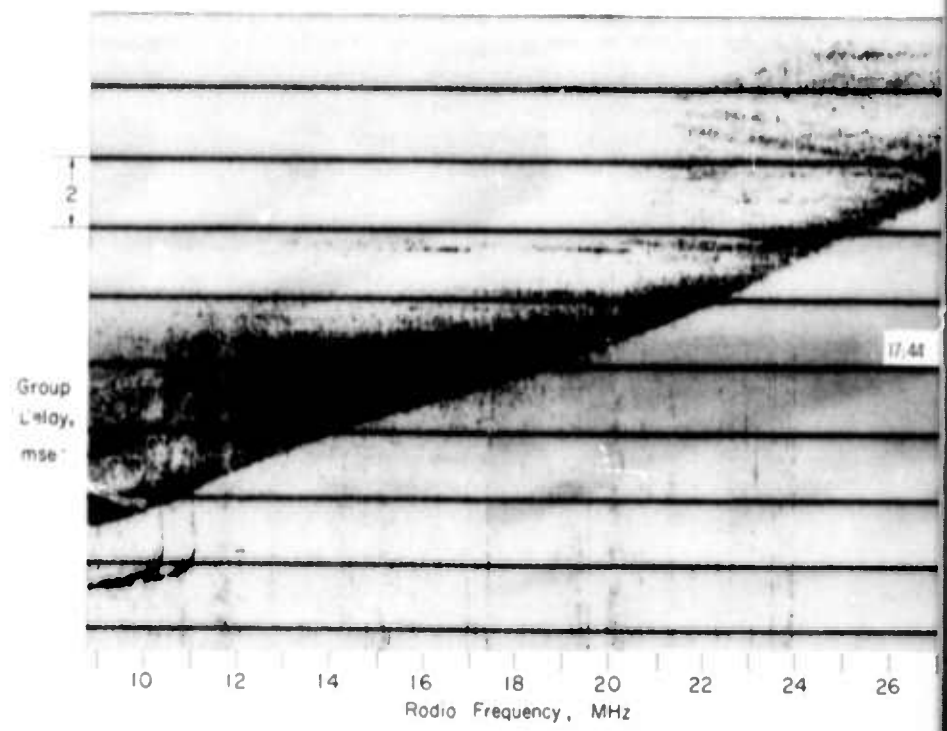
2
Group
Delay,
msec
17.48
10
12
14
16
18
20
22
24
26
Radio Frequency, MHz

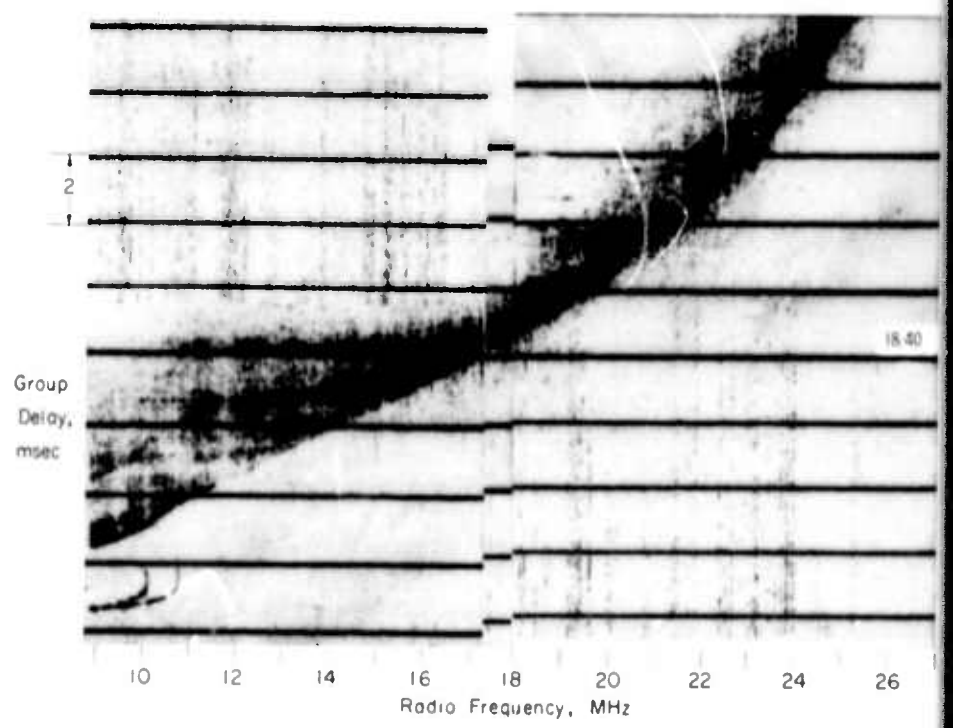
2
Group
Delay,
msec
18.40
10
12
14
16
18
20
22
24
26
Radio Frequency, MHz

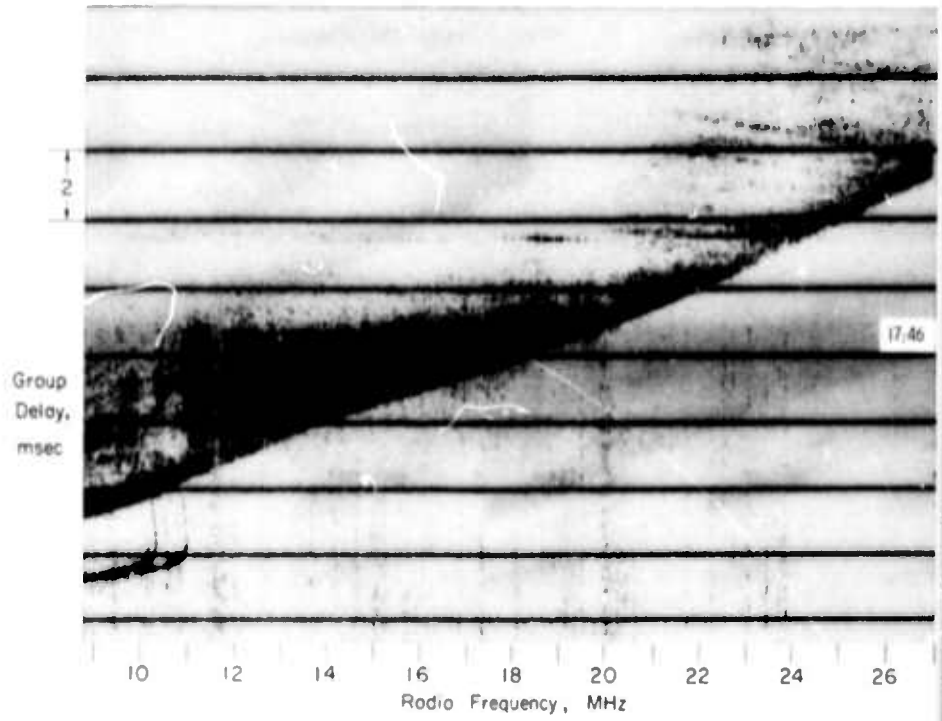
2
17:46
Group
Delay,
msec
10
12
14
16
18
20
22
24
26
Radio Frequency, MHz

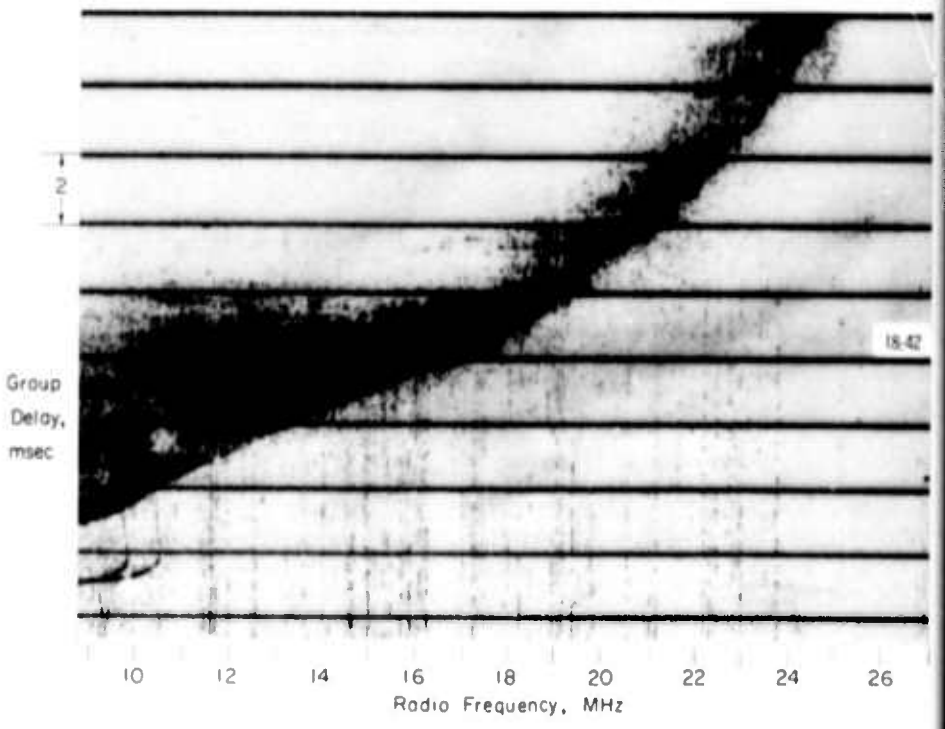
2
18:42
Group
Delay,
msec
10
12
14
16
18
20
22
24
26
Radio Frequency, MHz

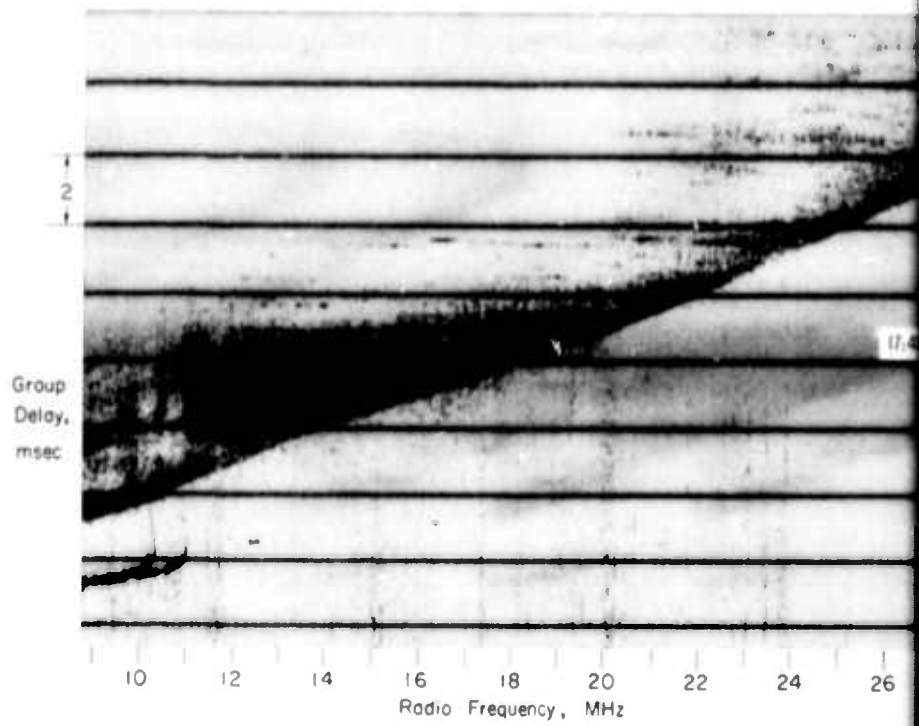
2
Group
Delay,
msec
10
12
14
16
18
20
22
24
26
Radio Frequency, MHz

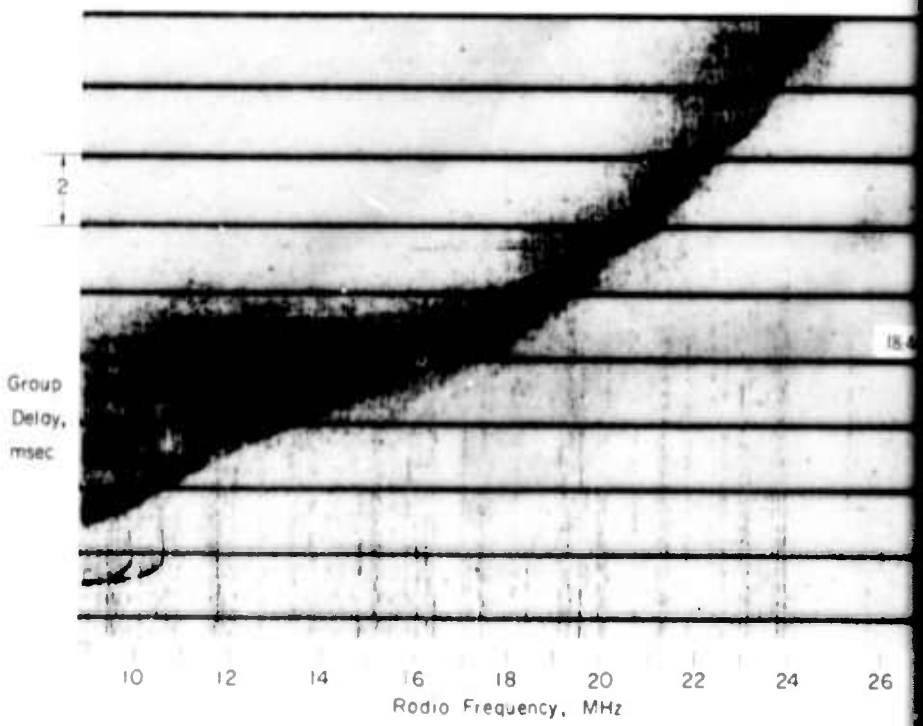
2
Group
Delay,
msec
10
12
14
16
18
20
22
24
26
Radio Frequency, MHz

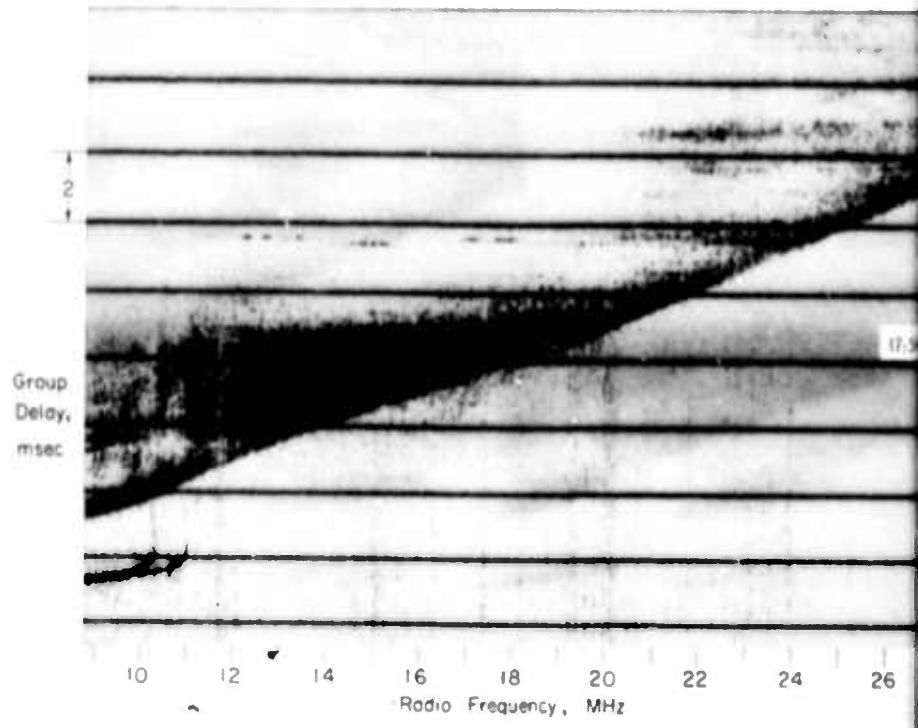
2
Group
Delay,
msec
10
12
14
16
18
20
22
24
26
Radio Frequency, MHz

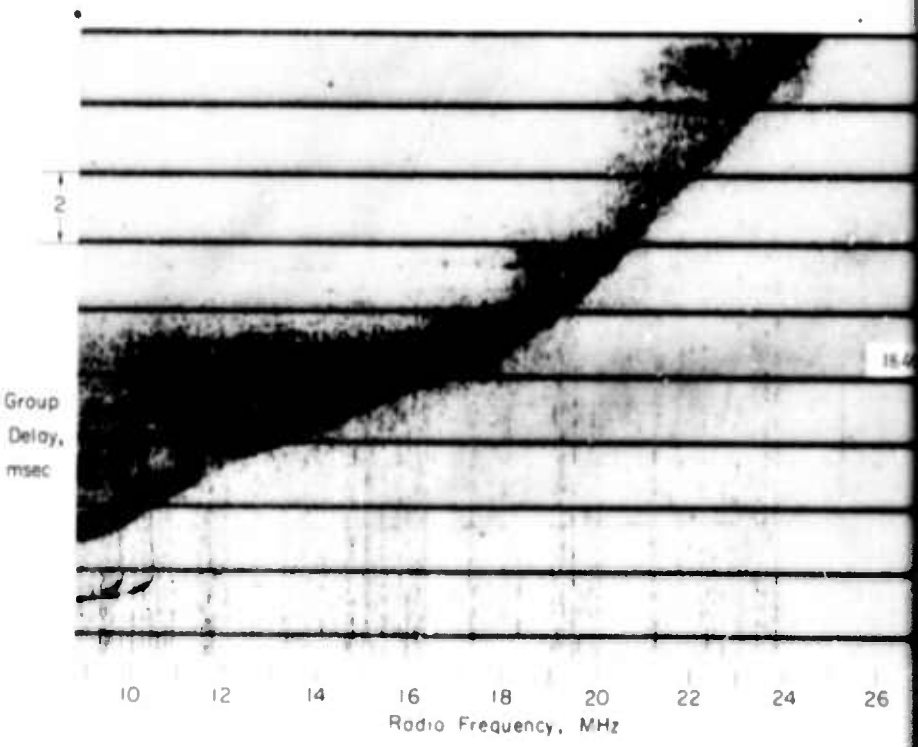
2
Group
Delay,
msec
10
12
14
16
18
20
22
24
26
Radio Frequency, MHz

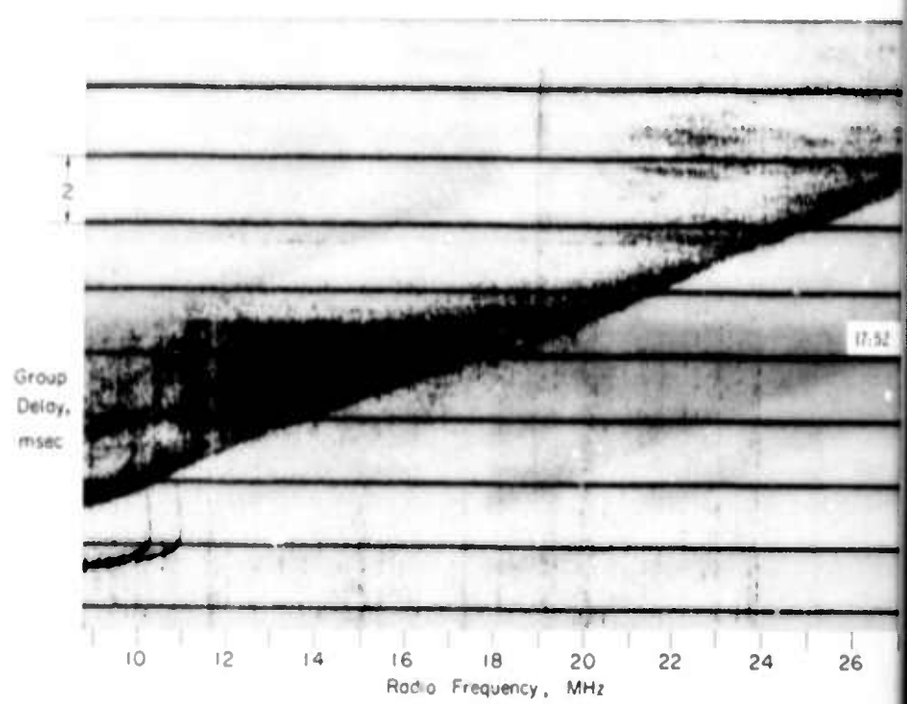
2
Group
Delay,
msec
17:52
10
12
14
16
18
20
22
24
26
Radio Frequency, MHz

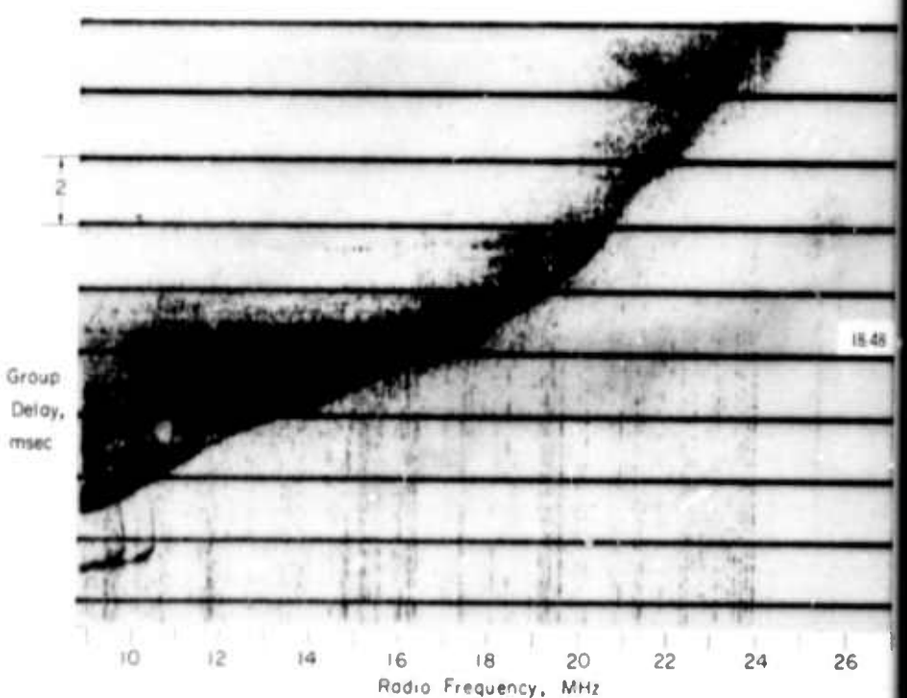
2
Group
Delay,
msec
18:48
10
12
14
16
18
20
22
24
26
Radio Frequency, MHz

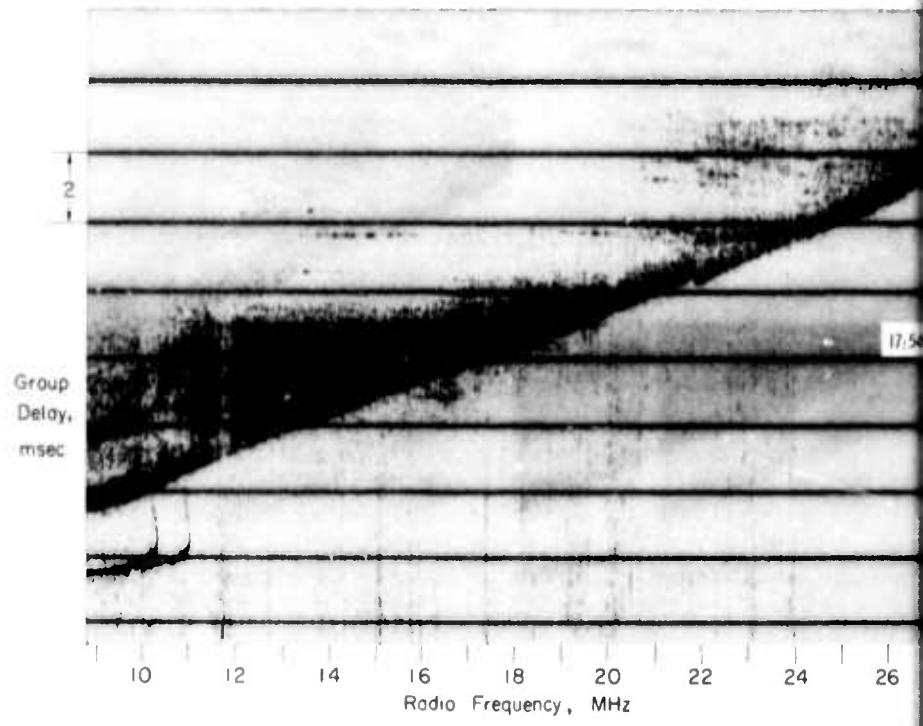
2
Group
Delay,
msec
10
12
14
16
18
20
22
24
26
Radio Frequency, MHz

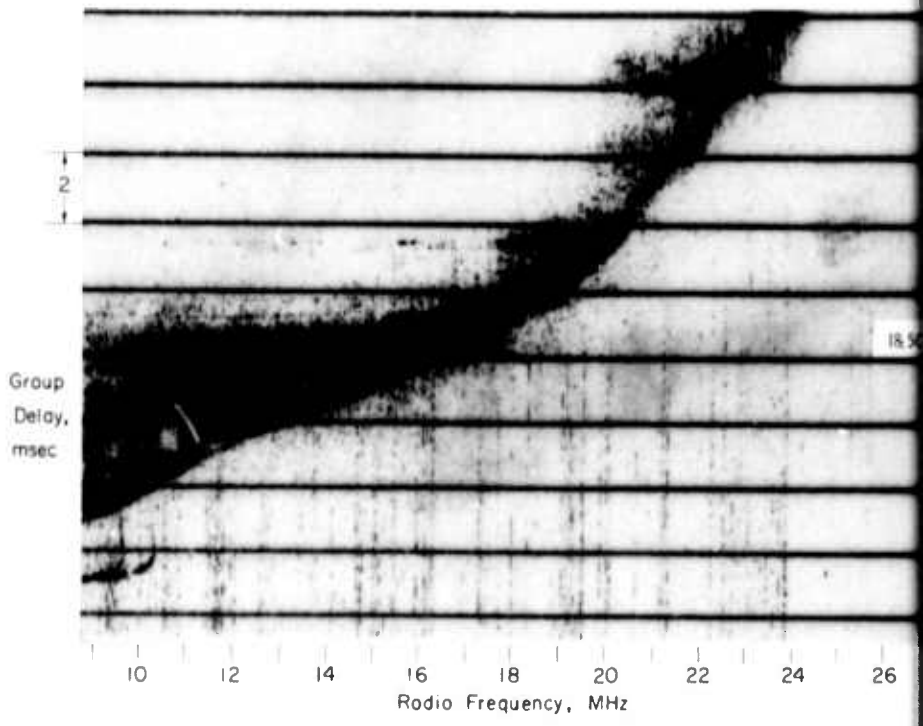
2
Group
Delay,
msec
10
12
14
16
18
20
22
24
26
Radio Frequency, MHz

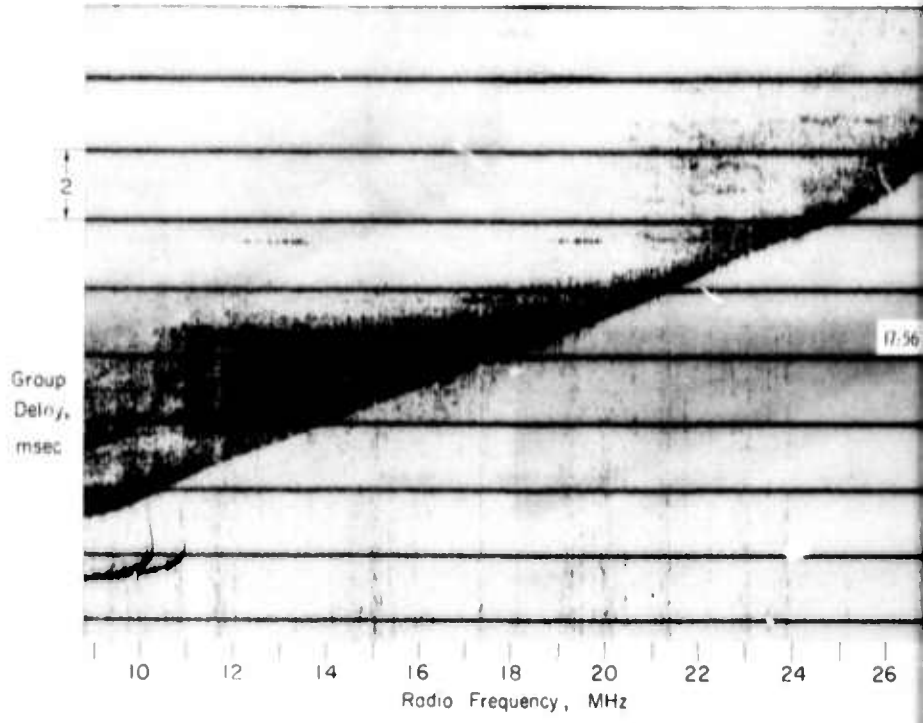
2
Group
Delay,
msec
17:56
10
12
14
16
18
20
22
24
26
Radio Frequency, MHz

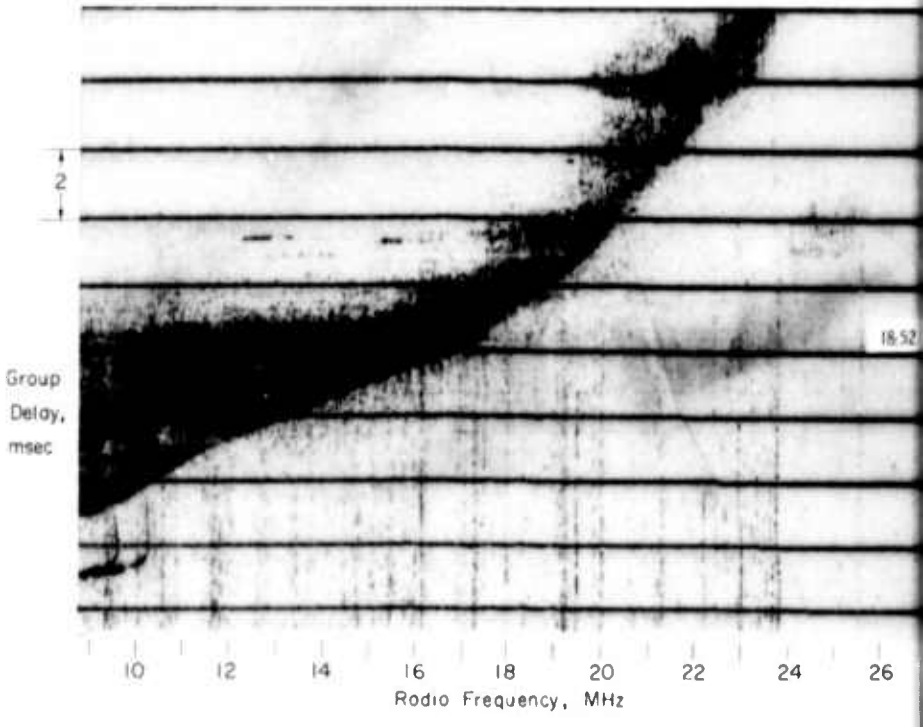
2
Group
Delay,
msec
18:52
10
12
14
16
18
20
22
24
26
Radio Frequency, MHz

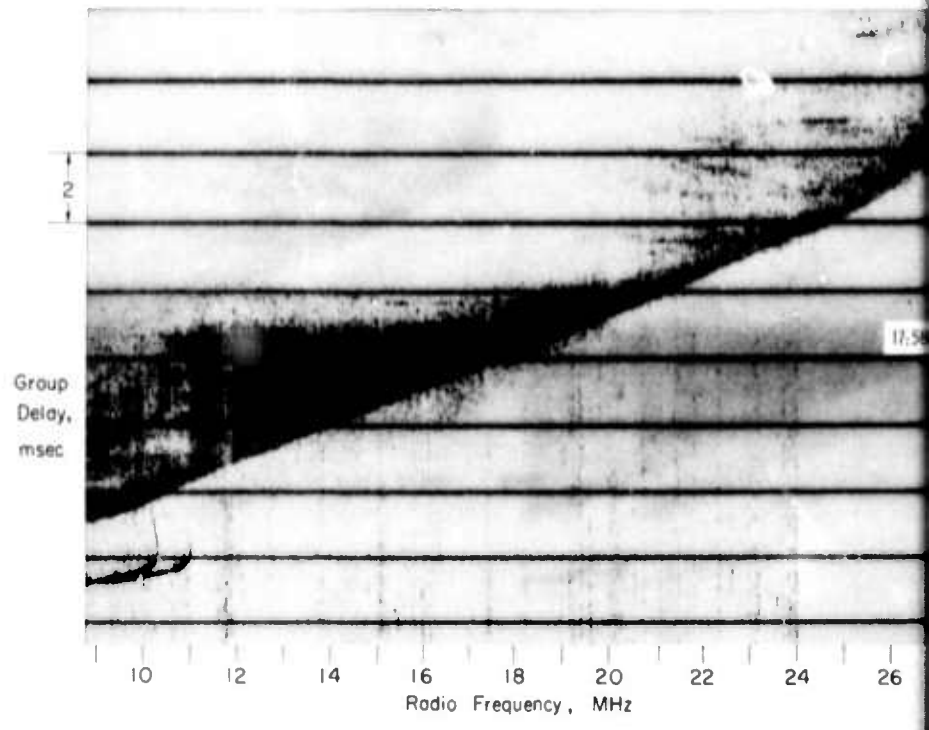
2
Group
Delay,
msec
10
12
14
16
18
20
22
24
26
Radio Frequency, MHz

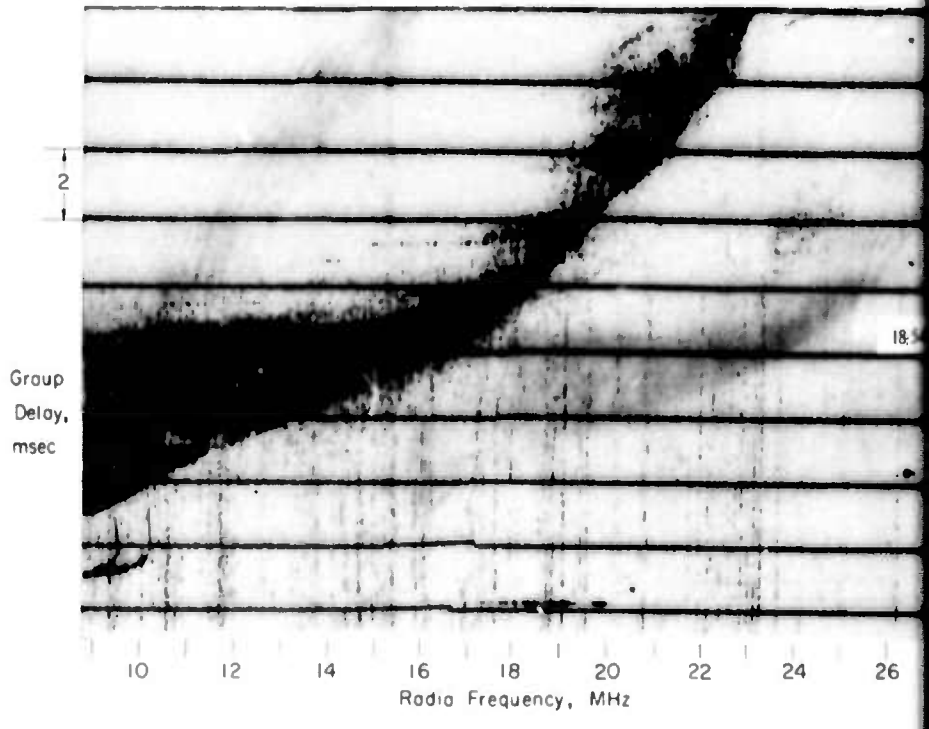
2
Group
Delay,
msec
10
12
14
16
18
20
22
24
26
Radio Frequency, MHz

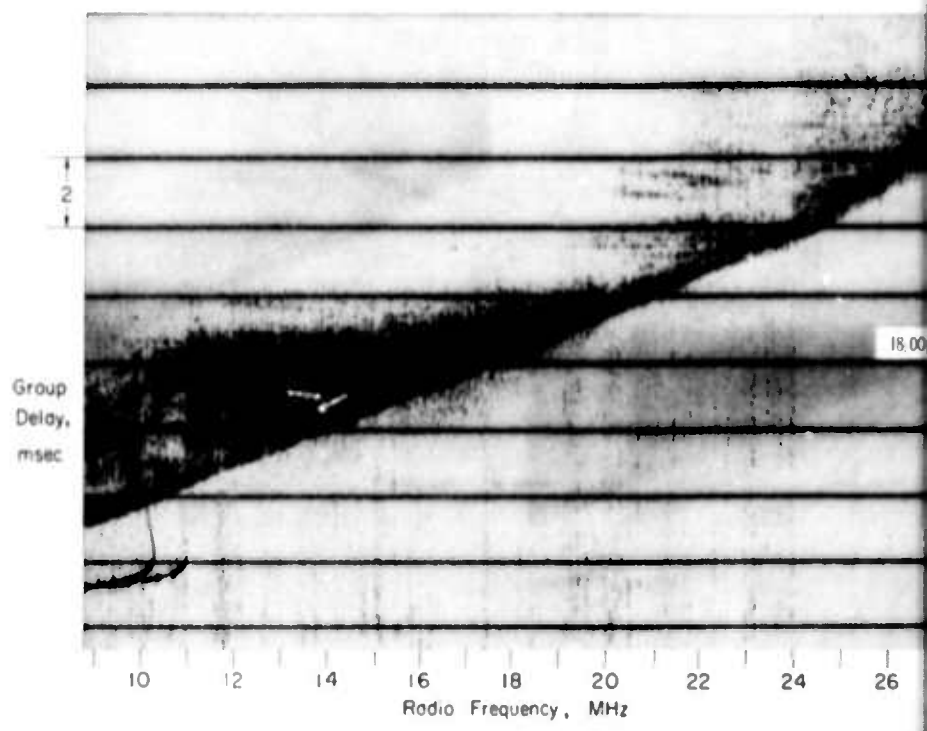
2
18.00
Group
Delay,
msec
10
12
14
16
18
20
22
24
26
Radio Frequency, MHz

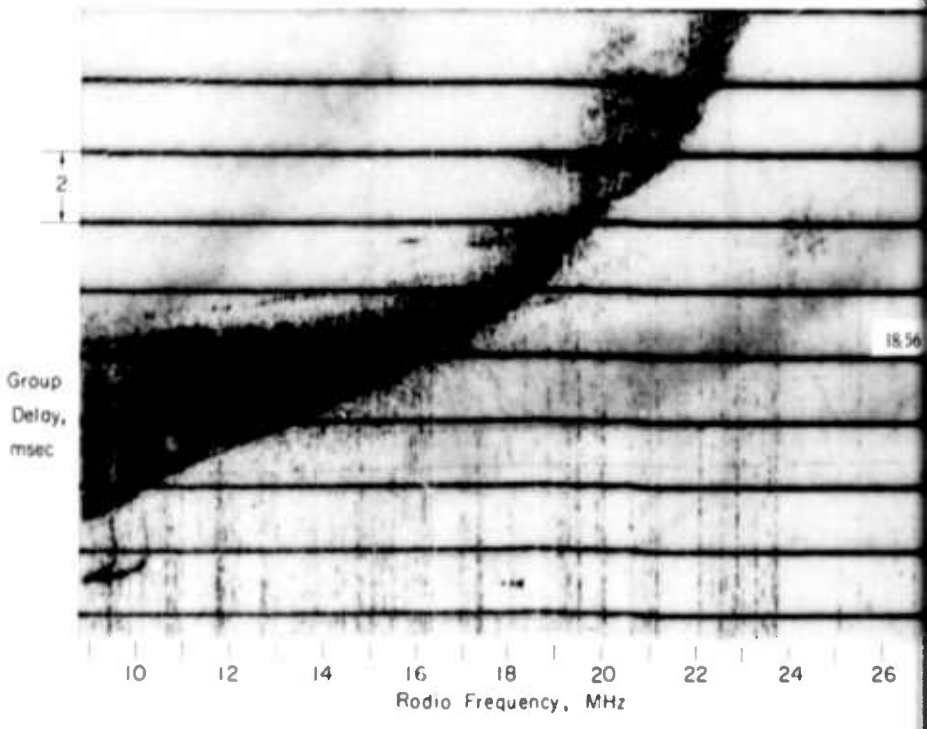
2
18.56
Group
Delay,
msec
10
12
14
16
18
20
22
24
26
Radio Frequency, MHz

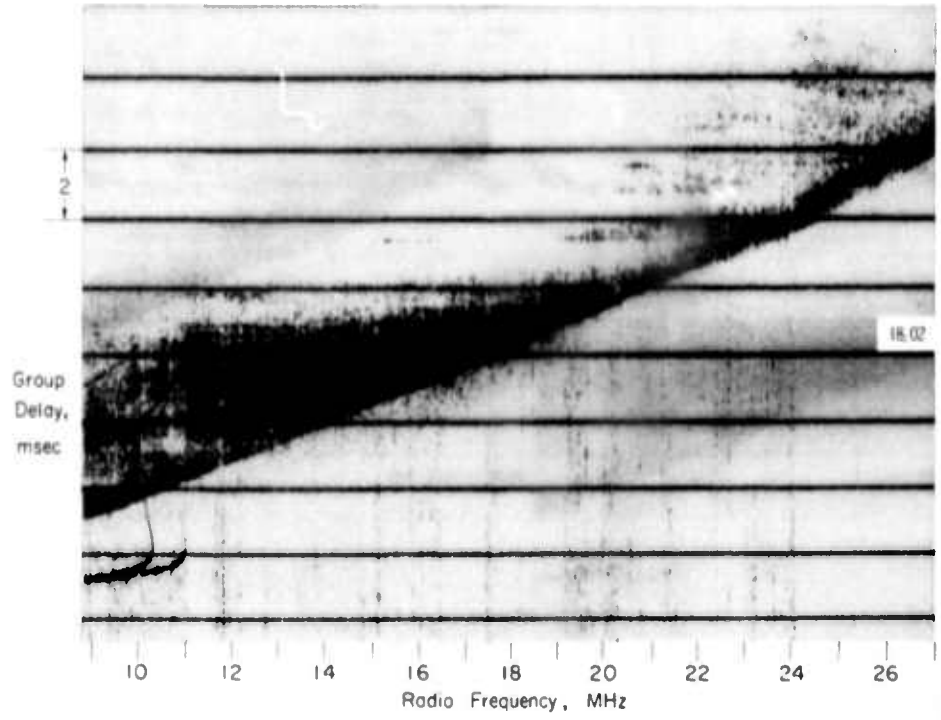
2
Group
Delay,
msec
18:02
10
12
14
16
18
20
22
24
26
Radio Frequency, MHz

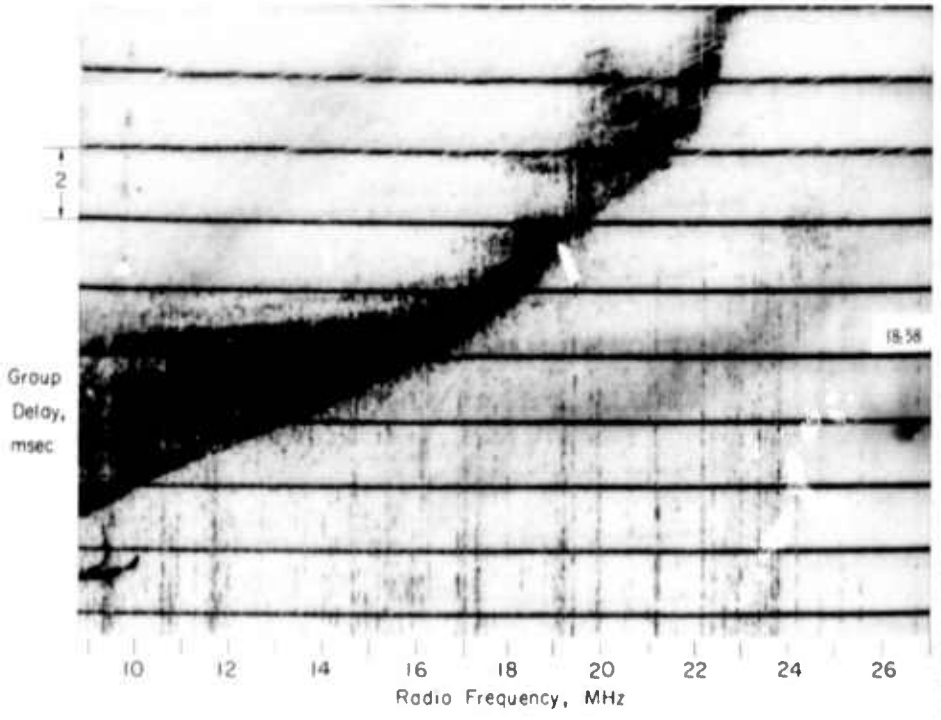
2
Group
Delay,
msec
18:58
10
12
14
16
18
20
22
24
26
Radio Frequency, MHz

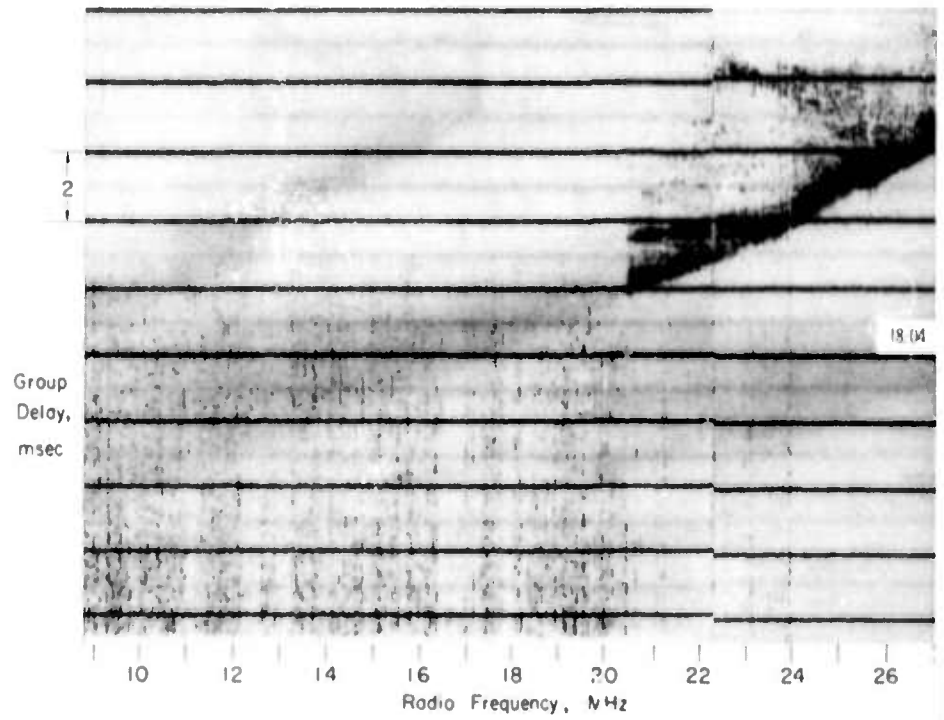
2
18.04
Group
Delay,
msec
10
12
14
16
18
20
22
24
26
Radio Frequency, MHz

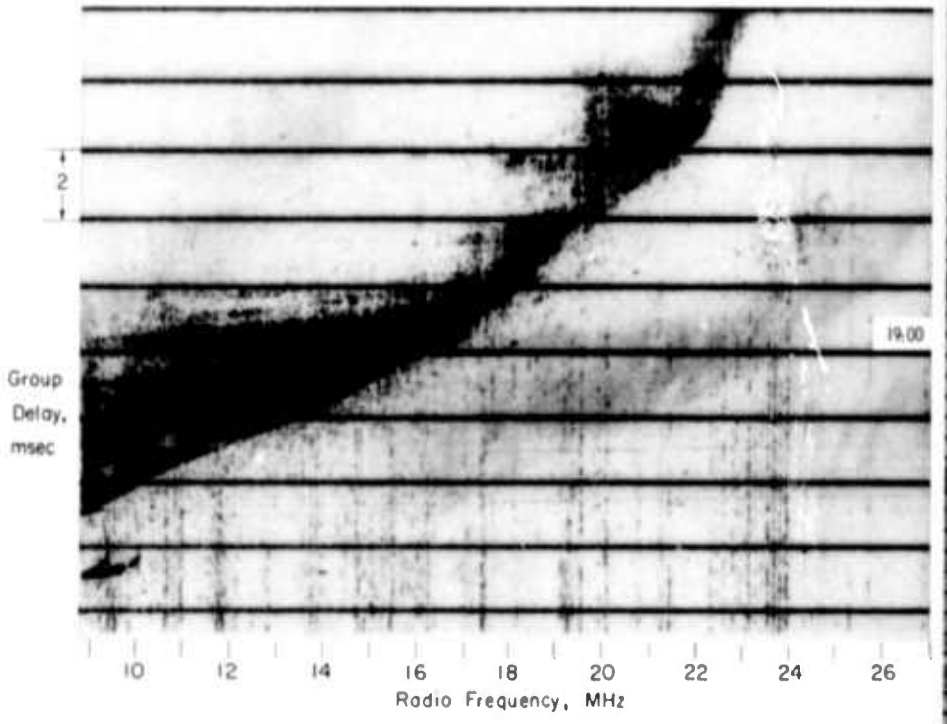
2
19.00
Group
Delay,
msec
10
12
14
16
18
20
22
24
26
Radio Frequency, MHz

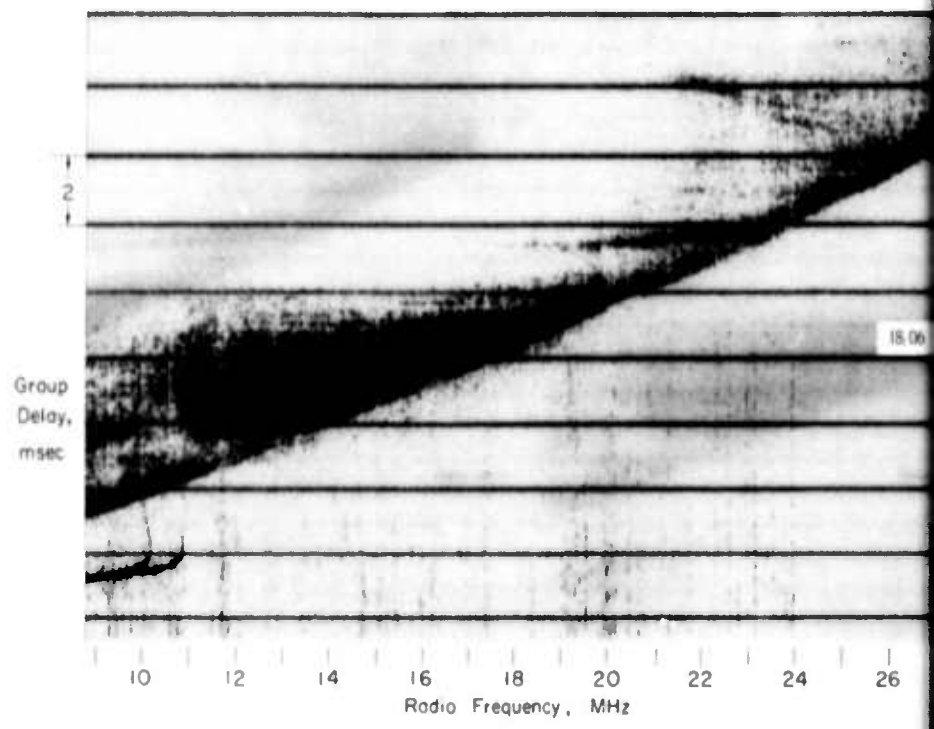
2
Group
Delay,
msec
10
12
14
16
18
20
22
24
26
Radio Frequency, MHz

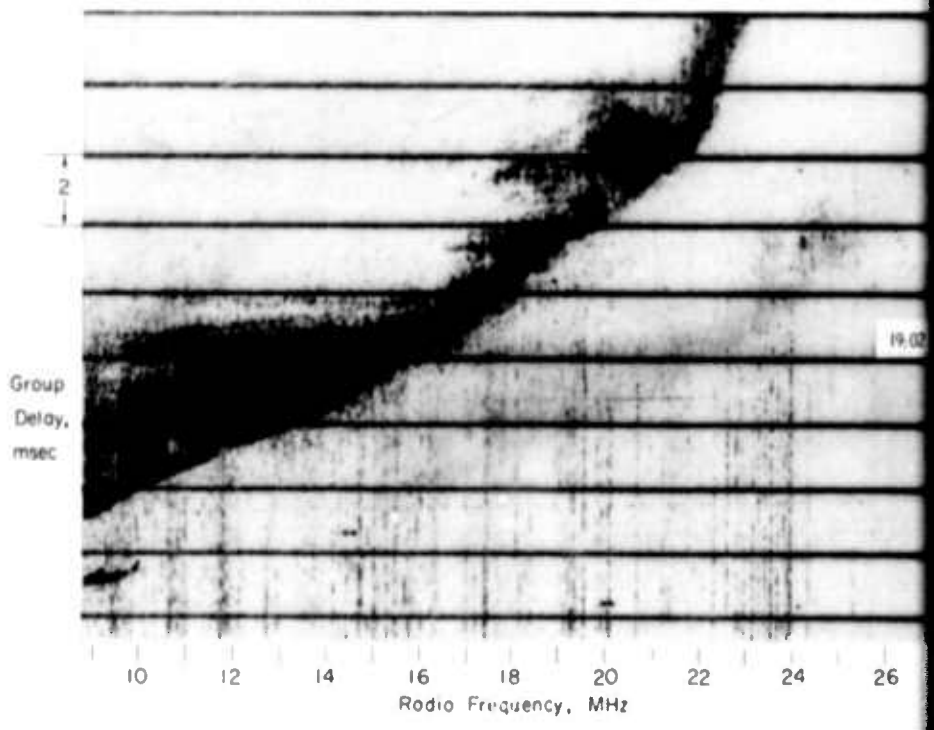
2
Group
Delay,
msec
10
12
14
16
18
20
22
24
26
Radio Frequency, MHz

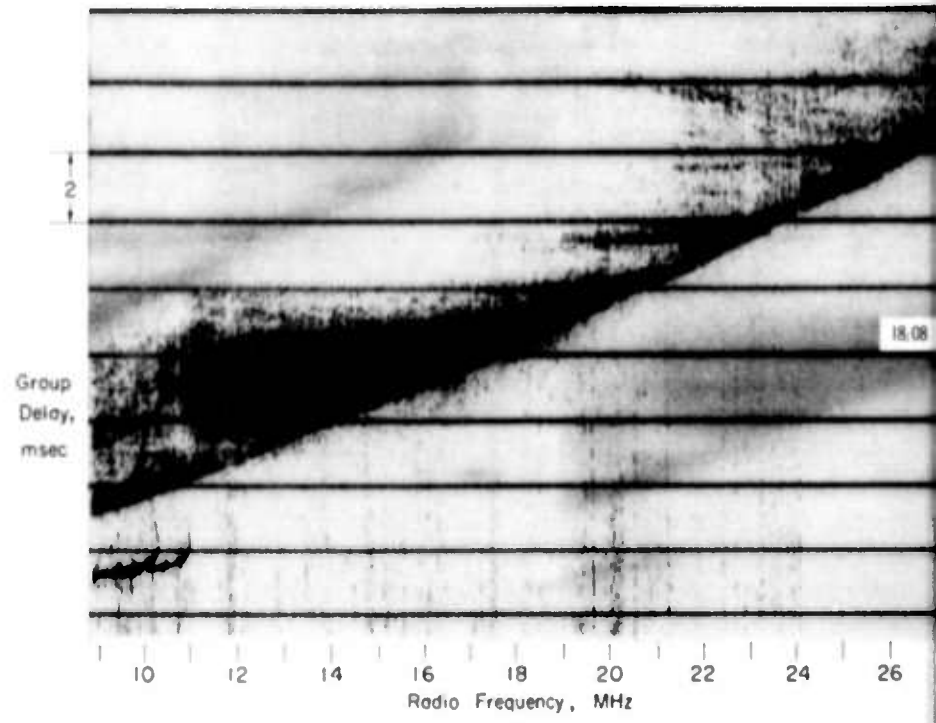
2
Group
Delay,
msec
18.08
10
12
14
16
18
20
22
24
26
Radio Frequency, MHz

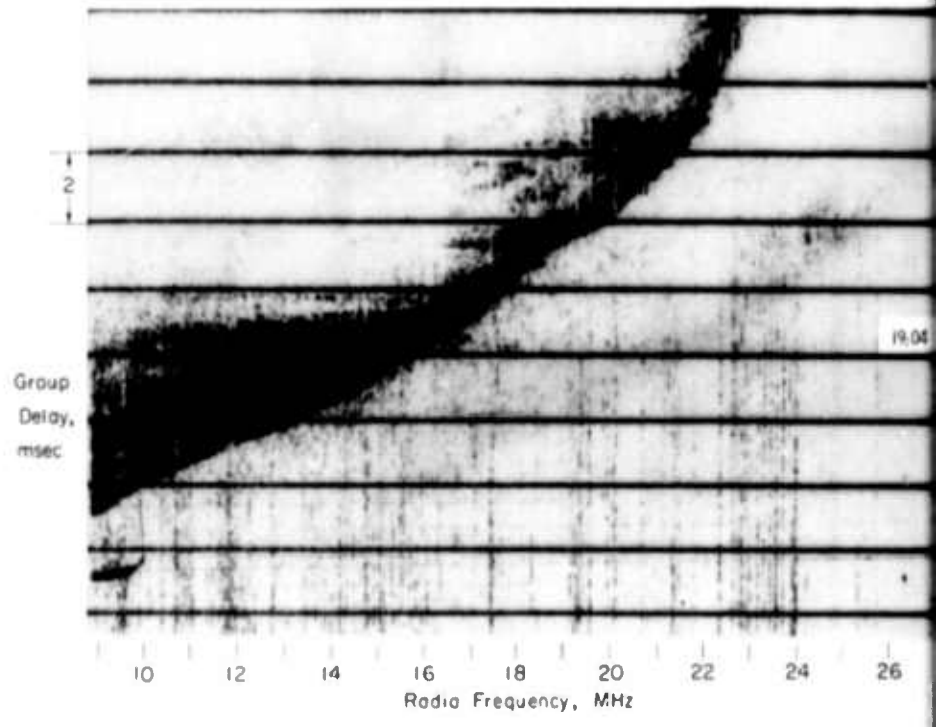
2
Group
Delay,
msec
19.04
10
12
14
16
18
20
22
24
26
Radio Frequency, MHz

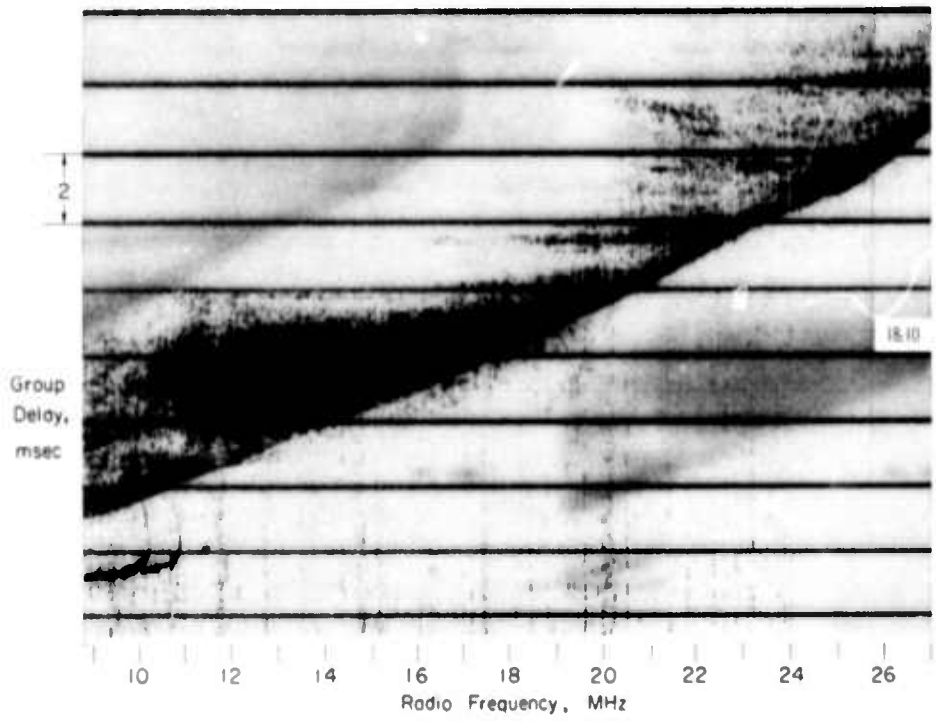
2
Group
Delay,
msec
18.10
10
12
14
16
18
20
22
24
26
Radio Frequency, MHz

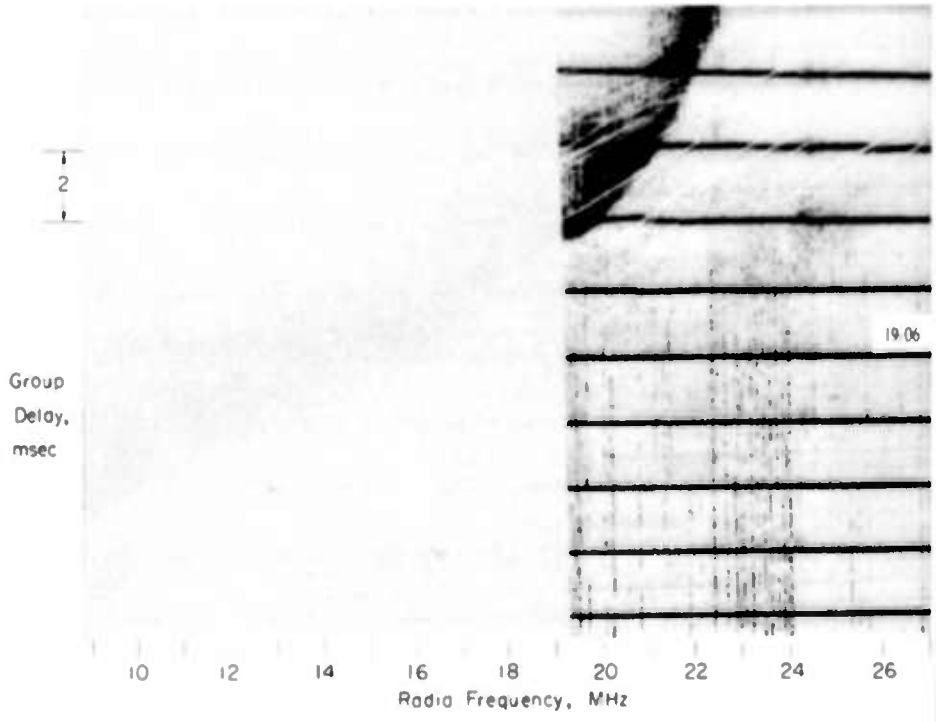
2
Group
Delay,
msec
19.06
10
12
14
16
18
20
22
24
26
Radio Frequency, MHz

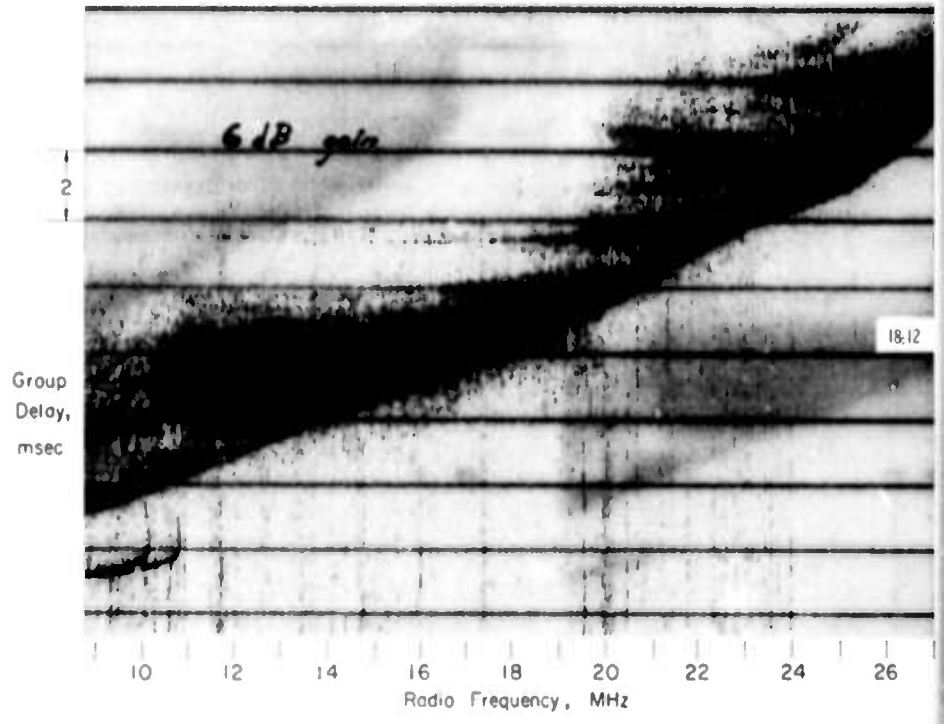
6 dB gate
2
18:12
Group
Delay,
msec
10
12
14
16
18
20
22
24
26
Radio Frequency, MHz

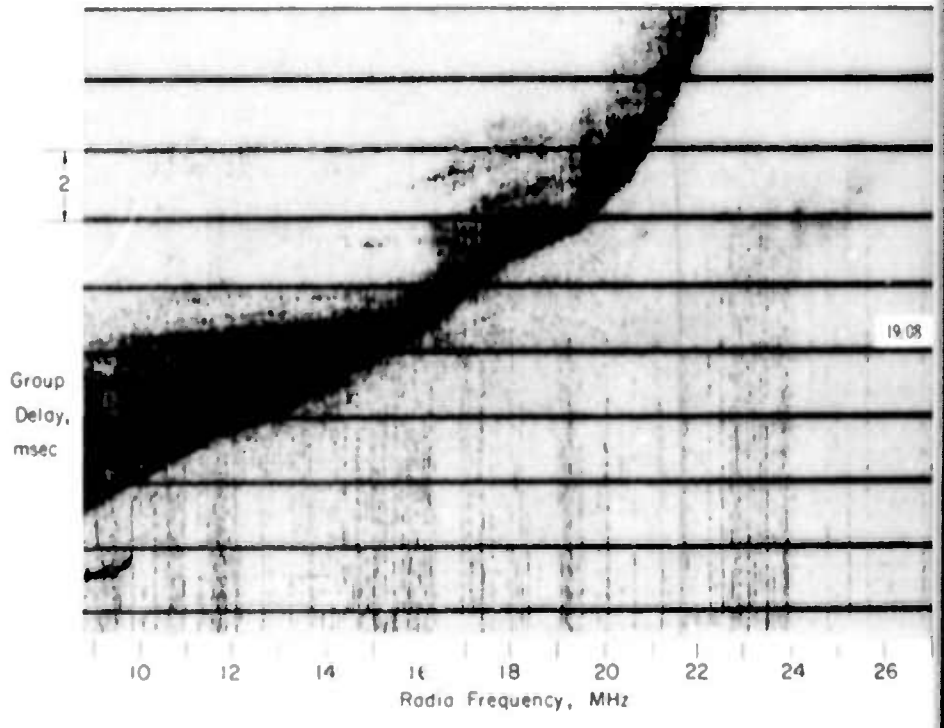
2
19:08
Group
Delay,
msec
10
12
14
16
18
20
22
24
26
Radio Frequency, MHz

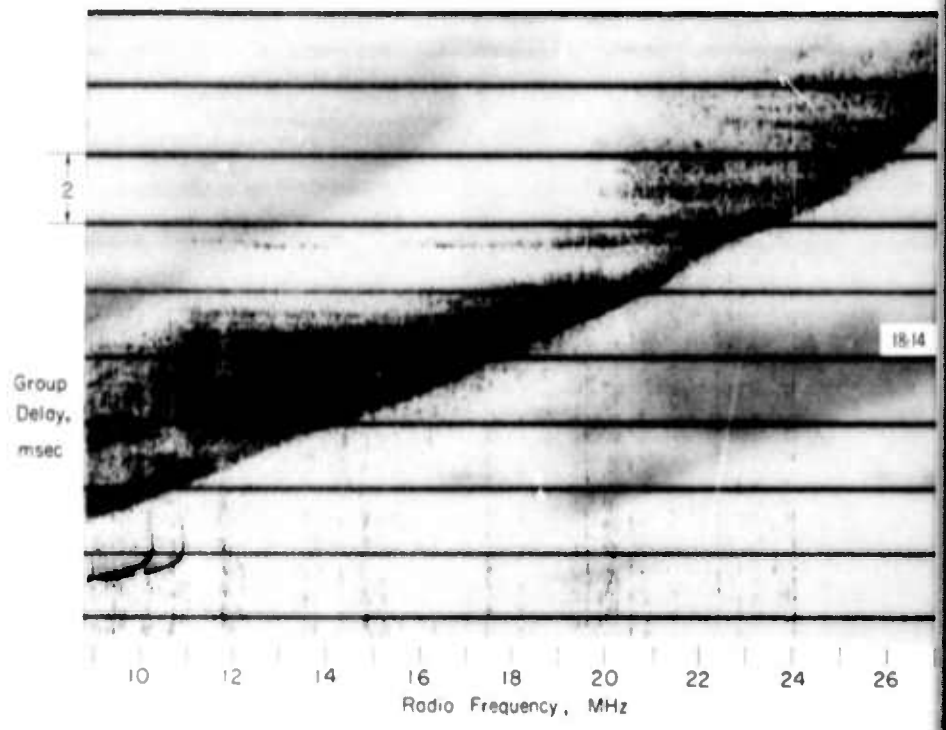
2
18:14
Group
Delay,
msec
10
12
14
16
18
20
22
24
26
Radio Frequency, MHz

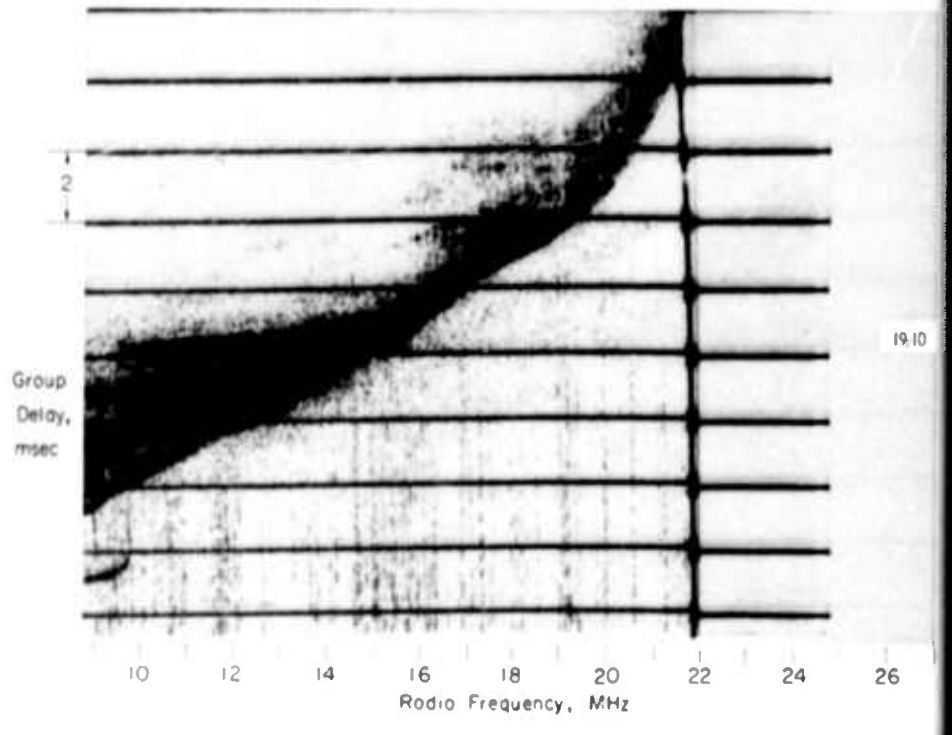
2
19:10
Group
Delay,
msec
10
12
14
16
18
20
22
24
26
Radio Frequency, MHz

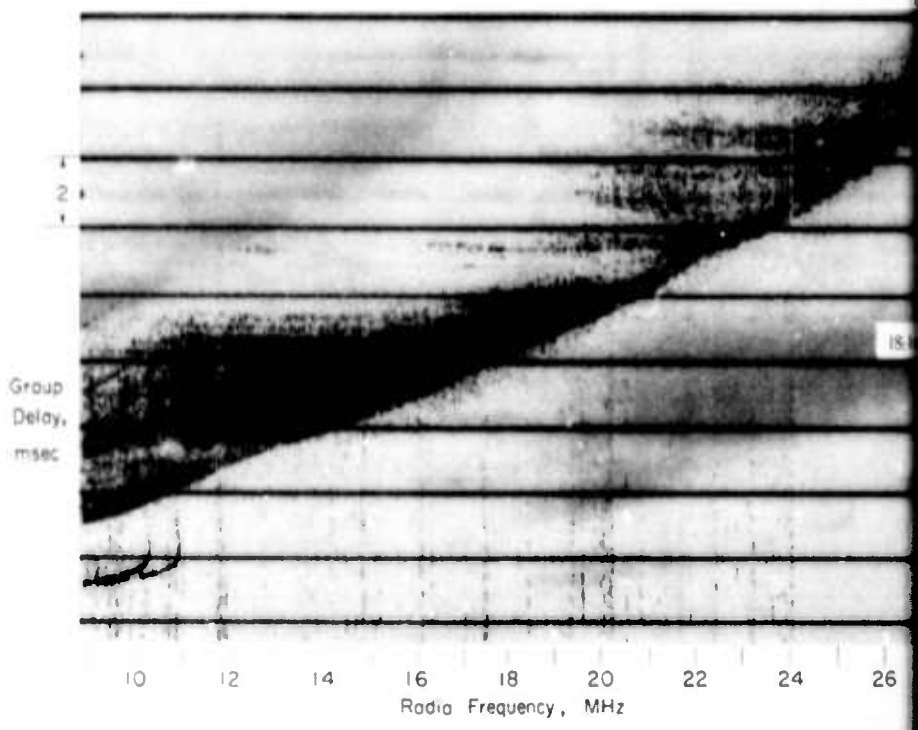
2
Group
Delay,
msec
10
12
14
16
18
20
22
24
26
Radio Frequency, MHz

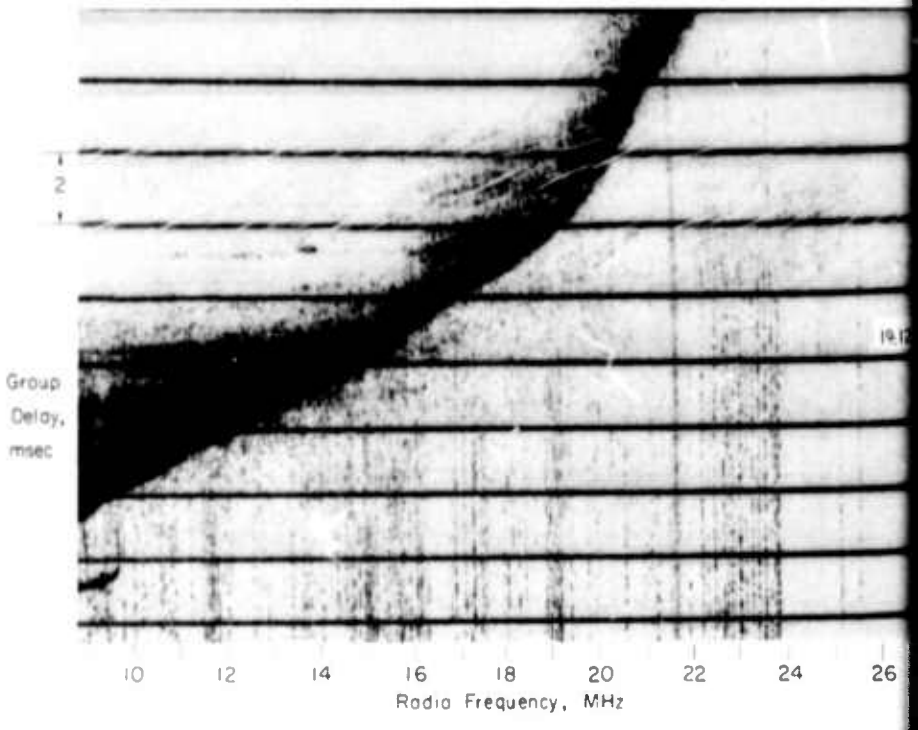
2
Group
Delay,
msec
10
12
14
16
18
20
22
24
26
Radio Frequency, MHz

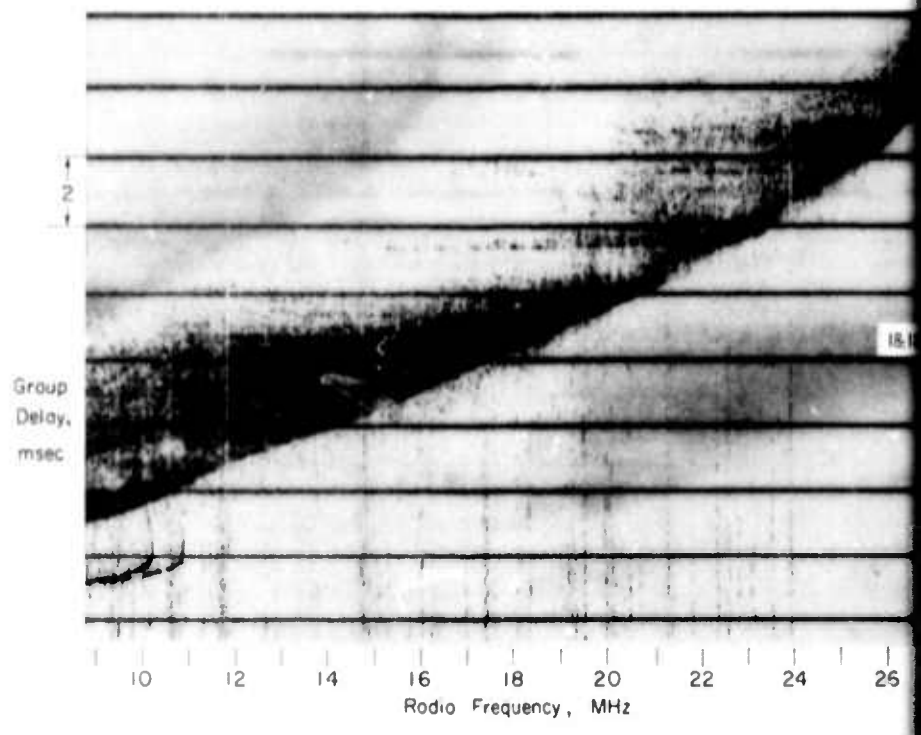
2
Group
Delay,
msec
10
12
14
16
18
20
22
24
26
Radio Frequency, MHz

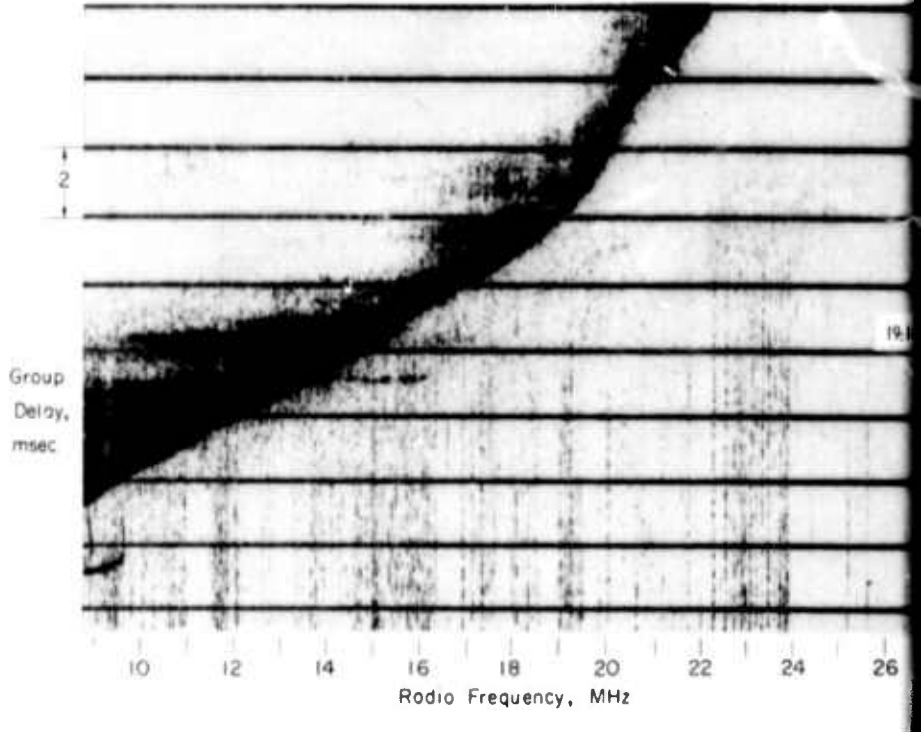
2
Group
Delay,
msec
10
12
14
16
18
20
22
24
26
Radio Frequency, MHz

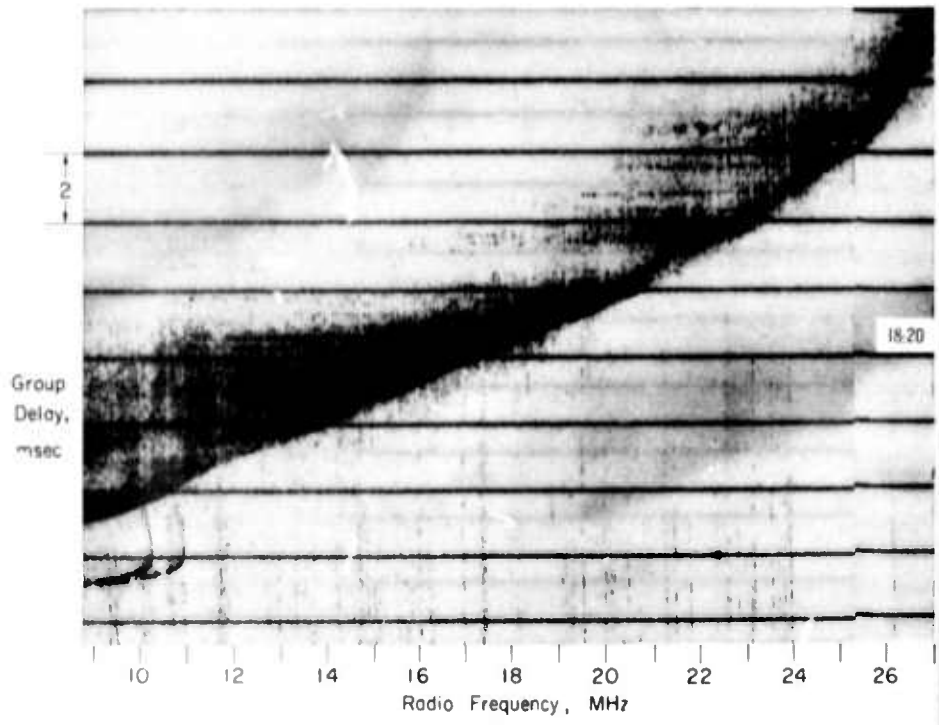
2
18:20
Group
Delay,
msec
10
12
14
16
18
20
22
24
26
Radio Frequency, MHz

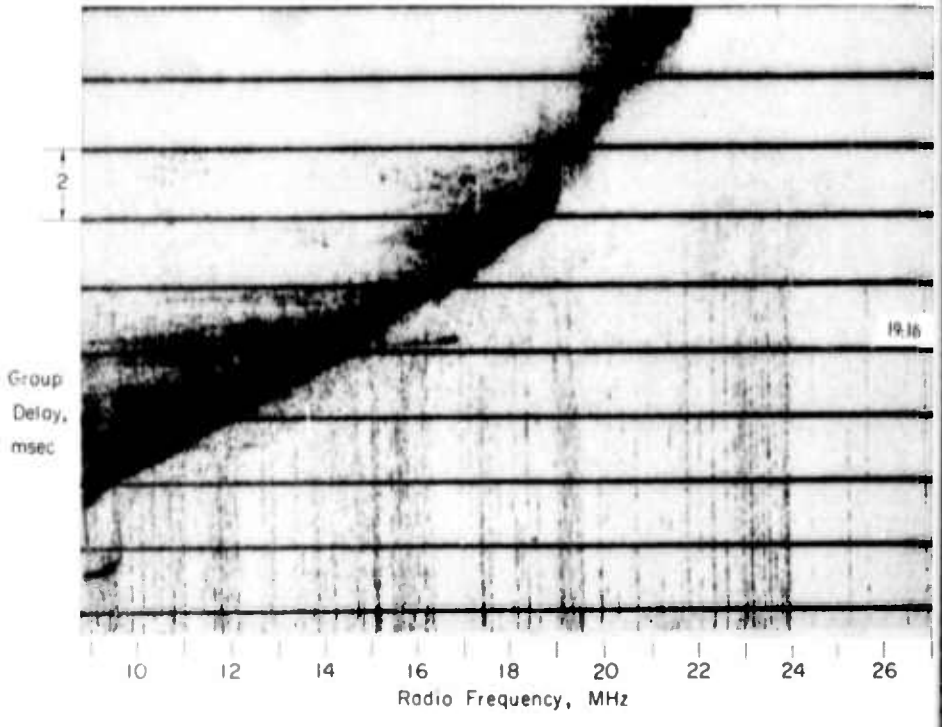
2
19:16
Group
Delay,
msec
10
12
14
16
18
20
22
24
26
Radio Frequency, MHz

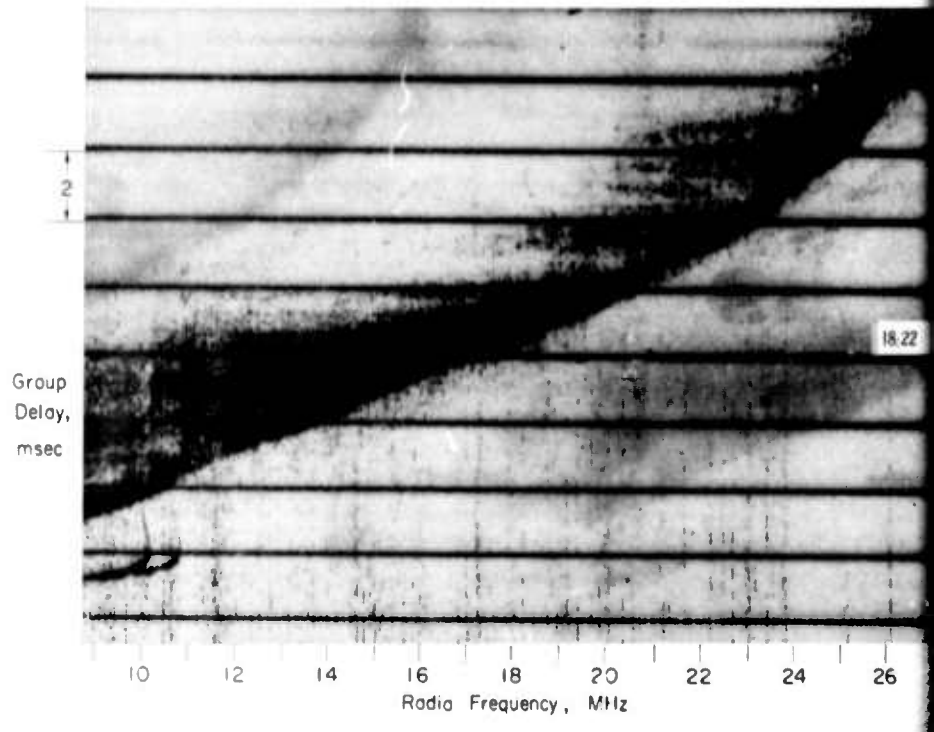
2
18.22
Group
Delay,
msec
10
12
14
16
18
20
22
24
26
Radio Frequency, MHz

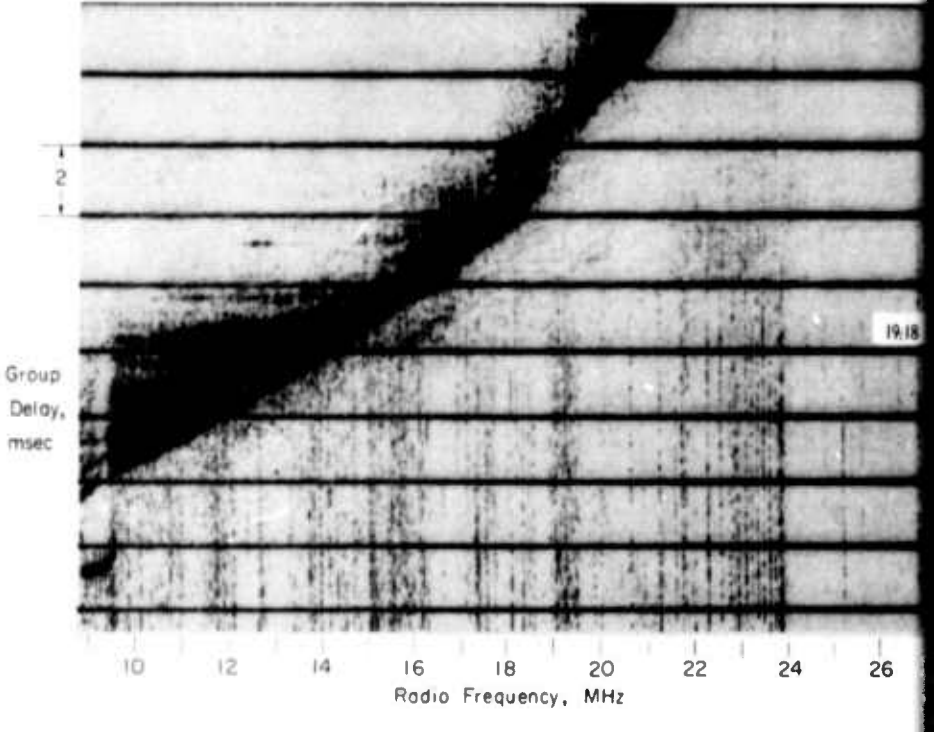
2
19.18
Group
Delay,
msec
10
12
14
16
18
20
22
24
26
Radio Frequency, MHz

DISTRIBUTION LIST

U-Series

NAVY

Chief of Naval Research
Department of the Navy
Washington, D. C. 20360
2 Attn: Code 418
1 Attn: Code 2027

Director
U.S. Naval Research Lab
Washington, D. C. 20390
1 Attn: Code 5320
(Mr. E. Zettle)
1 Attn: Code 5320
(Mr. J.M. Headrick)
1 Attn: Code 5432C
(Mr. F.A. Polinghorn)

Chief of Naval Operations
Department of the Navy
The Pentagon
Washington, D. C. 20350
1 Attn: OP-07TE
1 Attn: OP-723E

Commander
U.S. Naval Missile Center
Point Mugu, California 93041
1 Attn: Code N03022

Commander
Naval Weapons Center
China Lake, California 93555
1 Attn: Code 4025
(Mr. R.S. Hughes)

Commander
Naval Command Control Communications Laboratory Center
San Diego, California 92152
1 Attn: Mr. H.J. Wirth
1 Attn: Library

Commander
Naval Weapons Center
Corona Laboratories
Corona, California 91720
1 Attn: Mr. V.E. Hildebrand

Director
Office of Naval Research
Branch Office
495 Summer Street
Boston, Massachusetts 02210
1 Attn: Mr. Stan Curley

AIR FORCE

Headquarters, USAF
The Pentagon
Washington, D.C. 20330
1 Attn: AFNICAD
(MAJ Nyquist)
1 Attn: AFRDDF

Headquarters, USAF
Office of Assistant Chief of Staff, Intelligence
Washington, D. C. 20330
1 Attn: AFNICAA

Commander
Rome Air Development Center
Research & Technology Div.
Griffiss AFB, New York 13442
1 Attn: EMASO
(Mr. S. DiGennaro)
1 Attn: EMAES
(MAJOR D.R. Wipperman)
1 Attn: EMASR
(Mr. V.J. Coyne)
1 Attn: EMASA

Headquarters, AF Systems Command
Foreign Technology Division
Wright-Patterson AFB
Ohio 45433
1 Attn: TDC (Mr. Zabatakas)
1 Attn: TDEED
(Mr. W. L. Picklesimer)
1 Attn: TDCES
1 Attn: TDCE
(Mr. M.S.J. Grabener)

Headquarters
AF Systems Command
Research & Technology Division
Bolling AFB, Washington,
D.C. 20332
1 Attn: RTTC
(Mr. Philip Sandler)

Headquarters
USAF Security Service (OSA)
San Antonio, Texas 78241
1 Attn: Mr. W. L. Anderson
ODC-R

Headquarters
Air Defense Command
Ent AFB, Colorado Springs,
Colorado 80912
1 Attn: NPSD-A
1 Attn: ADLPC-2A
(LCOL R.J. Kaminski)
1 Attn: ADOAC-ER
1 Attn: NELC-AP

Electronics Systems Div. (ESSL)
L. G. Hanscom Field
Bedford, Massachusetts 01731
1 Attn: 440L

Headquarters SAC (OAI)
Offutt AFB
Omaha, Nebraska 68113
1 Attn: Mrs. E. G. Andrews

Headquarters, AFCRL
L.G. Hanscom Field
Bedford, Massachusetts 01731
1 Attn: CRUI
1 Attn: CRUP (Dr. G.J. Gassman)

U.S. Air Force
Western Test Range
Vandenberg AFB,
California 93437
1 Attn: WTGT
(Mr. Stanley Radom)

Headquarters, USAF AFTAC
Washington, D. C. 20333
1 Attn: TD-3

Major T.D. Damon
Hqtrs. Air Weather Service
(AWVDC)
1 Scott Air Force Base, Illinois
62265

ARMY

Office of the Assistant Chief
of Staff for Intelligence
Department of the Army
The Pentagon, Room 2B 457
Washington, D. C. 20310
1 Attn: Mr. Joseph Grady

U. S. Army SLAG
The Pentagon, Room 1B 657
Washington, D. C. 20310
1 Attn: Mr. N. R. Garofalo

Chief, Army Security Agency
Arlington Hall Station
Arlington, Virginia 22212
1 Attn: Mr. R. R. Neill
1 Attn: IAOPS-O(SA)

Commanding Officer
U.S. Army Security Agency
Processing Center
Vint Hill Farms Station
Warrenton, Virginia 22186
1 Attn: LT Alan Bagully
1 Attn: Technical Library

Commander, Electronics
Warfare Lab
Mt. View Office, USAEC
P.O. Box 205
Mt. View, California 94040
1 Attn: Mr. Joseph Bert

U. S. Army Foreign Science &
Technology Center
Munitions Building
Washington, D. C. 20315
1 Attn: Communications &
Electronics Division

Commanding General
U. S. Army Missile Command
Redstone Arsenal, Alabama 35809
1 Attn: AMSMI-RES

DEPT. OF DEFENSE

Director
Advanced Research Projects Agency
The Pentagon
Washington, D. C. 20301
1 Attn: Mr. Alvin Van Every

Office of the Assistant Director
Intelligence & Reconnaisance
Office of the Director of Defense
Research & Engineering
The Pentagon, Room 3E 119
Washington, D. C. 20301
1 Attn: Mr. H. A. Staderman

Director
National Security Agency
Ft. George G. Meade
Maryland 20755
1 Attn: K-344 (Mr. C. Gandy)
1 Attn: C3-TDL

Deputy Director
Research & Technology
Office of the Director of
Defense Research & Engineering
The Pentagon, Room 3E 1030
Washington, D. C. 20301
1 Attn: Dr. C. W. Sherwin

Office of the Assistant
Director (Defense Systems)
Defense Research & Engineering
The Pentagon, Room 3D 138
Washington, D. C. 20301
1 Attn: Mr. Daniel Fink

Director, Defense
Intelligence Agency
The Pentagon, Room 3B 259
Washington, D. C. 20301
1 Attn: DIACO-4
1 Attn: DIAST-2B

Director, Weapons Systems
Evaluation Group
Office of the Director of
Defense, Research & Engineering
1 Washington, D. C. 20301

Defense Documentation Center
Cameron Station
20 Alexandria, Virginia 22314

National Aeronautics & Space
Administration
Ames Research Center
Moffett Field, California 94035
1 Attn: Dr. Kwok-Long Chan
1 Attn: Mr. Lawrence Colin

OTHER

ITT Electro-Physics Labs Inc.
3355 - 52nd Avenue
Hyattsville, Maryland 20781
1 Attn: Mr W. T. Whelan

Institute for Defense Analyses
400 Army-Navy Drive
Arlington, Virginia 22202
1 Attn: Dr. Louis Wetzel

MITRE Corporation
E Bldg., Room 353
Bedford, Massachusetts 01730
1 Attn: Mr. W.A. Whitcraft, Jr.
1 Attn: Mr. Bill Talley

RAND Corporation
1700 Main Street
Santa Monica, California 90406
1 Attn: Dr. Cullen Crain
1 Attn: Library

Raytheon Company
Spencer Laboratory
2 Wayside Road
Burlington, Massachusetts 01803
1 Attn: Mr. L. C. Edwards

U-Series - Other (Cont)

Stanford Research Institute
Menlo Park, California 94025
1 Attn: Dr. David Johnson

Sylvania Electronics Systems
Electronics Defense Laboratory
P. O. Box 205
Mt. View, California
1 Attn: Mr. John DonCarlos

Mr. Thurston B. Soisson
Box 8164 SW Station
1 Washington, D. C. 20024

Astrophysics Research Corporation
10889 Wilshire Blvd.
Los Angeles, California 90024
1 Attn: Dr. Alfred Reifman

Institute of Science & Technology
The University of Michigan
P. O. Box 618
Ann Arbor, Michigan 48105
1 Attn: BAMIRAC Library

Bendix Corporation
Bendix Radio Division
Baltimore, Maryland 21204
1 Attn: Mr. John Martin

AVCO Systems Division
Lowell Industrial Park
Lowell, Massachusetts 01851
1 Attn: Mr. Sidney M. Bennett

U.S. Department of Commerce
ITSA - ESSA
Boulder, Colorado 80302
1 Attn: Mr. William Utlaut
1 Attn: Mr. L. H. Tveten
1 Attn: Mr. W. A. Klemperer,
Div. 530, ESSA

Page Communications, Inc.
3300 Whitehaven St., NW
Washington, D. C. 20008
1 Attn: Mr. David Fales, III

Massachusetts Institute of
Technology
Lincoln Laboratory
P. O. Box 73
Lexington, Massachusetts 02173
1 Attn: Dr. J. H. Chisholm

Massachusetts Institute
of Technology
Center for Space Research
Building 33-109
Cambridge, Massachusetts 02138
1 Attn: Dr. J.V. Harrington

Princeton University
James Forrestal Research Center
Plasma Physics Laboratory
P. O. Box 451
Princeton, New Jersey 08540
1 Attn: Dr. Edward Frieman

University of California
Mathematics Department
Berkeley, California 94720
1 Attn: Dr. E. J. Pinney

Electronics Research Laboratory
University of California
Berkeley, California 94720
1 Attn: Prof. D. J. Angelakos

Battelle-Defender
Battelle Memorial Institute
505 King Avenue
1 Columbus, Ohio 43201

HRB-Singer, Inc.
Science Park
P.O. Box 60
State College, Pennsylvania 16801
1 Attn: Library

Pickard & Burns,
Research Department
103 Fourth Avenue
Waltham, Massachusetts 02154
1 Attn: Dr. J. C. Williams

Other U-Series (Cont)

Sylvania Electronic Systems
Applied Research Laboratory
40 Sylvan Road
Waltham, Massachusetts 02154
1 Attn: Library

Department of Electrical
Engineering
Radiolocation Research Laboratory
University of Illinois
Urbana, Illinois 61803
1 Attn: 311 EERL (Mr. D.G. Detert)

Arecibo Ionospheric Observatory
Box 995
Arecibo, Puerto Rico 00613
1 Attn: Librarian

The University of Texas
Electrical Engineering Research
Laboratory
Route 4, Box 189
Austin, Texas 78756
1 Attn: Mr. C. W. Tolbert

Rice University
Fondren Library
P.O. Box 1892
1 Houston, Texas 77001

Purdue University
Library
1 West Lafayette, Indiana

Telcom, Incorporated
5801 Lee Highway
Arlington, Virginia 22207
1 Attn: Mr. J. D. Ahlgren,
Vice President

UNCLASSIFIED

Security Classification

DOCUMENT CONTROL DATA - R & D

Security classification of title, body of abstract and indexing annotation must be entered when the overall report is classified

1. ORIGINATING ACTIVITY (Corporate author)

STANFORD ELECTRONICS IABORATORIES

2a. REPORT SECURITY CLASSIFICATION

UNCIASSIFIED

2b. GROUP

3. REPORT TITLE

THE INTERPRETATION OF HF SWEEP-FREQUENCY BACKSCATTER SOUNDINGS TO DEDUCE THE STRUCTURE OF LOCALIZED IONOSPHERIC ANOMALIES

4. DESCRIPTIVE NOTES (Type of report and inclusive dates)

Technical Report No. 116, December 1967

5. AUTHOR(S) (First name, middle initial, last name)

Thomas A. Croft

6. REPORT DATE	7a. TOTAL NO. OF PAGES	7b. NO. OF REFS
December 1967	139	13

8a. CONTRACT OR GRANT NO	9a. ORIGINATOR'S REPORT NUMBER(S)
Nonr-225(64)	TR No. 116
b. PROJECT NO	SEL-68-029
NR 088-019	9b. OTHER REPORT NO(S) (Any other numbers that may be assigned this report)
c.	
d.	

10. DISTRIBUTION STATEMENT

This document is subject to special export controls and each transmittal to foreign governments or foreign nationals may be made only with prior approval of the Office of Naval Research, Field Projects Branch, Washington, D. C., 20360.

11. SUPPLEMENTARY NOTES	12. SPONSORING MILITARY ACTIVITY
	Office of Naval Research ARPA Order No. 196

13. ABSTRACT

By use of computer simulation, it is possible to predict the effect of traveling ionospheric irregularities upon the data obtained by HF sweep-frequency ground-backscatter sounders. The simulation process makes use of an ionospheric model in which radio rays are traced to determine the time distribution of energy along the distant ground after skywave travel. Subsequent computation yields a synthetic record of the echo amplitude as a function of radio frequency and time delay, much like the experimental data. The degree of realism achieved is limited primarily by the need for economy; the process used here is a simplified version of one previously described (Ref. 1).

It is shown that a localized ionospheric irregularity causes a discontinuity in backscatter echo amplitude with a limited extent in frequency and with a delay that is comparatively independent of frequency. This discontinuity has the appearance of a short streak on the synthetic records; such a feature is common in experimental data. When an ionospheric irregularity exists from the ground to an unlimited altitude and is formed with its long axis tilted about 45° away from the observer, a backscatter streak appears which is spread over the entire frequency range of the background echo. Furthermore, this streak is tilted on the record, i.e., its time delay increases with an increase in frequency. When a simila anomaly is programmed so that it tilts inward toward the observer, then the resulting streak has a delay that decreases with an increase in frequency. A relation between the tilt of the anomaly and the tilt of the backscatter streak is thus demonstrated. The relation is in accord with a limited observation that tilted streaks in experimental backscatter move only in the predicted direction of anomaly motion as deduced from the measured direction of anomaly tilt.

DD FORM 1473

UNCLASSIFIED

Security Classification

14 KEY WORDS	LINK A		LINK B		LINK C	
	ROLE	WT	ROLE	WT	ROLE	WT
GRAVITY WAVES (ATMOSPHERIC) TRAVELING IONOSPHERIC DISTURBANCES IONOSPHERIC IRREGULARITIES HIGH FREQUENCY RADIO HF RADIO BACKSCATTER RAYTRACING COMPUTER SIMULATION SKYWAVES NOCTILUCENT CLOUDS OBLIQUE IONOGRAMS						

Abstract (contd)

Anomalies with constant altitude are shown to produce new, short-range leading edges on the backscatter. Experimental data having this form can thus be interpreted as an indication of the presence of small "layerlets" within the ionosphere, but it is noted that there are at least three other possible causes for this particular form of backscatter echo.